THE SILICON MICROVERTEX DETECTOR OF THE H1 EXPERIMENT: READOUT, EVENT RECONSTRUCTION, AND STUDIES ON HEAVY QUARK DECAYS

DISSERTATION
zur Erlangung des Doktorgrades
des Fachbereichs Physik
der Universität Hamburg

vorgelegt von
Markus Kausch-Blecken v. Schmeling
aus Trier

Hamburg
1998

Gutachter der Dissertation: Prof. Dr. B. Naroska
Prof. Dr. R. Klanner

Gutachter der Disputation: Prof. Dr. B. Naroska
Prof. Dr. V. Blobel

Datum der Disputation: 06. 10. 1998

Dekan des Fachbereichs Physik und
Vorsitzender des Promotionsausschusses: Prof. Dr. B. Kramer

Abstract

This thesis presents the readout system and the event reconstruction of the Central Silicon Tracker (CST), the silicon strip microvertex detector of the H1 experiment at HERA. The CST consists of two layers of double-sided silicon sensors and delivers three-dimensional position information. A total of 81920 strips are read out by custom-designed readout chips with an integrated analog pipeline that is operated at the HERA bunch crossing frequency of 10.4 MHz. The pipeline depth of 32 buffers is matched to the decision time of the central trigger of $2.4\,\mu$s. For triggered events, the signal charges from the respective pipeline buffer are amplified, multiplexed, and transferred to dedicated processor modules where they are digitized. The memory of these modules provides a 16-fold multi-event buffering, so that the subsequent online processing of the data can be performed asynchronously to the trigger signals. Fast hit finding algorithms are applied to reduce the amount of raw data. The task of determining and updating pedestals and noise values for each of the readout strips is also performed online by the processor modules. The design goal of operating the online processing system at triggered event rates of ≈ 100 Hz without introducing dead time was achieved in the first year of operation. On average, the event size is reduced by a factor of 60.

In the subsequent offline event reconstruction clusters are built from the information of the hit strip data first. The cluster position is calculated by means of a center-of-gravity algorithm taking into account alignment corrections. Separately for the R-Φ- and the R-z-projections, the found clusters are then assigned to tracks measured by the central jet chamber of the H1 detector. The efficiency for linking a track to a CST cluster in R-Φ is 98%. In R-z, where the CST detectors have a lower signal-to-noise ratio, an efficiency of 86% was measured. By means of a constrained fit, the resolution of the track parameters measured in the central region of the H1 detector is improved considerably.

With these improved tracks the potential of CST measurements for heavy quark tagging was demonstrated in a study of the semi-muonic decay of particles containing heavy quarks. A sample of events with muons of high transverse momentum ($p_t > 2\,\mathrm{GeV}$) has been selected from the data taken with the CST in 1997, and the impact parameter method was applied in order to prove that the origin of the muon tracks is separated from the primary event vertex. A significant asymmetry in the impact parameter distribution is seen which is not present in a background data sample that was selected for comparison. If the b-quark content of the muon sample is further enriched by applying harder cuts , the on average longer lifetime is reflected by a more significant asymmetry in the impact parameter distribution. This finding is supported by Monte Carlo data samples containing muons from c- and b-quark decay respectively that have been studied in addition.

Kurzfassung

Gegenstand dieser Arbeit ist das Datenaufnahmesystem und die Ereignisrekonstruktion für den Central Silicon Tracker (CST), den Siliziumstreifen-Mikrovertexdetektor des H1-Experimentes bei HERA. Der CST besteht aus zwei Lagen doppelseitiger Siliziumdetektoren und liefert dreidimensionale Ortsinformation. Insgesamt 81920 Streifen werden von speziell entwickelten Auslesechips mit einer integrierten Analogpipeline ausgelesen, die mit der Strahlkreuzungsfrequenz von HERA (10.4 MHz) betrieben wird. Die Zahl der Pipelinespeicher von 32 ist an die Entscheidungszeit des Triggersystems von 2.4μs angepaßt. Im Falle eines akzeptierten Ereignisses werden die Signalladungen des zugehörigen Pipelinespeichers verstärkt und zu Prozessormodulen transferiert, wo die Digitalisierung stattfindet. Der Speicher dieser Module ermöglicht ein 16-faches multi-event buffering, sodaß die weitere Signalverarbeitung asynchron zu den Triggersignalen erfolgen kann. Dabei werden schnelle Treffersuchalgorithmen zur Reduzierung des Datenvolumens eingesetzt. Die Bestimmung und Aktualisierung von Pedestal- und Rauschwerten für jeden Auslesestreifen erfolgt ebenfalls online durch die Prozessormodule. Das Ziel des totzeitfreien Betriebs des Online-Signalverarbeitungssystems bei Ereignisraten von ≈ 100 Hz wurde im ersten Betriebsjahr erreicht. Im Durchschnitt wird das Datenvolumen um einen Faktor 60 reduziert.

Bei der darauffolgenden Offline-Ereignisrekonstruktion werden zunächst Cluster mit Hilfe der Information über die getroffenen Streifen gebildet. Die Position eines Clusters wird durch einen Schwerpunktsalgorithmus ermittelt, wobei Korrekturen bezüglich der Ausrichtung des Detektors berücksichtigt werden. Getrennt für die R-Φ- und die R-z-Projektionen werden die Cluster dann Spuren zugeordnet, die in der zentralen Jetkammer des H1-Experiments gemessen wurden. Die Effizienz der Zuordnung eines CST-Clusters zu einer Spur in R-Φ beträgt 98%. Für die R-z-Projektion, wo die CST-Detektoren ein schlechteres Signal-zu-Rausch-Verhältnis haben, wurde ein Wert von 86% ermittelt. Durch eine gemeinsame Anpassung von Cluster- und Spurparametern wird die Genauigkeit der Spuren, die im zentralen Bereich des H1-Detektors gemessen werden, erheblich verbessert.

Mit Hilfe dieser verbesserten Spuren wurde das Potential der CST-Messungen für die Erkennung von schweren Quarks durch eine Studie semi-myonischer Zerfälle von Teilchen, die schwere Quarks enthalten, demonstriert. Aus den 1997 vom CST aufgezeichneten Daten wurden Ereignisse mit Myonen selektiert, die einen großen transversalen Impuls haben ($p_t > 2$ GeV). Die Impaktparameter-Methode wurde angewandt, um nachzuweisen, daß der Ursprung der Myonspuren vom Primärvertex separiert ist. Eine signifikante Asymmetrie der Impaktparameterverteilung wurde beobachtet, die in einem zum Vergleich betrachteten Untergrund-Datensatz nicht vorliegt. Wird der b-quark-Gehalt des Myon-Datensatzes durch härtere Schnitte erhöht, zeigt sich die durchschnittlich längere Lebensdauer in einer stärkeren Asymmetrie der Impaktparameter-Verteilung. Zusätzlich untersuchte Monte Carlo Datensätze mit Myonen aus c- und b-quark-Zerfällen bestätigen die Beobachtungen.

Contents

Introduction

In recent years, silicon strip microvertex detectors have become an important tool in high energy physics experiments. Their outstanding position resolution of the order of $10\,\mu$m allows the measurement of particles with typical decay lengths of well below one centimetre. The primary field of application is therefore the physics of heavy quarks where particle decay times of typically 1 ps are studied. Silicon strip detectors have been employed since the beginning of the 1980s, first in fixed target experiments for the study of charmed particles. For about 10 years, they have also been operated in colliding beam experiments, and have since contributed to a number of results, e.g. the precision measurements of the τ-lepton and b flavoured hadron lifetimes at LEP or the selection of events with top quark production at the Tevatron.

Modern collider detectors consist of several subdetectors for dedicated tasks, e.g. tracking, calorimetry, or muon detection. The detectors are usually arranged in cylindrical symmetry around the beam line and cover the region around the interaction point hermetically. In this environment, microvertex detectors are the innermost devices and are surrounded by tracking detectors, most commonly drift chambers. The standard method to use microvertex detector data for physics analyses is to improve the track measurements of these outer tracking detectors with respect to momentum and position resolution. For this purpose, hits from the microvertex detector have to be assigned to tracks measured by the surrounding track detectors. The high precision of the microvertex hits then puts strong constraints on the track parameters thus reducing their uncertainties. As a consequence the accuracy of the vertex determination —for the primary interaction as well as for secondary vertices due to the decay of long-lived particles— is improved considerably. This increased precision in the reconstruction of the event topology has proven to be very effective for studying processes with heavy quarks.

Nowadays, microvertex detectors commonly provide three-dimensional position information which can be achieved by employing double-sided detectors with silicon strips extending in different directions on the two sides. This leads to a large number of readout strips, typically of the order of 10^5–10^6. The detector system as a whole —including the front-end readout electronics— has to be very compact on the other hand, since the amount of non-active material close to the interaction point has to be minimized. Therefore, highly integrated readout systems are needed.

At the electron-proton collider HERA in particular, a further challenge to the readout system is due to the high particle bunch crossing rate of 10.4 MHz which implies that for an event that is read out, the time span for collecting and amplifying the signal charge from the silicon strips is very short.

The subject of this thesis is the Central Silicon Tracker (CST), a silicon strip microvertex detector that was installed in 1995/96 as part of an upgrade program of the H1 detector at HERA and began its regular data taking operation in 1997. In particular the readout system and the event reconstruction steps are described. Moreover, CST data taken in 1997 have been analyzed in a study on heavy quark decays in order to demonstrate that high-resolution measurements of the vertex detector can be employed for tagging heavy quarks at HERA and are thus suited to complement and improve the heavy flavour analyses that are carried out at the H1 experiment.

The thesis is structured as follows:

First, the physical processes that are studied at HERA are briefly discussed focussing on the production of heavy quarks in electron-proton scattering and on their subsequent decay modes.

Chapter 2 introduces the HERA collider and the H1 detector. The central tracking devices of the H1 detector and the methods employed for track reconstruction are described in more detail. Next, the microvertex detector CST is portrayed.

The system for the readout of the silicon trackers of H1 is presented in chapter 3. It covers the hardware components —namely the electronics for the front-end readout and the online processor modules— as well as the software employed to ensure the data flow from the detectors onto storage tapes. In particular, the algorithms implemented for an online hit detection in CST data are explained. Furthermore, the systems for controlling the detector operation and for an online monitoring of the data are described.

Chapter 4 gives a description of the event reconstruction of CST data. After a brief overview and a short section on the alignment of the CST with respect to the surrounding detectors, the reconstruction of hits from the front-end data is presented. The further steps include the assignment of hits found in the CST to tracks measured in the surrounding tracking detectors and a combined fit of the parameters of these tracks and hits. The quality of this fit is discussed and values for the resolution of the fitted tracks are determined. The chapter ends with a description of the integration of the software module for the reconstruction of CST data into the software framework of H1.

A first analysis using data taken by the CST in 1997 is presented in chapter 5. An explorative study on the impact parameter of muons measured in the CST has been carried out in order to demonstrate the qualification of the improved track parameters for a tagging of heavy quark decays. The study incorporates Monte Carlo simulations with a first employment of the new detector simulation of the CST.

The final chapter gives a summary of the results and discusses possible future developments for the reconstruction as well as for further analyses.

Chapter 1

Electron-proton scattering at HERA

After a discussion of the kinematics of electron-proton scattering, two kinematic domains are introduced: *deep-inelastic scattering* and *photoproduction*. At HERA, the latter is the main source for the production of heavy quarks. Physics with heavy quarks is the main application for the data of microvertex detectors and is therefore introduced in the third section. Production mechanisms as well as decay modes are discussed.

1.1 Kinematics of electron-proton scattering

Electron-proton scattering is the interaction of a point-like elementary particle with a compound object. It is described by means of the exchange of a gauge boson, which can be a photon, a Z^0, or a $W^{\pm}$-boson. According to the charge of the exchanged particle, one distinguishes between neutral-current (NC) and charged-current (CC) interactions. At HERA energies, photon exchange is the dominant process due to the large masses of the Z^0- and W-bosons.

If the four-momentum transfer from the incident electron to the proton is small, the photon interacts with the proton as a whole (elastic scattering). At higher four-momentum transfers, the boson is scattered off the proton constituents providing thus a means to probe the proton structure (inelastic scattering). In the framework of the *quark parton model* (QPM), the proton constituents are quarks and gluons, and the photon couples to the charged quarks only. Inelastic electron-proton scattering can thus be described as elastic electron-quark scattering.

Fig. 1.1 shows the Feynman-diagrams for the NC- and CC-processes: an incoming electron of four-momentum p_e is scattered off a quark that carries the fraction x of the proton four-momentum P. The final state consists of the scattered lepton having four-momentum p_e' and the hadronic final state (denoted by X). The center of mass energy $\sqrt{s}$ of the inclusive electron-proton scattering is given by the beam energies (neglecting the particle masses):

$$s = (P + p_e)^2 \approx 4\,E_e E_p \tag{1.1}$$

At a fixed center of mass energy, the kinematics of the scattering process is described completely by two independent Lorentz-invariant variables. Commonly used are the *virtuality* Q^2 and one of the two

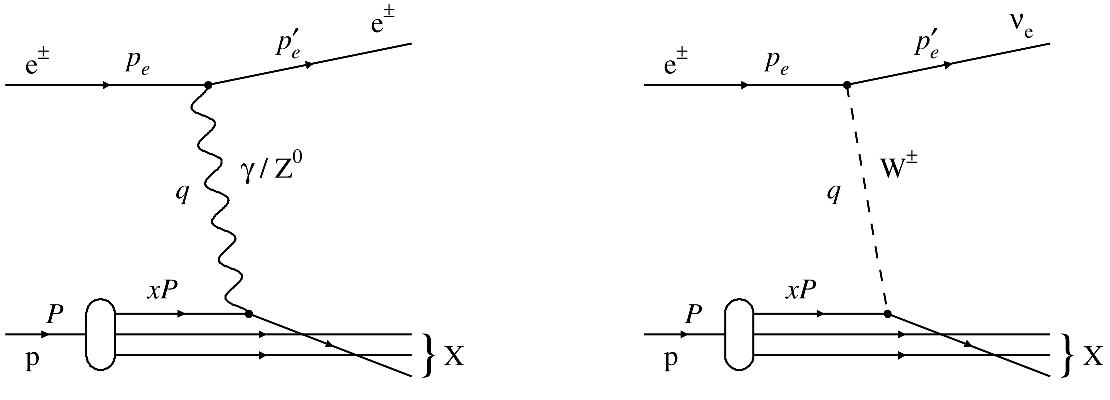

Neutral current

Charged current

Figure 1.1: *Feynman graphs for neutral-current and charged-current electron-proton scattering*

dimensionless scaling variables x and y:

$$Q^2 = -q^2 = -(p_e - p'_e)^2 \tag{1.2}$$

$$x = \frac{Q^2}{2P \cdot q} \tag{1.3}$$

$$y = \frac{P \cdot q}{P \cdot p_e} \tag{1.4}$$

The *Bjorken scaling variable* x is the momentum fraction of the proton carried by the scattered parton while the *inelasticity* y is the ratio of the actual to the maximum momentum transfer in the proton rest frame. Both take values between 0 and 1. Neglecting the particle masses the relation between the kinematic variables is

$$Q^2 = x \cdot y \cdot s \tag{1.5}$$

The hadronic final state X can be characterized by its invariant mass W that can be expressed by x and Q^2 exploiting four-momentum conservation at the hadronic vertex (m_p being the proton mass):

$$W^2 = (P+q)^2 = Q^2(\frac{1}{x} - 1) + m_p^2 \approx Q^2/x \tag{1.6}$$

For large values of W^2 ($W^2 \gg m_p^2$), the proton "loses" its identity and breaks up: the hadronic final state consists of a large number of particles. This is the domain of *deep-inelastic scattering* (DIS). The unscattered proton partons form the spectator jet that vanishes into the beam pipe and cannot be detected while the scattered quark undergoes a fragmentation process resulting in the current jet.

If $Q^2 \to 0$ on the other hand, the emitted photon is (quasi-)real, and the electron is scattered at very small angles. The interaction can be regarded as being composed of a photon flux from the electron and a subsequent photon-proton scattering process. This sector is called *photoproduction*.

In addition to W the *pseudo-rapidity* η is introduced for the characterization of a hadron in the final state:

$$\eta = \frac{1}{2} \ln \frac{p + p_z}{p - p_z} = - \ln(\tan(\frac{\Theta}{2})) \tag{1.7}$$

where p is the momentum of the hadron, p_z its z-component, and Θ is the polar scattering angle[1]. At the beam energies of HERA in 1997 of $E_p = 820\,\text{GeV}$ and $E_e = 27.5\,\text{GeV}$ the center of mass energy is $\sqrt{s} = 300\,\text{GeV}$ and a squared four-momentum transfer Q^2 of up to $90200\,\text{GeV}^2$ is kinematically possible.

For the *extraction of the kinematic quantities* several methods can be employed since the detectors deliver more information than the two measured observables needed. The methods are based on the quantities either of the scattered electron, or of the hadronic final state, or of both. They differ in accuracy and applicability depending on the kinematic range and the nature of the scattering process.

1.2 Kinematic domains

1.2.1 Deep inelastic scattering

Deep inelastic scattering is characterized by high values of Q^2 and large hadronic masses W. The double-differential ep-cross-section in lowest order of the electromagnetic coupling constant α is given by

$$\frac{d^2\sigma^{NC}_{e^\pm p}(x, Q^2)}{dx\, dQ^2} = \frac{4\pi\alpha^2}{xQ^4} \left\{ \frac{y^2}{2} 2xF_1(x, Q^2) + (1 - y)F_2(x, Q^2) \mp (y - \frac{y^2}{2})xF_3(x, Q^2) \right\} \tag{1.8}$$

F_1, F_2, and F_3 are the proton *structure functions* that are related to the a priori unknown proton structure. The F_3-term contributes only for Z^0-exchanges. In the QPM framework, the structure functions are related to the parton density functions q_i and the parton charges e_i, and a simple behaviour for the DIS-limit ($Q^2 \to \infty$, $pq \to \infty$) is predicted [1]:

$$F_1(x, Q^2) \to F_1(x) = \frac{1}{2} \sum_i e_i^2 (q_i(x) + \bar{q}_i(x)) \tag{1.9}$$

$$F_2(x, Q^2) \to F_2(x) = \sum_i e_i^2 x (q_i(x) + \bar{q}_i(x)) \tag{1.10}$$

It is summed over all quarks and anti-quarks in the proton. The fact that the structure functions do depend on x only is known as *Bjorken scaling*.

However, a more dynamic proton model that accounts for interactions between the partons by means of gluon exchanges leads to a scaling violation (the structure functions depend logarithmically on Q^2) as well as to a violation of the *Callan-Gross relation* $2xF_1(x) = F_2(x)$ that can be derived from Eq. (1.9) and (1.10) [2]. The underlying theory is the *quantum chromodynamics* (QCD). It introduces additional processes between the partons (gluon radiation, quark-antiquark production, gluon self-coupling) that are described in perturbation theory. Using a factorization theorem, this leads to generalized equations for the structure functions.

---

[1] At HERA, Θ is defined with respect to the proton direction ($\equiv$ forward direction).

1.2.2 Photoproduction

In photoproduction events, Q^2 is ≈ 0, so that the electron is scattered at small angles a quasi-real photon is emitted. At HERA, the cross-section for inclusive electron-proton scattering is dominated by photoproduction processes. The total photoproduction cross-section can be derived from the differential electron-proton cross-section:

$$\frac{d^2\sigma_{ep}}{dy\,dQ^2} = \frac{\alpha}{2\pi Q^2}\left(A(y,Q^2)\cdot\sigma^T_{\gamma^* p}(y,Q^2) + B(y,Q^2)\cdot\sigma^L_{\gamma^* p}(y,Q^2)\right) \tag{1.11}$$

that is composed of the contributions from transversely and longitudinally polarized photons σ^T and σ^L with A and B being kinematic variables. In the Weizsäcker-Williams approximation [3], which is valid for small Q^2, the longitudinal component is negligible, that is $\sigma^{tot}_{\gamma p} \approx \sigma^T_{\gamma^* p}$. Introducing the flux of transversely polarized photons $f_{\gamma/e}(y,Q^2)$ one gets:

$$\frac{d^2\sigma_{ep}}{dy\,dQ^2} = f_{\gamma/e}(y,Q^2)\cdot\sigma^{tot}_{\gamma p} = \frac{\alpha}{2\pi Q^2}\frac{1}{y}\left(1+(1-y)^2-2\frac{m_e^2 y^2}{Q^2}\right)\cdot\sigma^{tot}_{\gamma p} \tag{1.12}$$

There are a number of contributions to the cross-section due to the fact that, apart from being the gauge boson of the electroweak interaction, the photon has hadronic properties as well. In leading order QCD, one distinguishes between *direct processes* where the photon interacts point-like with a parton and *resolved processes* where a parton from the photon couples to the proton parton.

- The direct processes are the photon-gluon fusion (Fig. 1.2a) and the QCD compton process (Fig. 1.2b) with the parton from the proton being a quark and a gluon respectively. At HERA, the photon-gluon fusion is the main source for the production of heavy quarks, i.e. $c\bar{c}$- and $b\bar{b}$-pairs. The processes are calculable in the framework of perturbative QCD above a minimal transverse momentum ($p_t > 1.5\,\mathrm{GeV}$).
- Two processes contribute to the resolved part [4]:
  - a component described by the vector meson dominance model (VDM). The photon fluctuates into a quark-antiquark pair that forms a bound state: a virtual vector meson that subsequently interacts with the proton parton (Fig. 1.2c). The VDM is a phenomenological model and the processes cannot be calculated using perturbative QCD.
  - the anomalous component where the quark-antiquark pair from the photon is not bound and the interaction can be described in terms of a hard subprocess calculable in pQCD (Fig. 1.2d). In addition to the two final state jets from the hard subprocess, the hadronic photon remnant can form a third jet.

The hadronic nature of the photon is described analogous to the proton in terms of a photon structure function $F_2^\gamma(x_\gamma, Q^2)$ where x_γ is the fraction of the photon momentum that enters in the hard subprocess. In this connection, a term for the coupling of the photon to a quark-antiquark pair is introduced that accounts for the anomalous components of the cross-section.

1.3 Heavy quarks

The study of processes involving the production and decay of heavy quarks is the primary domain for making use of the high-resolution measurements of microvertex detectors. This is due to the relative

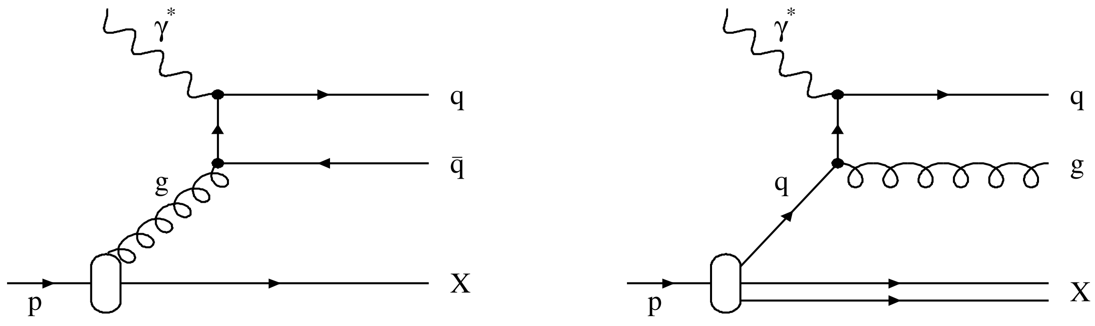

(a) photon-gluon fusion (b) QCD compton process

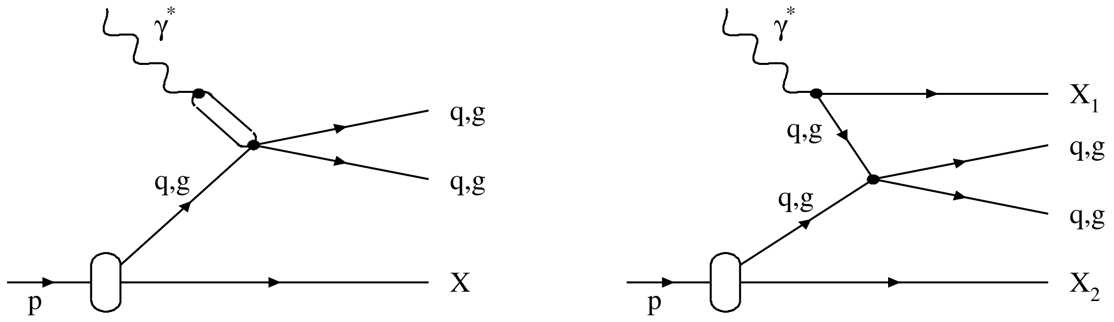

(c) VDM (d) anomalous component

Figure 1.2: *Diagrams showing photoproduction processes at HERA*

long lifetime of hadrons with heavy quarks resulting in large decay lengths that can be resolved. At HERA, the production cross-section for charm quarks is of the order of $\sigma(ep \rightarrow ec\bar{c}X) \approx 1\,\mu\text{b}$ while the $b\bar{b}$-cross-section is smaller by two orders of magnitude. At the HERA design luminosity of $100\,\text{pb}^{-1}$, this corresponds to $\approx 10^8$ charm-pairs and $\approx 10^6$ beauty-pairs per year of which only a small fraction can be measured however. Due to their large masses, top quark pairs cannot be produced.

1.3.1 Production mechanisms

The dominant process for the production of heavy quarks at HERA is photon-gluon fusion. The W or Z^0 exchange is suppressed due to the large masses of the heavy gauge bosons, and the scattering off heavy quarks in the proton can be neglected due to their small fraction. The main contribution to the cross-section is due to photoproduction so that the classification of the photoproduction processes in the previous section holds for the heavy quark production as well. Beyond the study of the direct processes, which is also possible in DIS, photoproduction allows an understanding of the resolved component to the heavy quark cross-section. Moreover, the study of the Q^2-dependence of the data from DIS and photoproduction allows a test of the QCD predictions on the hadronic structure of the photon.

For photoproduction in lowest order QCD ($O(\alpha \cdot \alpha_s)$), the direct process $\gamma + g \rightarrow q\ \bar{q}$ (Fig. 1.2a) is the main contribution to the cross-section. The photon-proton cross-section can be factorized in a photon-gluon cross-section $\sigma_{\gamma g}$ and a gluon density g [5, 6]:

$$\sigma_{\gamma p}^{PGF} = \int dx_g \; g(x_g, \ldots)\sigma_{\gamma g}(\hat{s}, m_q, \ldots) \tag{1.13}$$

These quantities depend on the momentum fraction of the gluon x_g, on the center of mass energy $\hat{s}$ of the heavy quark-antiquark pair, on the quark mass m_q, and additionally on the renormalization scale for the elementary interaction as well as on the factorization scale where the gluon density g in the proton is evaluated. The choice of these scales is not unique and usually scales related to the transverse momentum and the mass of the quark. The photoproduction cross-section $\sigma_{\gamma p}^{PGF}$ is then connected to the electron-proton cross-section according to Eq. (1.12).

Since the cross-section depends on the gluon density in the proton, its measurement provides a means for a *direct* determination of the gluon density.

At the high photon-proton center-of-mass energies that are reached at HERA, a large fraction the cross-section for heavy quarks is estimated to stem from resolved processes [7, 8]. Those are in leading-order QCD the gluon-gluon fusion and the quark-antiquark annihilation (Fig. 1.3). Furthermore, higher order terms contribute significantly to the cross-section. Corrections of the order of 50% have been calculated for the charm cross-section [9]. Some of the higher order processes are sketched in Fig. 1.4. The dominant contribution is the *gluon radiation* (Fig. 1.4, left) whereas the *quark radiation* (center) is negligible. Due to interference with the leading order process (the final state is the same), the process of order $O(\alpha \cdot \alpha_s^3)$ (right) contributes to the order $O(\alpha \cdot \alpha_s^2)$ as well.

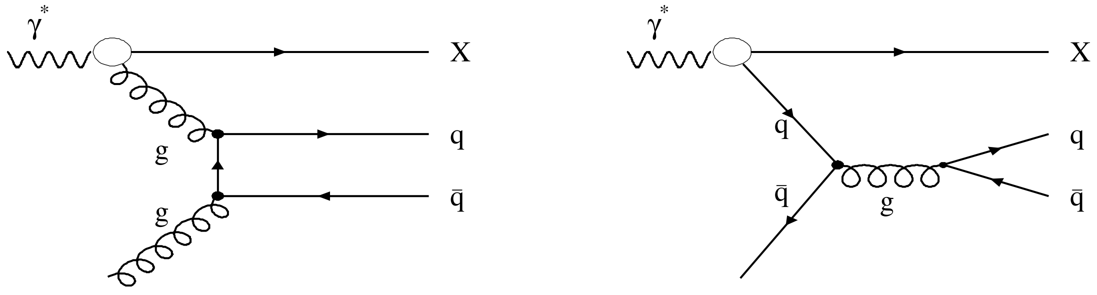

(a) gluon-gluon fusion

(b) quark-antiquark annihilation

Figure 1.3: *Resolved γp-interactions producing heavy quark pairs*

Both for charm- and beauty quark production at HERA, NLO-calculations have been performed [7]. In general, the uncertainties on the $b\bar{b}$-cross-section are smaller due to the higher mass of the b-quark. The results depend on the choice of the quark- and gluon density parameterizations, on the scale of the strong coupling constant Λ_{QCD}, and on the quark mass itself. Due to the additional freedom in the choice of the parameterization of the photon structure, the uncertainties on the hadronic component of the cross-section are greater than those on the direct component. Depending on the choice of the parameters, the fraction of resolved processes varies between 15% and 70% for charm quarks and between 15% and 40% for beauty quarks [8].

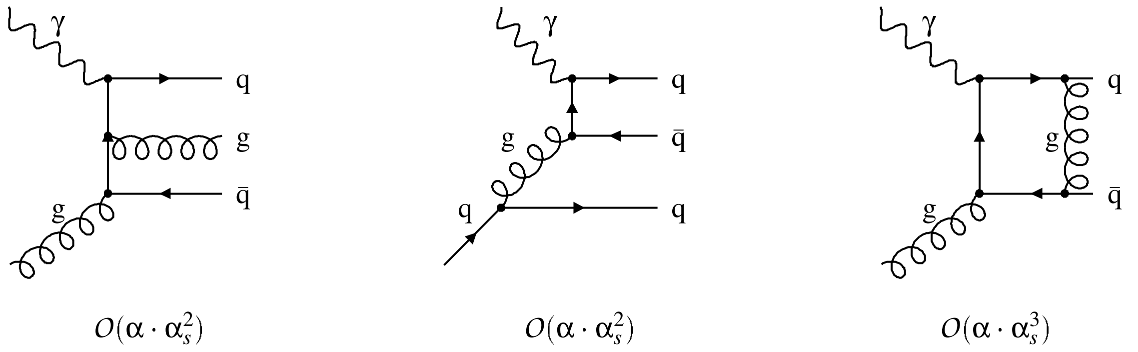

$O(\alpha \cdot \alpha_s^2)$ $O(\alpha \cdot \alpha_s^2)$ $O(\alpha \cdot \alpha_s^3)$

Figure 1.4: *Higher order processes of heavy quark photoproduction (direct component)*

1.3.2 Decays of heavy quarks

The heavy quarks that have been produced in the different hard subprocesses undergo fragmentation into hadrons. They can form bound states, the heavy quarkonia like $\mathrm{J}/\Psi(c\bar{c})$ or Υ $(b\bar{b})$, heavy mesons $(q_h q)$, or heavy baryons $(q_h qq)$. The bound states are commonly labelled *hidden* charm or beauty whereas the states formed separately by the quark and the antiquark are summarized as *open* charm or beauty.

Here, only the decays of heavy mesons shall be discussed further. A distinct property of them is their long lifetime. The $B^{\pm}$-mesons (composed of a b- and a u-quark) for instance have a mean life τ_B of $\approx 1.6\,\mathrm{ps}$ while for the $D^{\pm}$-mesons (composed of c and d) the mean life is $\tau_D \approx 1.0\,\mathrm{ps}$ [10].

This results in a characteristic signature in the detector: production vertex and decay vertex of the mesons are significantly separated and provide a means to detect processes involving heavy quarks. This topology is the reason that nearly all experiments in high energy physics attempt to measure their vertex positions to the highest possible precision by the employment of microvertex detectors [11]–[17].

The heavy mesons are bound by the strong interaction and decay weakly. The decay widths Γ are proportional to the elements of the Cabibbo-Kobayashi-Maskawa matrix (CKM) [18] that are fundamental parameters within the standard model. The flavour changing weak current can then be written as:

$$J = (\bar{u}, \bar{c}, \bar{t}) \begin{pmatrix} V_{ud} & V_{us} & V_{ub} \\ V_{cd} & V_{cs} & V_{cb} \\ V_{td} & V_{ts} & V_{tb} \end{pmatrix} \begin{pmatrix} d \\ s \\ b \end{pmatrix} \tag{1.14}$$

The CKM matrix describing the unitary transformations among three quark doublets can be characterized by three Euler angles and six phases (of which only one is of physical relevance). In a reduced model for only two quark generations, the mixing is specified by a single parameter and the CKM matrix reduces to the Cabibbo matrix:

$$V_{cab.} = \begin{pmatrix} \cos\Theta_c & \sin\Theta_c \\ -\sin\Theta_c & \cos\Theta_c \end{pmatrix} \tag{1.15}$$

with Θ_c being the Cabibbo angle. Charm quark decays can thus be classified in *Cabibbo-allowed* and *Cabibbo-suppressed* processes according to the magnitude of their matrix elements.

The dominant decay processes of heavy quarks are:

$$b \to c\mathrm{W}^- \qquad \text{and} \qquad c \to s\mathrm{W}^+ \tag{1.16}$$

The virtual W-boson decays either into a lepton-neutrino pair or hadronically into a quark-antiquark. In the framework of the *spectator model* the heavy quark decays as a quasi-free particle: the influence of the couplings to light quarks and gluons is neglected. A consequence of this model is the prediction of the decay widths for different mesons containing the same heavy flavour to be equal. However, a comparison with experimental results shows that this is only true for the *semi-leptonic* decay modes with the lepton pair and the hadronic spectator system in the final state. For the hadronic decay modes, additional interactions between the final-state hadrons have to be taken into account.

Experimentally, the semi-muonic decay modes of heavy mesons ($q_h \to q\mathrm{W} \to q\,\mu\nu_\mu$) are of particular interest due to the fact that muons can be measured in dedicated subdetectors with high efficiency. Therefore, for the study of heavy meson decays with data from the new microvertex detector of the H1 experiment that will be presented in Chap. 5, an event sample based on a muon selection is used. In addition to the elementary processes (1.16), cascade decays can contribute in the b-sector. The charm quark from the beauty decay can decay semi-muonically:

$$\begin{tikzcd} b \arrow[r] & \mathrm{W}^- c \arrow[dr] & & \\ & & \mathrm{W}^+ s \arrow[r] & \mu\, X \end{tikzcd}$$

Due to the beauty mass the decay $\mathrm{W}^- \to c\bar{s}$ is kinematically possible which results in a further contribution to the cascade decay. Tab. 1.1 shows theoretical and measured branching ratios for heavy quarks decaying into muons. The theoretical values are calculated in the framework of the spectator model, and the values for the quark masses were $m_c = 1.87\,\mathrm{GeV}/c^2$ and $m_b = 5.27\,\mathrm{GeV}/c^2$.

quark	theor. [%]	exper. [%]			ref.
c	11	8.6	±1.7	$^{+0.8}_{-0.7}$	[19]
		9.6	±1.1		[20]
b	11	10.2	±0.5	±0.2	[21]
		10.5	±0.5		[20]

Table 1.1: *Theoretical and experimental branching ratios for heavy quarks decaying into muons.*

The primary goal of employing a microvertex detector is the separation of background events stemming from light quark production from the heavy quark events. This is achieved by exploiting the event topologies that are characterized by secondary vertices. Typical decay lengths of heavy mesons are of the order of $c\tau \sim 100\,\mu$m and the detector vertex resolution hence has to be of the same order.

Due to the ratio of the production cross-sections at HERA, c-quark decays are accessible more easily than b-quark decays. On the other hand, since the scale for perturbative calcuations is harder in the b-sector due to the higher b-mass, the theoretical uncertainties are considerably lower. Therefore, a separation of the b-quark from the c-quark domain is a second important issue for microvertex detectors.

A precise spectroscopy of heavy flavoured mesons provides access to a number of interesting physics issues:

- the observation of *rare* decays. In the charm-sector, those processes are the doubly Cabibbo suppressed decays, where the magnitude of the Cabibbo-matrix element for the c-decay as well as for the decay of the W-boson prohibits the transition, e.g. $c \to d\mathrm{W}^+ \to du\bar{s}$. Other rare processes are those that can only be represented by loops in the Feynman diagrams, like penguin diagrams, flavour changing neutral currents or the $D^0\bar{D}^0$ mixing (Fig. 1.5). In general, loop level processes are sensitive to the existence of new, heavy particles.

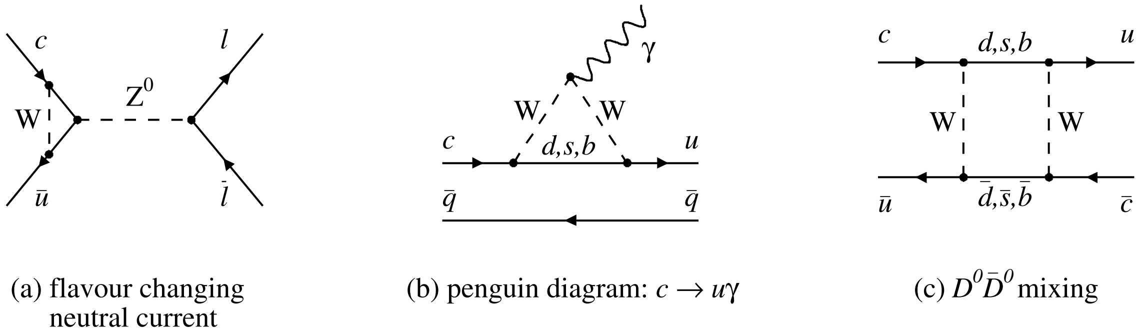

(a) flavour changing neutral current

(b) penguin diagram: $c \to u\gamma$

(c) $D^0\bar{D}^0$ mixing

Figure 1.5: *Rare charm decays on the loop level*

In the b-sector, the charmless b-decays are rare processes of interest.

- studies of *mixing* of the neutral D- and B-mesons. In the charm sector, the mixing rate is small compared to the K^0 or B^0 mesons. Moreover, the process $D^0 \to \bar{D}^0 \to K^+\pi^-$ has the same final state as the doubly Cabibbo suppressed D^0-decay. The two processes can only be distinguished by measuring their time evolution. The resolution needed is of the order $O(0.5 \cdot \tau_{D^0})$ which corresponds to a vertex resolution of $\approx 50\,\mu$m.

- investigations on *forbidden* decays, e.g. lepton number violating decays like $D^0 \to \mu^+ e^-$ that are forbidden to all orders in the standard model, and the observation of which would hence be a signal for new physics.

- the extraction of the gluon density. Complementary to the indirect methods using structure function analyses, direct measurements that are based on measurements of heavy mesons are possible. A recent method [22] used the decay of the charmed D^*-meson to determine the differential cross-section $d\sigma/dx_g$ from which the gluon density was unfolded.

- the determination of the b-quark production cross-section. Recent analyses at HERA [8, 23] give an indication that the cross-section is considerably larger than the expectation from leading order calculations.

In any case, a deepened knowledge on the decay mechanisms of heavy mesons also gives rise to a better understanding on their production.

Chapter 2

The H1 detector at the *ep*-collider HERA

In this chapter the accelerator HERA and the detector H1 are portrayed. It is then focussed on the reconstruction of tracks in the central region of H1, and on the microvertex detector CST that has begun its operation in 1997.

2.1 The *ep*-storage ring HERA

The storage ring HERA[1] at DESY in Hamburg (Fig. 2.1) is the world's only facility for electron-proton collisions. The particles are being injected through several pre-accelerators into two separate machines with a circumference of 6.4 km each. They are then accelerated to energies of 27.5 GeV and 820 GeV for electrons and protons respectively. The *ep*-center-of mass energy is thus $\sqrt{s} \approx 300\,\mathrm{GeV}$. Up to 1993, HERA was operated using electrons, afterwards with positrons whose lifetime in the beam pipe is three times as large. With an improved vacuum system installed, it is planned to switch to electron fills again in 1998[2].

		design		1997	
		e	p	e	p
beam energy	[GeV]	30.0	820	27.6	820
avg. beam current	[mA]	58	163	28	74
number of bunches		220	220	175	175
avg. luminosity	[$\mathrm{cm}^{-2}\mathrm{s}^{-1}$]	1.5×10^{31}		4.27×10^{30}	
avg. specific luminosity	[$\mathrm{cm}^{-2}\mathrm{s}^{-1}\mathrm{mA}^{-2}$]	4.0×10^{29}		4.82×10^{29}	
integrated luminosity	[nb^{-1}]			32400	

Table 2.1: *Parameters of the storage ring HERA*

Both the electron and the proton beams are structured in particle bunches of which up to 220 can be filled into each ring. This corresponds to a bunch crossing frequency of 10.4 MHz. In 1997, 175 colliding *e*- and *p*-bunches were injected for luminosity production. Additionally, some bunches without partner (*pilot bunches*) provide a means to study background processes induced by beam-gas

---

[1] **H**adron-**E**lektron-**R**ing-**A**nlage

[2] In the following, only the term electron will be used when related to the incoming or scattered lepton.

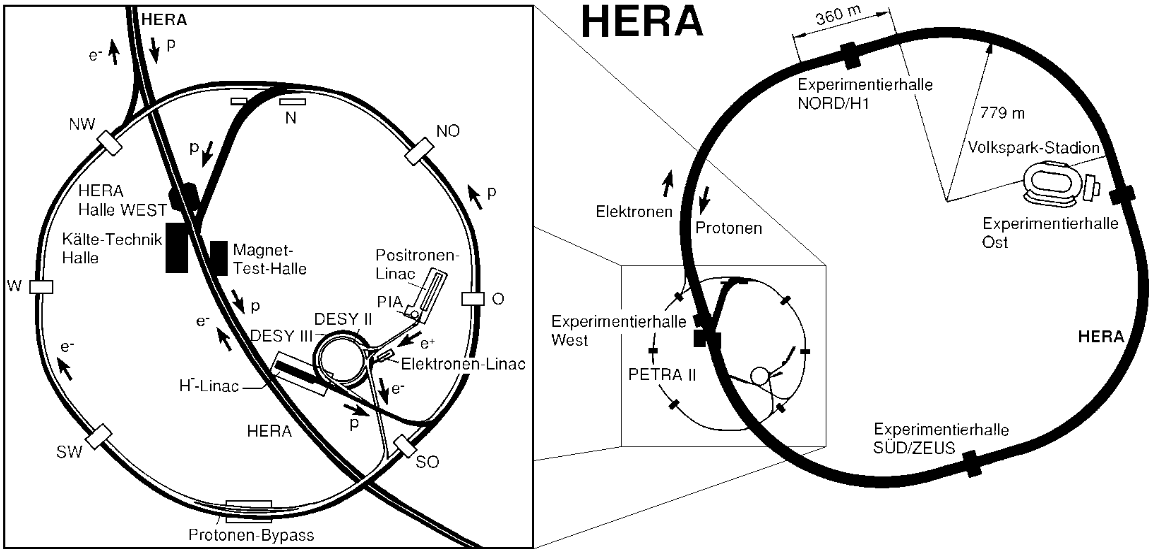

Figure 2.1: *The electron-proton collider HERA. The zoomed view on the left displays the injectors and pre-accelerators while the storage ring itself with the four experiment areas is shown on the right. The H1 experiment is situated in the north section of the ring.*

or beam-wall events. The duration of a luminosity run is typically 10 h and is determined by the electron beam lifetime. Some parameters of the HERA accelerators are shown in Tab. 2.1.

The beams collide at two interaction regions where the experiments H1 and ZEUS are located. In two other detector areas the fixed target experiments HERMES and HERA-*B* are situated. HERMES was designed to study the spin structure of nucleons. It uses the longitudinally polarized electron beam and a polarized gas target. HERMES is operational since 1995 and has already published results on the spin structure function of the proton [24]. HERA-*B* is currently under construction [25] and expected to begin with its physics program in 1999. The aim is to study the *CP*-violation in the $B^0\bar{B}^0$-system. The *B*-mesons will be produced by moving an aluminum wire target into the halo of the proton beam.

2.2 The H1 detector

The H1 detector (Fig. 2.2) is a universal particle detector designed to measure tracks and energies of the particles produced in *ep*-collisions [26]. It covers almost all of the solid angle range and is instrumented asymmetrically taking into account the different momenta of the incoming particles: the final state particles tend to be boosted in the proton direction. The main detector has a weight of 2800 t and measures $12 \times 15 \times 10\,\text{m}^3$.

The proton direction defines the z-axis of the right-handed H1-coordinate system. Its origin is at the nominal interaction point with the x-axis pointing towards the center of the HERA ring and the y-axis pointing upwards. The polar angle Θ is defined with respect to the z-axis from 0° at $+z$ to 180° at $-z$. Small values of Θ define the "forward" direction. The azimuthal angle Φ extends from the positive

1 Beam pipe and beam magnets
2 Central tracking devices
3 Forward tracking devices
4 Electromagnetic LAr calorimeter
5 Hadronic LAr calorimeter
6 Superconducting coil ($B = 1.15\,\mathrm{T}$)
7 Compensating magnet
8 Helium cryogenics for 7
9 Muon chambers
10 Instrumented iron yoke
11 Forward muon toroid ($B = 1.6\,\mathrm{T}$)
12 Backward drift chamber and calorimeter
13 Plug calorimeter
14 Concrete shielding
15 Liquid argon cryostat

Figure 2.2: *Schematic layout of the H1 detector. The numbers will be referred to in the text.*

x-axis towards positive values for the upper detector half and up to $-180°$ for the lower half.

In the following, the main components of the detector are introduced. Numbers in boxes refer to Fig. 2.2.

Track detectors

In the inner part of the apparatus the track and vertex detectors are installed. The central part $\boxed{2}$ consists of:

- a silicon strip *microvertex detector* CST[3] for the precise determination of primary and secondary vertices. The CST was installed in 1996 and began regular data acquisition in 1997. As the subject of this thesis, it is described in detail in Chap. 2.4.
- two *jet chambers* CJC1 and CJC2[4]. Their signals are the basis for the track reconstruction in the central region and are also used for particle identification utilizing the dE/dx-information. The CJC has a track resolution of $\approx 150\,\mu$m in the R-Φ-plane and of ≈ 3 cm in z. The chambers and the principles of the track reconstruction are described in Chap. 2.3.
- two *drift chambers* CIZ and COZ[5] for improving the track resolution in the z-coordinate. Their signal wires are mounted in a polygon-shaped manner concentrically around the beamline. The CIZ is subdivided into 15 cells with four wires each, the COZ into 24 cells. The position resolution is $\sigma_{rz} \approx 350\,\mu$m.
- two *proportional chambers* CIP and COP[6] that deliver signals for the H1-trigger system. Their signal wires are strung parallel to the beamline and they are segmented into 60/18 Rz-pads and 16/16 $R\Phi$-pads.

The tracking chambers are mounted cylindrically around the beam pipe and the vertex detector in two radial layers of proportional chamber – z-chamber – jet chamber. (Fig. 2.3). The geometrical acceptances for the different detectors are shown in Tab. 2.2.

	radial		z		polar	
	min [mm]	max [mm]	min [mm]	max [mm]	min [°]	max [°]
CST	57.5	95	-175	175	30	150
CIZ	174	200	-1080	720	13.6	170.8
CJC1	203	451	-1125	1075	10.7	169.7
COZ	460	485	-1105	1055	23.6	157.3
CJC2	530	844	-1125	1075	26.3	154.7

Table 2.2: *Active regions of the central tracking chambers*

In the forward region $\boxed{3}$ a system of three identical supermodules each consisting of *radial* and *planar drift chambers*, a *proportional chamber*, and a *transition radiation module* is installed. Particles from

---

[3] Central **S**ilicon **T**racker

[4] Central **J**et **C**hamber

[5] Central **I**nner **Z**-chamber, **C**entral **O**uter **Z**-chamber

[6] Central **I**nner **P**roportional chamber, **C**entral **O**uter **P**roportional chamber

the interaction region first traverse three planar drift chambers that are rotated by 60° in azimuth with respect to each other. The signal wires are parallel to each other and orthogonal with respect to the beam axis. The planar chambers measure the x- and y-coordinates of the particle track to an accuracy of $\approx 170\,\mu$m. The adjacent proportional chamber generates trigger signals. The transition radiation module is intended to separate high energetic pions and electrons. Finally, a drift chamber with wires strung radial to the beam axis measures additional points on the track achieving an R-Φ-resolution of $\approx 200\,\mu$m. The angular coverage of the complete forward tracking system is $5° < \Theta < 30°$.

A complete view of the tracking system together with the backward detectors (s. below) is given in Fig. 2.3.

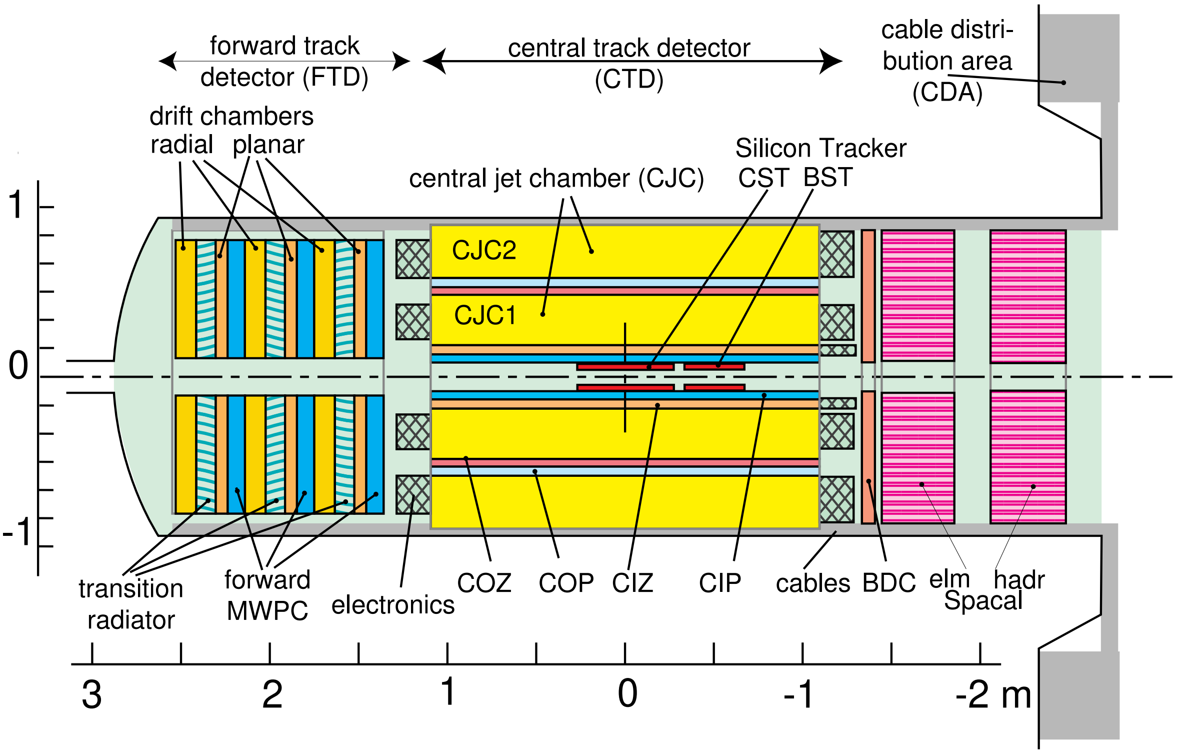

Figure 2.3: *Side-view of the tracking detectors*

Detectors in the backward region

The backward region $\boxed{12}$ of the H1 detector has been upgraded in 1995/96 in order to increase the acceptance for events with low x and Q^2 characterized by small scattering angles of the electron[7] [27]. New components are:

- The *backward silicon tracker* BST consisting of four disks with silicon strip detectors. The disks are mounted around the beam pipe between $z = -725.4$ mm and -949.8 mm resulting

---

[7] Due to the orientation of the coordinate system, this is equivalent to large values of the polar angle Θ.

in a good coverage of the polar angle of $172^\circ < \Theta < 176^\circ$. The detectors are single-sided and have arc-shaped strips of $48\,\mu$m pitch width oriented concentrically with respect to the beamline. The inner radius of the active material is 57.3 mm, the outer 120 mm. A resolution of $12\,\mu$m has been measured. The BST shares its readout system with the CST which is described in Chap. 3.1.

- The *backward drift chamber* BDC measuring the position of particles scattered in the backward region ($153^\circ < \Theta < 177^\circ$) [28]. It is subdivided into four double layers that consist of eight sectors each. The sense wires follow this octogonal shape, resulting in an almost radial drift direction for optimal polar angle resolution. For the backscattered electron in DIS processes, the resolution is better than 1 mrad.

- The *backward calorimeter* SPACAL[8] with an electromagnetic and hadronic part both consisting of a lead–scintillating fibre matrix. The fibres are parallel to the beam axis and are being read out by photomultipliers. The SPACAL covers the region of $153^\circ < \Theta < 177.8^\circ$ and reaches an energy resolution for electrons of $7\% / \sqrt{E} \oplus 1\%$ [29]. The electromagnetic part is subdivided into 1192 cells of $4 \times 4\,\mathrm{cm}^2$ cross-section resulting in a position resolution for a shower of < 4 mm. The time resolution being better than 1 ns allows an efficient background rejection.

Calorimetry

The tracking detectors are surrounded by a *liquid argon calorimeter* that measures energies of particles scattered into the central or forward region (polar acceptance: $4^\circ < \Theta < 153^\circ$). It is segmented longitudinally into eight "wheels" each of which is subdivided in Φ into eight identical stacks (Fig. 2.4). The calorimeter is composed of an electromagnetic $\boxed{4}$ and a hadronic part $\boxed{5}$ that both use liquid argon as active material and lead and stainless steel as absorber respectively. The electronic energy resolution is $12\% / \sqrt{E_e} \oplus 1\%$, the resolution for pions $50\% / \sqrt{E_\pi} \oplus 2\%$. Both parts of the

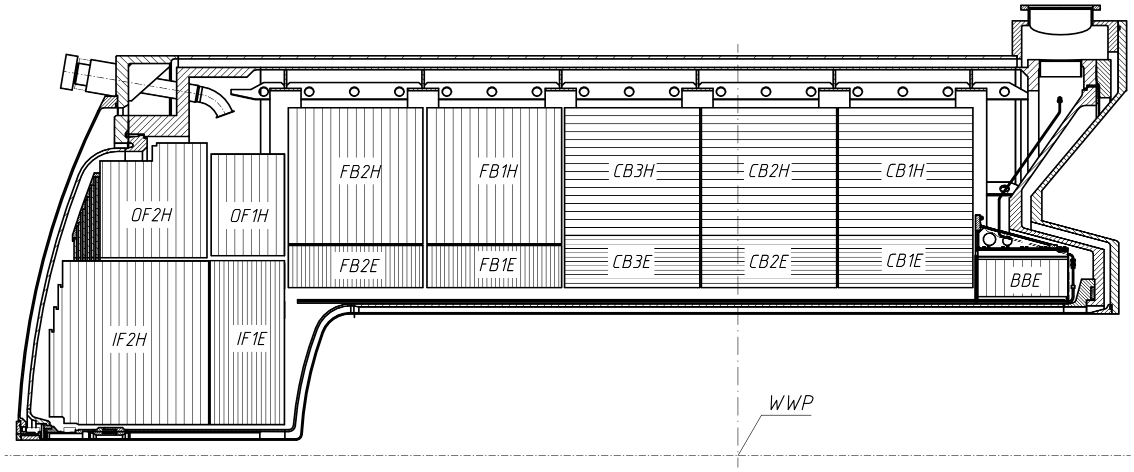

Figure 2.4: *Side view of the liquid argon calorimeter showing a cross-section of the eight wheels (left to right). The protons enter from the right,* WWP *denotes the nominal interaction point.*

---

[8] **Spa**ghetti-**Cal**orimeter

calorimeter are non-compensating which means that the signals for hadrons are smaller than for electrons of the same energy. During the reconstruction the hadronic energies have thus to be reweighted. The systematic error on the scale of the hadronic energies is currently $\approx 4\%$.

The polar angle in the extreme forward direction range up to the beam pipe ($4^\circ > \Theta > 0.6^\circ$) is covered by the *plug-calorimeter* $\boxed{13}$ for hadronic energy measurements. It consists of copper absorbers and silicon detectors.

Magnet

The tracking detectors and the calorimeter are surrounded by a magnet consisting of a superconducting coil $\boxed{6}$ and an iron return yoke $\boxed{10}$. The coil is mounted inside a cryostat with a length of 5.75 m and an outer diameter of 6.08 m. The mean magnetic field in the region of the central trackers is 1.15 T. In order to minimize its impact on the HERA beams, a second superconducting coil $\boxed{7}$ is installed at $z = -4.4$ m that compensates the longitudinal component of the main field.

Muon detectors

The iron return yoke of the magnet $\boxed{10}$ is instrumented with streamer tubes for the detection of muons and of remaining energy from hadronic showers leaking out from the calorimeter. 10 chamber layers are interleaved between the iron slabs, and 3 layers are attached on the inside and on the outside respectively (Fig. 2.5). At polar angles of $\Theta = 90^\circ$, muons have to have an energy greater than 1.2 GeV to reach the first layer, and greater than 2.0 GeV to traverse the iron yoke completely. The polar angle range covered is $5^\circ < \Theta < 170^\circ$. The streamer chambers have a single sense wire in the middle of their cross-section of $1 \times 1\,\mathrm{cm}^2$. Five layers are equipped with strip electrodes mounted perpendicular to the wires that are used for position measurements along the wire direction. The other layers have pad electrodes whose hit information is used for resolving track ambiguities. In the central region (*barrel*) the wires are strung parallel to the z-axis, while in the forward and backward direction (*endcaps*), they are parallel to x. The position resolution is ≈ 4 mm perpendicular to the wires and ≈ 1.2 cm along the wires. The momentum resolution in the central region is $\sigma_p/p \approx 35\%$ in the barrel. The iron together with the pad electrodes additionally serves as a tail-catcher measuring the hadronic energy leaking from the calorimeter.

In front of the iron yoke (in proton direction) a *forward muon spectrometer* is installed. It consists of three drift chamber layers in front of and behind a toroid magnet $\boxed{11}$ generating a mean magnetic field of 1.6 T. It is intended for the detection of high-energetic muons ($5 < E_\mu < 200$ GeV) in a range of $3^\circ < \Theta < 17^\circ$.

Luminosity detectors

The system for the luminosity measurements (not shown in Fig. 2.2) consists of two small crystal Cherenkov calorimeters, namely a photon detector of $100 \times 100\,\mathrm{mm}^2$ and an electron tagger of size $154 \times 154\,\mathrm{mm}^2$. They are located in the HERA tunnel at $z = -102$ m and -33.4 m respectively. The photon detector is protected against synchrotron radiation by a lead filter with a thickness of 2 radiation lengths X_0 followed by a water Čherenkov counter used as a veto detector against photons interacting in the lead.

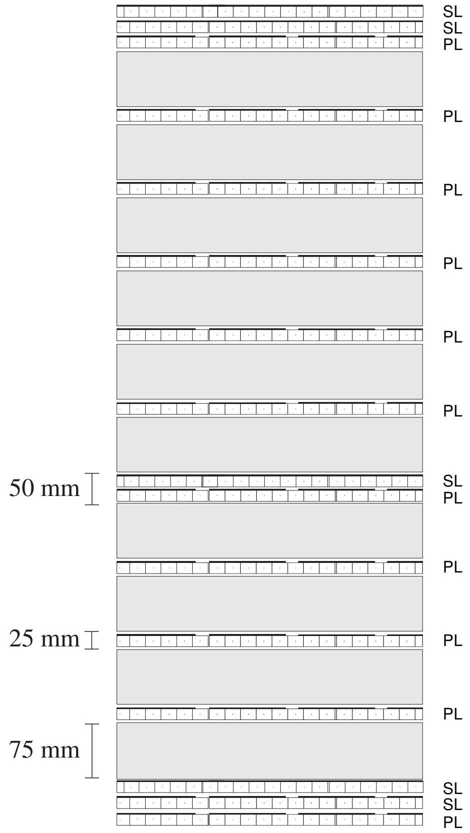

Figure 2.5: *Cross section of the central muon detector. PL denotes layers with pad electrodes, SL those with strip electrodes.*

The reaction for determining the luminosity in the interaction region is the Bethe-Heitler-Bremsstrahlung process:

$$ep \to ep\gamma$$

the cross-section of which is well-determined in QED. The main background source is bremsstrahlung from interactions of the electron beam with the residual gas in the beam pipe. These events can be subtracted using data from electron pilot bunches. The luminosity is calculated as:

$$\mathcal{L} = \frac{R_{tot} - (I_{tot}/I_0)\,R_0}{\sigma_{vis}} \tag{2.1}$$

with R_{tot} and R_0 being the total rate of bremsstrahlung events and the rate from the pilot events respectively, I_{tot} and I_0 the corresponding beam currents, and σ_{vis} being the visible $ep \to ep\gamma$ cross-section. For the offline determination of the luminosity, only information on the radiated photon is employed in order to minimize the systematic error. The principle of the measurement is sketched in Fig. 2.6.

The electron tagger together with a second device at $z = -44$ m is additionally used for the detection of the scattered electron in photoproduction events. The covered kinematic region is $Q^2 < 0.01\,\mathrm{GeV}^2$, $0.3 < y < 0.7$ for the 33 m-tagger and $0.08 < y < 0.18$ for the 44 m-tagger.

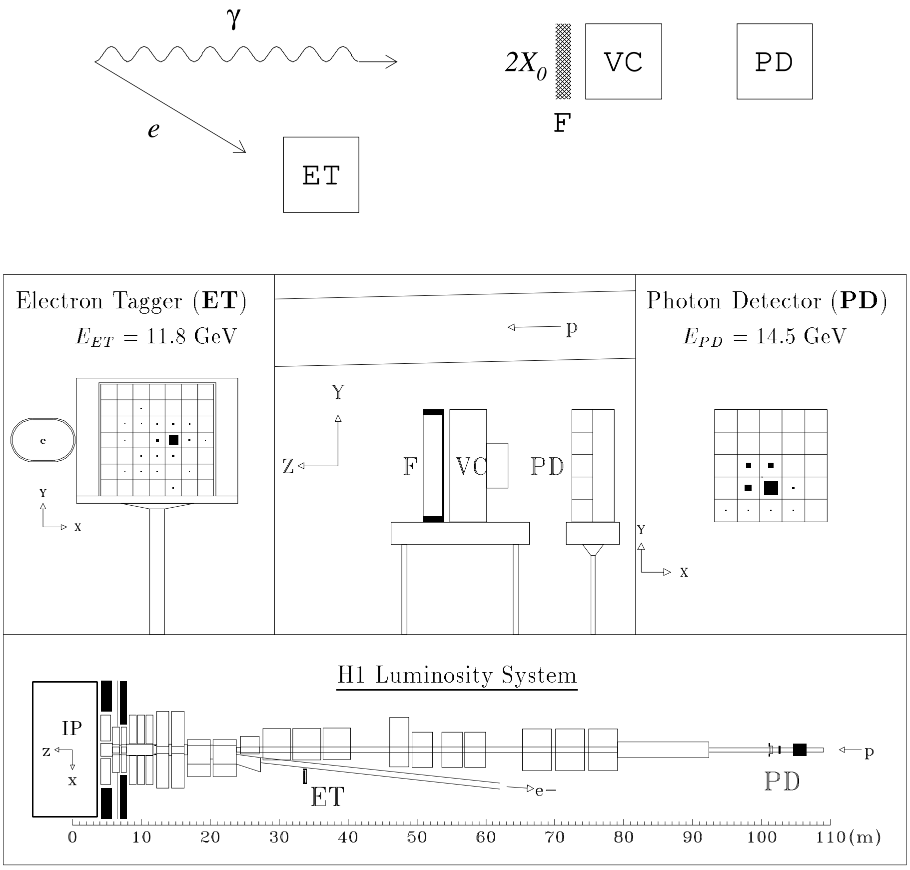

Figure 2.6: *Luminosity detectors and principle of the measurement. The electron radiates a photon which is measured in the photon detector (PD) after having traversed the lead filter (F) and the Čherenkov-counter (VC).*

Time-of-flight system and veto-wall

In order to suppress background events induced by the proton beam before it reaches the interaction region, the H1 detector uses two systems of scintillation counters. The *time-of-flight system* has two scintillator planes at $z = -1.95$ m and -2.25 m. Particles entering the back of the detector in the direction of the proton beam, i.e. that do not originate from the interaction region, can be identified using the time-of-flight difference of ≈ 13 ns with respect to particles from *ep*-interactions.

The *veto-wall* consists of two walls of scintillator planes at $z = -6.5$ m and -8.1 m. Both walls are composed of an inner and outer plane and identify particles by measuring the time-coincidences. The time resolution for an inner-outer-coincidence is 3 ns for the inner wall and 8 ns for the outer.

Trigger system

While the HERA bunch crossing frequency is 10.4 MHz, the actual rate of physical interactions is ≈ 100 kHz only. It is the task of the trigger system to filter out the events of physics interest and to reject the background events. This is achieved by means of a multi-stage triggering system consisting of hardware and software levels reducing the final event rate written to tape to ≈ 5 Hz. Dominant background processes are:

- *beam-wall events* where protons or electrons interact with the beampipe walls
- *beam-gas events* where interaction with remaining gas molecules in the beampipe takes place
- *synchrotron radiation* from the electron beam
- *beam halo muons*
- *cosmic muons*

The *first-level trigger* (L1) is a complex hardware logic that makes use of information from the different subdetectors (trigger elements) and combines it into so-called subtriggers. Since this process cannot be completed within the time span of 96 ns between two bunch crossings, the subdetectors have to store their event information in pipelines until a trigger decision is made. This is also necessary since the response time of some subdetectors may be considerably longer than a bunch crossing (e.g. due to preamplifier integration times or drift times in chambers). The L1 trigger decision is available after 24 bunch crossings. It can be initiated by any subtrigger and starts the full readout of the detector components as well as invoking the higher trigger levels. As a consequence of the pipelined architecture, the first-level trigger runs inherently dead-time free. First-order dead-time starts only after a `L1keep`-signal when the front-end pipelines are stopped and their readout is initiated.

The *second-level trigger* (L2) consists of two independent systems that work in parallel and deliver their decision within $20\,\mu$s:

- a topological trigger
- a neural network trigger implemented on several parallel computers

Both systems are able to investigate detector signal correlations on a much larger scale than the first-level trigger. It is only after a positive decision of L2 that some of the time consuming readout steps for the subdetectors are initiated (e.g. the multiplexed front-end readout and subsequent hit detection for the silicon trackers or the zero-suppression of the drift chamber signals).

The *third-level trigger* (L3) is foreseen to give the possibility to perform more sophisticated calculations though it is not implemented yet. Its decision time is 2 ms, and determines the time limit for the complete readout of all subdetectors.

In 1997, typical output rates of L2/L3 were 50-100 Hz that had to be managed by the central data acquisition system. No additional dead-time is introduced since the L2/L3 system runs asynchronously to L1.

The last trigger instance before data storage is the *level 4 filter farm* (L4). It consists of ≈ 30 processor boards[9] each having the full raw data of one event available for making the final decision on accepting. The decision step comprises the partial reconstruction of an event using software of the standard offline reconstruction as well as dedicated fast filter algorithms. The software is organized in terms of logical modules executed “on top” of each other. Processing is terminated and the event rejected as soon as one module finds a filter condition to be false. The farm is also employed for monitoring (online histograms) and calibration purposes. Calibration data are written to a database and can thus be used by the online reconstruction of the accepted events (s. below).

---

[9] In 1997, part of the boards were MIPS R 3000, and part were PowerPC 604 based.

Data acquisition system

The data acquisition system for the H1 detector has to cope with the data of $\approx$400000 analog channels producing a total of some 4 Mbytes of digitized raw data. The system is built around the VMEbus standard and subdivided into 12 readout branches, each being mastered by a VMEtaxi module. These provide the possibility to interconnect the readout crates by means of fibre optic links, forming a ring. The master processor of the ring assembles the data of all branches, building full-event units which can then be distributed to several "consumers", subsystems monitoring (like the event display), filtering (the L4 farm), or recording data on permanent storage media. The consumers can in turn feed back data into the stream, e.g. additional data calculated on the L4 farm. Processor communication over the fibre-optic ring is established via memory-mapped mailbox protocols, so that no operating system is required to run on the processors.

The input data to the full-event units are produced in parallel by the readout branches, if the L1 and L2 trigger decisions have been positive. By specific compression and formatting algorithms (e.g. cluster-finding for the silicon trackers) the raw event size is reduced to $\approx$ 100 kBytes. Apart from the VMEtaxi processor the system architecture is autonomous in all branches. The silicon trackers for instance use a second fibre optic ring to transfer their data to the VMEtaxi processor (cf. Chap. 3.1).

The final event records are sent to an SGI challenge computer where the full event reconstruction (commonly referred to as L5) takes place. Its task is essentially to convert the digitized hit information from the subdetectors into physical quantities, namely tracks and energy clusters. The process is organized modularly, starting with separate tasks for each of the subdetectors and later combining information from different modules, e.g. track linking of the different track detectors or linking of central tracks and tracks measured in the muon detectors.

The reconstruction also performs a *classification* of the events which means that criteria motivated by physics selections have to be met. If an event cannot be classified, it is rejected.

Both raw data and reconstructed data are stored on tapes[10], while the last reconstruction step produces also a compressed subset of the reconstructed data (DST[11]) that are stored on hard-disks and are the basis for physics analyses.

2.3 Track reconstruction with the central jet chambers

In this section, the central jet chambers being the most important subdetector for the reconstruction of central tracks are introduced in more detail. From the measurements of the tracks a primary vertex can be determined in most of the events. With the information from the new microvertex detector CST which will be introduced in the next section, a considerable improvement in resolution is possible. This will be achieved by recalculating the track parameters employing CJC as well as CST information and hence depends —among other items— on the consistency and efficiency of the CJC reconstruction. Here, the methods applied for the track finding in the CJC are therefore described in more detail while the event reconstruction with the microvertex detector will be discussed in Chapter 4.

---

[10] The latter are the **P**hysics **O**utput **T**apes (POT)

[11] **D**ata **S**ummary **T**apes

2.3.1 Chamber architecture and readout

The CJC is radially divided into two sections from radii of $R = 20.3$ cm to 45.1 cm (CJC1) and from $R = 53.0$ cm to 84.4 cm (CJC2). The drift cells are made up of a plane of anode sense wires adjacent to two cathode wire planes that shape the drift field. The cells extend over the full radial span of CJC1 and CJC2, hence the influence of field shaping wires at the inner and outer radii is minimized. The potential on the cathode wires is proportional to their distance from the sense wires creating a uniform drift field over all of the the cell. The CJC1 has 30 cells consisting of 24 sense wires and 49 cathode wires each, the CJC2 has 60 cells with 32/66 wires. A radial cross-section is shown in Fig. 2.7.

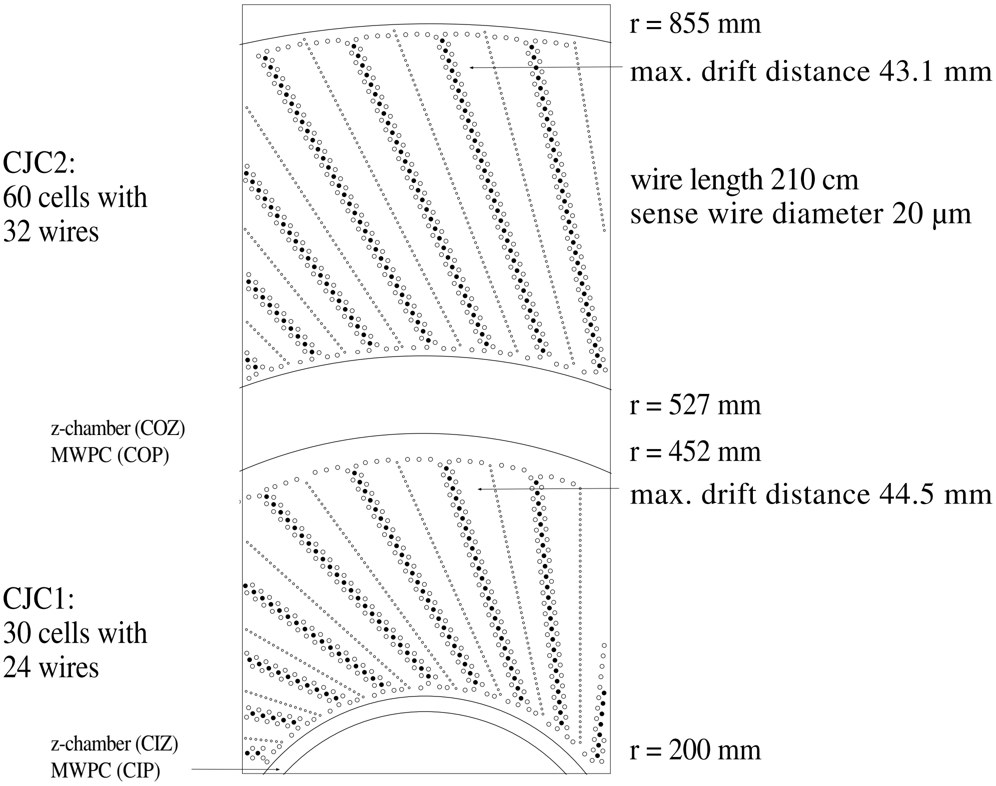

Figure 2.7: *Radial view of the central jet chambers. Note the tilted cell geometry as well as the two potential wires separating adjacent sense wires.*

Neighbouring sense wires are separated by two potential wires allowing an almost independent adjustment of drift field and gas amplification and reducing cross-talk efficiently.

The jet cells are tilted by about 30° in azimuth resulting in an electron drift direction (in the presence of the magnetic field) that is almost perpendicular to tracks originating from the center. Apart from giving optimal track resolution, this geometry helps to resolve ambiguities by connecting track segments from neighbouring cells. Due to the fact that a track crosses the sense wire plane at least once, the passing time can be determined to an accuracy of ≈ 0.5 ns which allows the separation of tracks from different bunch crossings.

The 2640 sense wires are read out at both ends via preamplifiers mounted at the chamber end walls. The analog signals are transferred via some 28 m of coaxial cable to electronics modules where they are continuously being digitized by FADCs at a sampling frequency of 104 MHz. The digital data are then written to “circular buffers” that store information of the last 25 bunch crossings at any time to allow for the decision time of the first-level trigger.

Upon the reception of a trigger signal, in each readout crate[12] the data from the desired time slice are copied by scanner cards into a central memory. During the copy a hit-table is set up by comparing the data to programmable thresholds. Using the hit-table information, a microprocessor then copies the reduced data to the master readout crate of the central tracker branch. Here, an analysis of pulse-charge integral and signal timing (Qt-analysis) is performed by PowerPC processors. The output data of the CJC for the subsequent track finding in the reconstruction processes are then the charges on both wire ends and the drift time for every hit found.

2.3.2 Track finding

Due to the solenoidal magnetic field, tracks of charged particles in the CJC are curved in the R-Φ-plane. They can be parameterized by means of a helix described by five parameters listed in Tab. 2.3. To a good approximation, the parameters in the R-Φ-plane and those in the R-z-plane are independent.

			value range
curvature (inverse radius)	[cm^{-1}]	κ	$-\infty \ldots +\infty$
closest distance to origin	[cm]	dca	$-\infty \ldots +\infty$
azimuthal angle at *dca*	[rad]	Φ	$-\pi \ldots +\pi$
polar angle at *dca*	[rad]	Θ	$0 \ldots \pi$
intersection with z-axis at *dca*	[cm]	$z0$	$-\infty \ldots +\infty$

Table 2.3: *Parameters for a helix track in a solenoidal magnetic field*

κ, Φ, and *dca* are determined by means of a circle fit in the R-Φ-plane [30], whereas Θ and $z0$ are obtained from a straight line fit in R-z. The sign convention for κ and *dca* is chosen in a way that

- tracks of positively charged particles have negative curvatures
- upon the change of the sign of one parameter, the sign of the other remains the same, e.g. two stiff tracks differing only in their charge (sign of κ) would have the same sign of the *dca*.

Φ, Θ, and $z0$ are defined as in the H1-coordinate system.

The primary quantities measured by the CJC are the drift times t and the charges Q^+ and Q^- at both wire ends. The drift path length s from the position of the traversing particle to the sense wire can be calculated as

$$s \approx v_D \cdot (t - t_0) \tag{2.2}$$

due to the constant drift velocity v_D in the cells ($t - t_0$ is the time difference between the particle crossing and the generation of the signal). A measurement on several sense wires allows the reconstruction of a particle track in the R-Φ-plane. One has to consider the fact that the drift direction deviates from the direction of the electric field due to the presence of the magnetic field (Lorentz-angle). For the

---

[12] Using 16-channel FADC cards, 23 crates are needed for the CJC readout.

CJC, this effect is partly compensated by the azimuthal tilt of the cells. From the charges at both ends the z-coordinate along a sense wire of a passing track can be reconstructed since the wire acts as a voltage divider:

$$z = \frac{Q^+ - Q^-}{Q^+ + Q^-} \tag{2.3}$$

The track reconstruction hence involves several calibration constants like the bunch crossing time t_0, the Lorentz-angle, and the drift velocity v_D. Due to the chamber geometry with tracks crossing signal and cathode wire plane at least once, it is possible to extract these constants from the CJC data: the chamber is *self-calibrating* [31].

The track finding program exists in two versions: a fast one that is implemented on the L4 filter farm and employed for background rejection and the preliminary classification of events, and the standard version being part of the complete reconstruction program (L5). The former looks for tracks with a transverse momentum $p_t > 100\,\mathrm{MeV}$ originating from the primary vertex. Its results allow background rejection, a preliminary event classification, and the extraction of calibration constants. The standard version is slower by a factor of ten, but efficient for all kinds of tracks. It makes use of the results of the fast version.

Both programs consist of three steps:

- the determination of the bunch crossing time t_0
- the search for short track elements consisting of three hits within a given cell
- the definition of tracks by means of the determination of the helix parameters

Due to the higher accuracy of the R-Φ-measurements, the track finding starts in the R-Φ-plane. Short track elements are connected and matched, first within a cell, next between adjacent cells, then within the two chambers, and lastly between CJC1 and CJC2. Θ and $z0$ are determined by means of a straight line fit of the z-coordinates of the hits afterwards. The set of tracks obtained in this manner is referred to as *non-vertex-fitted tracks*.

The intrinsic resolutions for a single hit in the CJC have been measured to be $195\,\mu\mathrm{m}$ in R-Φ and 2.2 cm in the z-coordinate. Studies on the resolution of the track parameters using cosmic tracks are reported in Chap. 4.6.

2.3.3 Vertex matching

A further reconstruction step then makes use of the knowledge of the primary vertex position. By means of treating it as an additional point for a non-vertex-fitted track, and recalculating the track parameters by means of *constraining* them to the vertex, the resolution can be improved considerably.

The vertex position is obtained utilizing the fact that the beam position in the H1 detector is stable over long time periods. By means of collecting well-measured tracks from many events, and minimizing the *dca* by applying a least squares method the average x- and y-coordinates of the interaction point (at $z = 0$) can be calculated[13]. These *run-vertex* coordinates are determined for every data-taking run

---

[13] Actually, the beam position in x and y depends on the z-coordinate (beam-tilt). Therefore, slopes for x vs. z and y vs. z are determined additionally.

consisting of several thousands of events. Their uncertainty is given by the radial extensions of the beams, which are $\approx 180\,\mu$m in x and $\approx 50\,\mu$m in y. Since the coordinates are determined on the L4 filter farm, the reconstruction program on L5 can make use of them.

The accuracy of the run-vertex position in x and y is greater than the one that could be achieved by performing an event-wise vertex fit. The primary vertex of any event is thus always determined from the run-vertex coordinates, its uncertainty being the size of the beam spot.

For a given event, the z-coordinate of the primary vertex is calculated first from the $z0$-coordinates of the non-vertex-fitted tracks. Then, the x-y-vertex of the event can be computed from the run-vertex parameters (which are defined at $z = 0$). All measured tracks are then matched to this vertex thus improving their resolution.

In addition to the determination of the primary vertex, the reconstruction program searches for secondary vertices by trying to match tracks to a common origin which is significantly separated from the primary vertex. As a consequence, several *fit hypotheses* for a non-vertex-fitted track may exist. The set of tracks consisting of all possible matchings to all found vertices is named *vertex-fitted tracks*. Together with the list of vertices, it is the final output of the CJC reconstruction program, and the basis for the physics analyses.

Typical values of the vertex parameter resolution are $250\,\mu$m for x and y and 2 mm in z.

The z-resolution of the CJC tracks being two orders of magnitude lower than the R-Φ-resolution is improved by merging information from the z-chambers CIZ and COZ that have a R-z-resolution of $\approx 350\,\mu$m.

2.4 The vertex detector CST

The silicon strip microvertex detector CST (Fig. 2.8) was installed completely in 1996 and began its regular data taking operation in 1997. Its purpose is the reliable separation of primary and secondary vertices in an event. This goal is achieved by improving the resolution of the track parameters measured in the central region of the H1 detector. In particular, the limitation of the primary vertex resolution introduced by the radial beam extensions is overcome making it possible to resolve decay lengths of the order of $100\,\mu$m that are typical for the decays of heavy quarks. The precision needed for this purpose can only be achieved by a high-resolution position sensitive detector as close to the interaction point as possible.

2.4.1 Detector layout

The CST consists of two layers of silicon strip detectors mounted cylindrically around the beam pipe at radii of $R = 57.5$ mm and $R = 97$ mm respectively. The detector is centered at the nominal interaction point and has an effective length of 358 mm, thus covering a large fraction of the interaction region. Its polar angle acceptance is $30° < \Theta < 150°$. A total of 81920 strips on 192 silicon sensors are read out.

The CST is made of double-sided, DC-coupled silicon detectors to allow position measurements in R-Φ as well as in z. The sensitive area of a sensor is $5.62 \times 3.2\,\text{cm}^2$, its thickness $300\,\mu$m.

On the p-side of the detectors, the strips are parallel to the z-axis thus measuring Φ. The readout strip pitch is $50\,\mu$m resulting in a total number of 640 channels. The principle of the measurement is

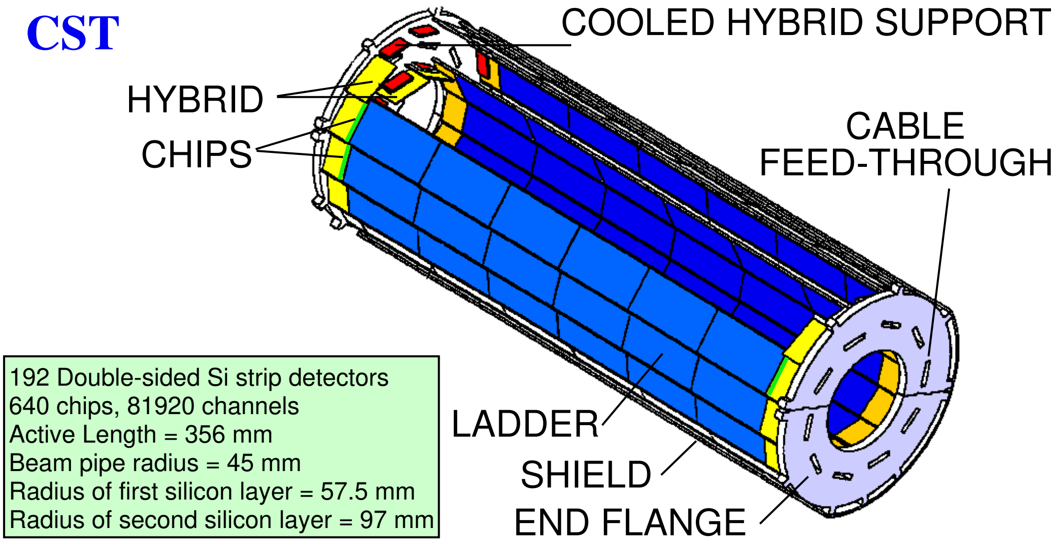

192 Double-sided Si strip detectors
640 chips, 81920 channels
Active Length = 356 mm
Beam pipe radius = 45 mm
Radius of first silicon layer = 57.5 mm
Radius of second silicon layer = 97 mm

Figure 2.8: *The microvertex detector CST*

sketched in Fig. 2.9.

Applying a voltage between p-side and n-side of the silicon sensors creates a reverse-biased p-n-junction. When the bulk is fully depleted, an ionizing particle traversing the detector creates electron-hole pairs that drift along the electric field lines towards the p^+-implant strips and to the n-side contact respectively.

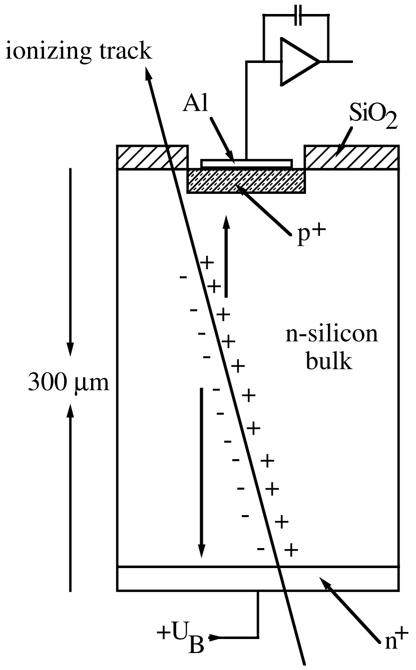

Figure 2.9: *Principle of a DC-coupled silicon detector with readout on the p-side (from [32])*

On the n-side, the strips are orthogonal with respect to z with a readout pitch of $88\,\mu$m. Segmenting the n-side however leads to a an accumulation of negative charges at the boundary between the n-silicon bulk and the covering silicon oxide[14] for a depleted detector. This is due to a positive space charge within the silicon dioxide due to trapped holes that have been created during processing. The resulting effect is a conductive layer between neighbouring strips (Fig. 2.10, a). For the CST detectors, the n-side strips are therefore separated ohmically by implanting p^+-strips between the n-strips (Fig. 2.10, b).

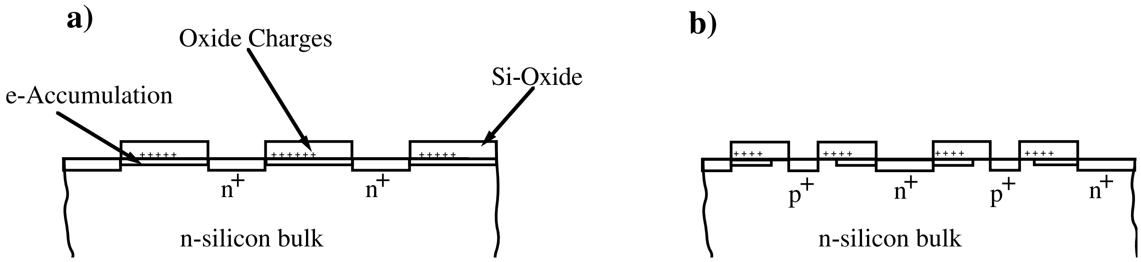

Figure 2.10: *The use of p-blocking implants for isolating n-side strips (from [32]):*
a) *n-side of a depleted silicon detector with a conductive sheet due to trapped charges between the n^+-strips;*
b) *ohmic charge separation of the strips by p^+-blocking implants as used for the CST detectors.*

Since the readout direction is fixed to be at $+z$ or $-z$, a second metal layer is necessary to route the signals to the ends of the CST. The second layer is separated from the first metal layer (the aluminum strips that are in contact with n^+-implant strips) by a silicon dioxide layer of thickness $5\,\mu$m. The double metalization however introduces a higher capacitance and therefore a higher noise level for the n-side [33].

A support structure of carbon fibre provides the necessary rigidity (a position stability of $5\,\mu$m has to be maintained) while minimizing the amount of insensitive material. Six silicon sensors together with two hybrids carrying the readout electronics (one at each end) are joined by carbon fibre rails along their sides to form a detector ladder. The two layers are shaped as regular prisms with 12 and 20 detector ladders respectively resulting in 100% geometrical acceptance in Φ with some overlap at the ladder edges. Due to the gaps between adjacent detectors, an insensitive region of about 3% in z is however unavoidable. Three detectors have their readout lines daisy-chained on both sides and make up —together with their readout hybrid— the basic entity for readout and reconstruction: the *half-ladder* (Fig. 2.11). Due to the serial connection of the readout lines of a half-ladder, a three-fold ambiguity is introduced for the n-side-signals that has to be resolved by the reconstruction process.

The detector ladders are held together by supports on the carbon-fibre end flanges that also contain water pipes for cooling. The end flanges carry printed circuit boards that distribute control signals and supply voltages to each of the hybrids, and that convert the signal charge pulses from the readout strips into optical signals for further readout.

The total weight of the CST is 1.5 kg. At $\Theta = 90°$, the total material thickness of the CST, including all supports, is $\approx 1\%$ of a radiation length.

The front-end readout chips and the subsequent electronics are described in Chap. 3.1.1.

---

[14] For passivation, the silicon sensors are covered with a silicon oxide layer of thickness $0.8\,\mu$m.

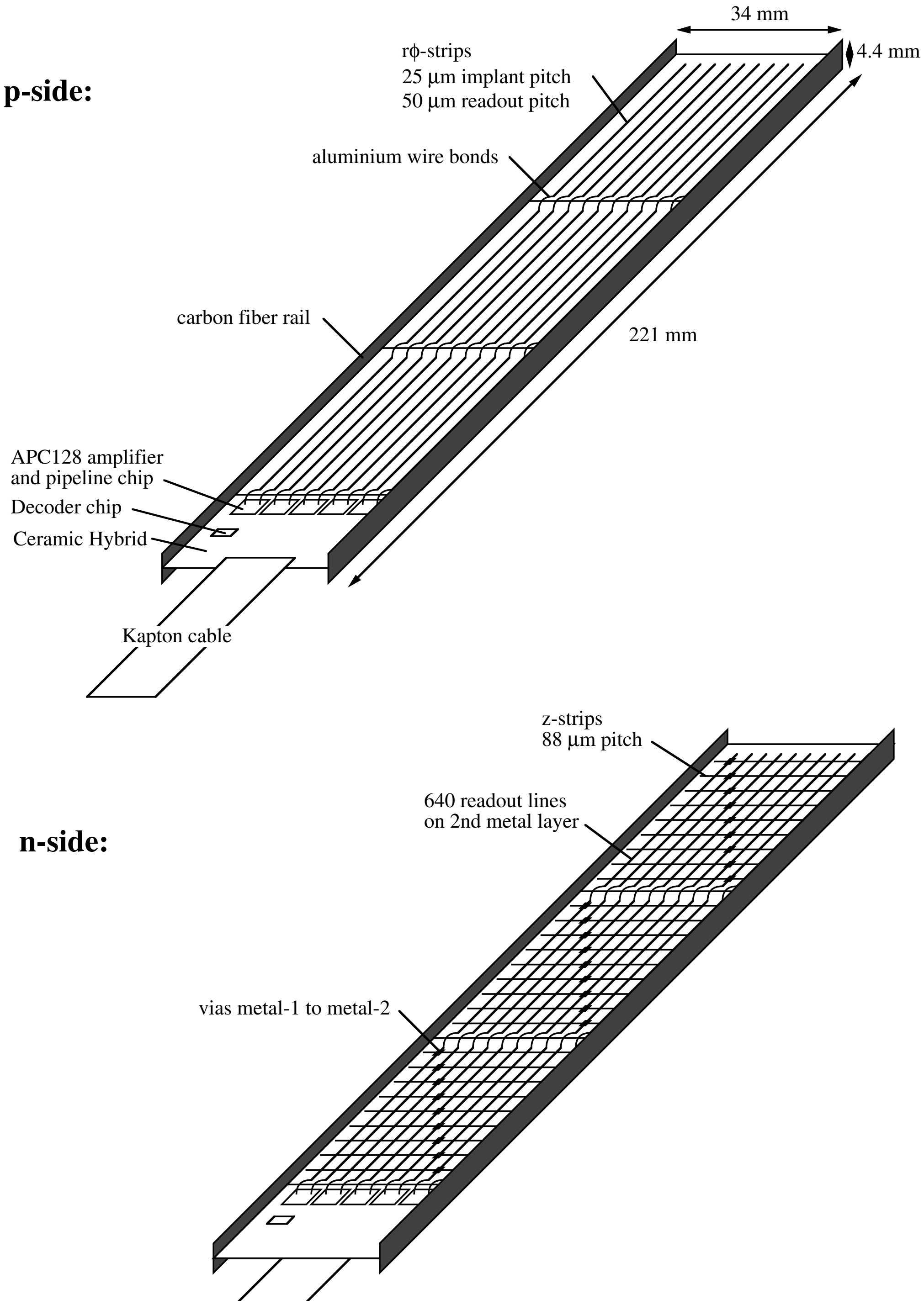

Figure 2.11: *Schematic view of the CST detector half-ladders on p- and and n-side*

2.4.2 Vertex resolution and beam pipe

Within the polar angle acceptance of the CST, a particle from an *ep*-event vertex is measured in both layers. With this position information, the particle track can be reconstructed. As will be explained in Chap. 4, it is necessary for this purpose to combine the CST measurements with measurements of the CJC. Hits from the CST are employed to improve the resolution of the tracks that have been found by the CJC. The event vertex can then be reconstructed by matching a common origin to the measured tracks.

For the following considerations about the achievable vertex resolution, the influence of the CJC measurements is neglected. This is justified since the CST measurements are the dominating contribution to the track parameters, as will be shown in Chap. 4.6.

The position resolution at the vertex is then determined by three contributions:

1. the geometrical extrapolation error when calculating the track origin on the basis of the measured hits
2. the uncertainty due to multiple scattering of a particle before it is detected
3. uncertainties on calibration and alignment of the detector

The *uncertainty on the alignment* of the silicon sensors of the CST is smaller than their intrinsic resolution and thus does not contribute significantly to the error on the vertex measurements. The alignment procedure is briefly sketched in Chap. 4.2.

For a double-layered detector like the CST the *geometrical extrapolation error* is given by

$$\sigma^2_{geom} = \left(\frac{\sigma_1 r_2}{r_2 - r_1}\right)^2 + \left(\frac{\sigma_2 r_1}{r_2 - r_1}\right)^2 \qquad (2.4)$$

where r_1, r_2 are the radial positions and σ_1, σ_2 are the intrinsic resolutions of the first and second silicon layer. It is hence desirable to have the inner detector layer as close to the interaction point as possible while maximizing the lever arm $r_2 - r_1$. At H1, the available space is limited by the beam pipe which determines the inner radius r_1 and the CIP determining the outer radius r_2 (cf. Fig. 2.3). In addition, it has to be allowed for some space for a mounting tube and for shielding to protect the front-end electronics against electromagnetic interference and to ensure a safe installation.

Exploiting the overlapping geometry of the layers, the intrinsic resolution on the p-side of the CST detectors has been measured to be $12\,\mu$m and $16\,\mu$m for inner and outer layer respectively [34]. On the n-side, the resolution is $25\,\mu$m, but has a strong dependence on the impact angle of the particle. The contribution from extrapolation uncertainties to the vertex resolution can thus be estimated (Eq. (2.4)) to be $\approx 40\,\mu$m on the p-side and $\approx 75\,\mu$m on the n-side when using CST information alone. However, when combining the precise measurements of the CST with the measurements in the CJC at comparably large radii, an improvement can be expected. At the same time it will be important not to introduce systematic uncertainties from the combination of the measurements which means that both detectors have to be calibrated and aligned correctly.

The *multiple scattering uncertainty* is given by a sum over all scattering layers traversed by a particle until reaching the outer detector layer:

$$\sigma^2_{M.S.} = \sum_i (R_i \Delta\Theta_i)^2 \qquad (2.5)$$

where the mean angular deviation $\Delta\Theta_i$ of a particle with transverse momentum p_t caused by multiple scattering in material with radiation length ΔX_i at radius R_i is [10]

$$\Delta\Theta_i \approx \frac{0.0136}{p_t\,[\mathrm{GeV}/c]}\sqrt{\frac{\Delta X_i}{X_0}}\left(1+\frac{\log\frac{\Delta X_i}{X_0}}{26}\right) \tag{2.6}$$

At colliding beam experiments like H1, a major contribution to multiple scattering is due to the beam pipe. In 1997, an aluminum pipe of radius 45 mm was installed which had a thickness of 2% of a radiation length X_0. During the 1997/98 shutdown, a new carbon-fibre pipe of the same radius of 45 mm and a thickness of 1% X_0 was inserted. Fig. 2.12 shows the contribution from multiple scattering in the beam pipe to the vertex resolution as a function of the transverse momentum p_t. It becomes clear that multiple scattering is the dominating contribution to the vertex uncertainty up to p_t-values of several GeV, especially when considering that a particle undergoes further multiple scattering in the CST itself. The precision of the vertex determination therefore depends crucially on the presence of high-energetic tracks. However, typical particle momenta in the decay processes involving heavy quarks are of the order of 1 GeV, so that it can be expected that the multiple scattering will remain a limiting factor for the vertex measurements.

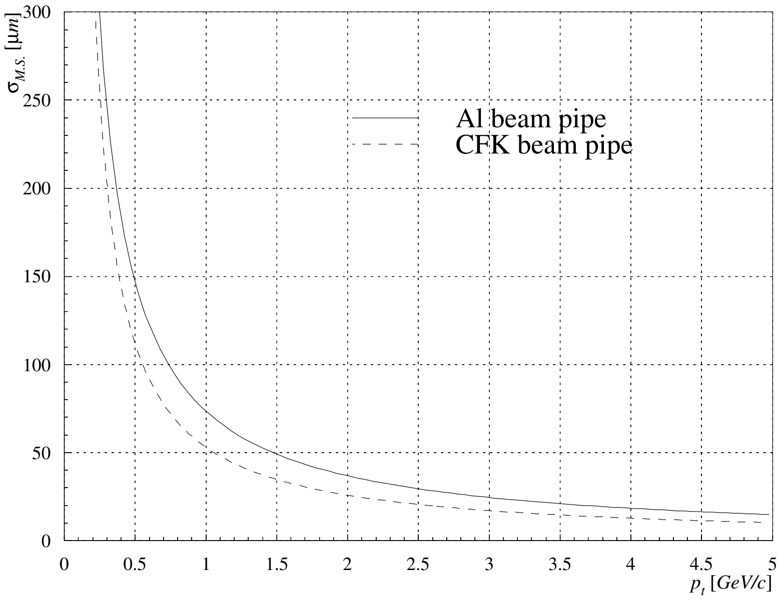

Figure 2.12: *Vertex resolution as function of transverse momentum. Only the contribution from multiple scattering in the beam pipe is plotted.*

The following chapters describe the data acquisition system for the CST and the methods applied in the reconstruction of events measured.

Chapter 3

Readout and control of the H1 silicon trackers

In 1997, the system for reading out and controlling the two silicon strip detectors CST and BST was fully commissioned and operated for the first time. The CST was completely equipped (81920 readout strips) while four disks of the BST with 40960 readout channels were installed. In this chapter, the **data acquisition** system, **the slow control** and the **online monitoring system** will be described. A focus will be put on the routines that have been developed and implemented for an **online hit finding**. The components of the whole system are sketched in App. A.1.

3.1 Data Acquisition

The parameters of the silicon strip detectors and the environment in which they are operated impose several constraints and challenges on the readout system:

1. The large number of readout strips leads to the need of a highly integrated front-end system where the signals are multiplexed at an early stage.
2. The low signal amplitude of silicon strip detectors makes the use of preamplifiers close to the sensors inevitable. The limited space in the center of the H1 detector however only allows the use of a very compact system with minimal power dissipation.
3. The HERA bunch repetition rate of 10.4 MHz and the decision time of the central trigger (first-level trigger: 2.4 μs) make it necessary to store the signals recorded in an event until a trigger decision is made.
4. The readout of the front-end system has to be fast enough to avoid any additional contribution to first-order dead time[1]. At H1, the time foreseen for the front-end readout is 800 μs.
5. An event size reduction on the raw data of the silicon detectors before they are merged into the central data stream of the H1 experiment is necessary. As described in Chap. 2.2, full events are assembled over fibre-optic links after a positive decision of the L2/L3 trigger stage (at rates of up to 100 Hz) and, if they have been accepted by the L4 filter farm process, are written to

---

[1] This is the time span during which the detectors are being read out and hence are insensitive.

tape at a rate of ≈ 5 Hz. The raw data size of the silicon readout branch alone is 250 kBytes per event. Since this is too much for storage (a complete H1 event written to tape has a size of ≈ 40 kBytes) and would also consume a bandwidth of ≈ 25 MBytes/s, a hit- & cluster search on the silicon raw data has to be performed. Due to the various effects influencing the signal of silicon detectors and, again, due to the large number of channels, powerful processors are needed.

6. The processing stage after the front-end data have been read out has to be decoupled completely from the front-end operation. This means that after one event has been read out from the front-end, the system has to be able to accept the next one immediately. Dead time introduced by subsequent processes like the hit detection or the data formatting is referred to as second-order dead time. In order to avoid second-order dead time, multi-event buffering has to be provided on the stage of the online hit detection.

7. The whole system has to be flexible enough to be able to read out different types of strip detectors: in particular different algorithms for the hit detection have to be implemented.

8. In order to cope with future expansions, namely additional disks of the BST and the silicon tracker of the VLQ, the system should be easily extendable.

The solution for the silicon detectors of H1 [35] meets the requirements 1.-4. by using a custom-built readout chip (APC128) mounted next to the silicon sensors. It is portrayed in Chap. 3.1.1. The conditions 5.-7. are met by using VMEbus based microcomputers with PowerPC processors. They are described in Chap. 3.1.2 with focus on the algorithms used for the online hit detection. Backbone of the system is a fibre-optic ring connecting all processors in the Silicon branch employing the VMEtaxi protocol [36]. It is controlled by a master processor supervising the readout and connecting the branch to the main H1 data acquisition system.

3.1.1 Front-end electronics

The front-end system of the H1 silicon strip detectors has a hierarchical structure: As described in Chap. 2.4, the basic building block of the CST is the detector half-ladder with 640 readout strips on both the p- and the n-side of the silicon sensors. At the end of each half-ladder, a hybrid is mounted that carries 5 readout chips [37] and one decoder chip on each side. The decoder chips are needed to control the operation of the readout chips. They are steered by the custom-designed VMEbus controller module OnSiRoC[2] [38, 39].

For the readout of all 81920 CST strips, 640 readout chips that are controlled by 128 decoder chips are needed.

The **readout chip** APC128[3] (Fig. 3.1) contains 128 readout channels each consisting of a charge-sensitive preamplifier and an analog signal pipeline buffer with 32 cells. It is operated by a digital shift register at the HERA bunch crossing frequency of 10.4 MHz. Incoming signals from the detector are amplified and then stored on the capacitors C_p of the pipeline buffer. Following a trigger signal, the stored charge is again amplified by the same preamplifier and then transferred to the latch capacitors C_L. The rise-time of the preamplifier signal is ≈ 80 ns [40]. Using the same preamplifier

---

[2] **O**nline **S**ilicon **R**eadout **C**ontroller

[3] **A**nalog **P**ipeline **C**hip with **128** channels

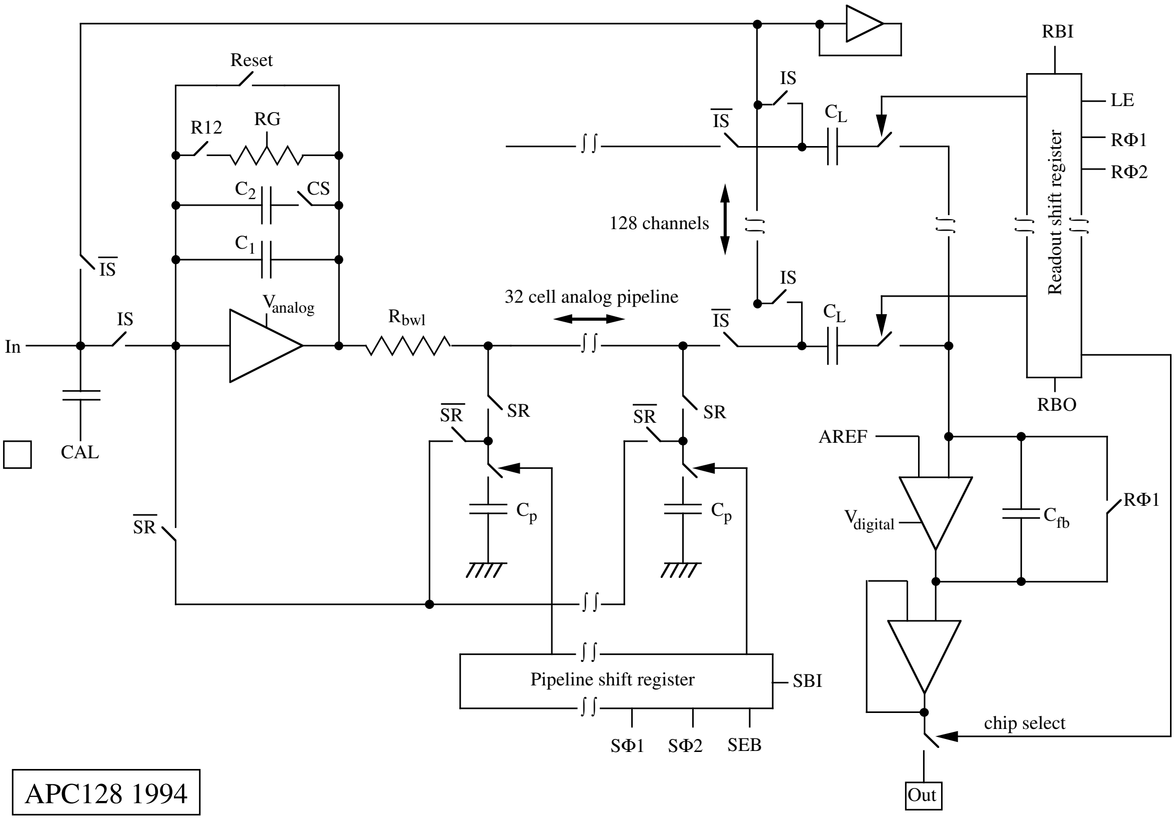

Figure 3.1: *Circuit diagram of one channel of the APC128*

has the advantage of reduced power consumption. The subsequent serial readout from the latch capacitors is controlled by the readout shift register: the capacitors are connected to the output amplifier successively. The rise time of the output pulses is ≈ 200 ns for CST signals, so that a readout frequency of 2 MHz is achieved [41]. Additional features of the chip include the possibility of a primary background rejection by adding or subtracting analog signals from arbitrary pipeline cells on the latch capacitors. Since the output stage of one APC may be set to a high-impedance state it is possible to read out several APCs using the same analog line.

The chip is fabricated in a 1μ-SACMOS[4] process. Each readout channel has a width of 44μm and the depth of a pipeline cell is 50μm. Together with the space for amplifiers and bond pads the area of the APC is $3.5 \times 6.3\text{mm}^2$.

The **decoder chip** is needed to (de)multiplex control signals for the APCs. Its task is to control the 14 switches of the APC with the input of only 4 signals generated by the OnSiRoC thus minimizing the number of lines between the control module and the front-end system. Furthermore, it can generate calibration pulses for the APC and monitor voltages for testing the readout line. It also contains the current source for the APC-preamplifiers. Up to 5 APCs are controlled by one decoder chip on a common hybrid.

The function of the **control module** OnSiRoC in the readout system is twofold: it is responsible for

---

[4] **S**elf-**A**ligned **C**omplementary **M**etal **O**xide **S**ilicon. 1μ means that the smallest structures on the chip have a size of $1\,\mu$m. The smaller the structures the greater is the radiation hardness of the chip.

the operation of the front-end chips and it serves as power supply for the chips as well as for the silicon sensors[5]. Its main components are therefore:

- a programmable sequencer that controls the operation of the OnSiRoC itself and generates the signals for the front-end chips
- 4 independent sets of 3 voltage supplies: analog (V_{analog}) and digital ($V_{digital}$) voltages for the APCs and decoder chips and the depletion voltage (V_{bias}) for the silicon sensors. All voltages can be switched independently. In addition, the bias current can be digitized and read out.

A sequencer is a programmable processor consisting of memory units and transceivers with registers. Programs for different operation modes can be stored and executed. A sequence consists of 32 bits: 16 data bits and 16 address bits. The latter are used for identifying the next sequence. It is possible to program infinite loops that can be interrupted by external trigger signals. For creating a binary file with sequencer instructions a programming language and a compiler for Macintosh computers have been developed [42].

The OnSiRoC is operated in two standard modes: *data sampling* (where detector signals are stored in the pipeline cells of the APC) and *data readout* from a specified cell. The sequencer programs for these two modes reside at defined addresses in memory. Communication with the H1 trigger system that initiates the switching between the two modes is established via a modified VME backplane.

For data sampling the OnSiRoC resets its internal pipeline counter and starts the sequencer that in turn initializes the APCs and initiates the operation of the pipeline in a never-ending loop. If a trigger signal is received, the sequencer starts from the address where the corresponding code is stored. The pipeline is stopped, and the charge in the pipeline cell storing the triggered event is transferred to the latch capacitors[6]. Readout is started by activating the readout shift register and the output amplifier.

Within the Silicon readout branch the front-end system operates autonomously in the sense that it is controlled entirely by the global H1 trigger signals and the HERA clock and hence works independently of the further steps (digitization and hit finding).

While the front-end chips and their controlling are identical for CST and BST, the systems used for the subsequent **transmission of the raw data** from the detectors to the back-end electronics are different: The CST converts the multiplexed analog signals to optical pulses on the printed circuit boards on the endring flanges of the detector [41]. A total of 16 fibre-optic links then transfers the data to the back-end electronics. Here, the signals are converted back into charge pulses by custom-built modules and passed on to the readout processors.
The BST uses repeater electronics mounted behind the detector disks. The signals from the hybrids are received via kapton cables. Line drivers provide the ability to send the analog signals via $\approx 40\,\mathrm{m}$ of coaxial cable.

3.1.2 Processor modules

The processor modules are industrial-made RIO2 8060 boards from CES [43]. Their main components are:

---

[5] Originally, it was intended to use the OnSiRoC also for readout, digitization and further signal processing [39, 40]. Due to the complexity of this task which had not been anticipated, it was in this respect replaced by the new readout modules RIO2 (s. Chap. 3.1.2).

[6] At this stage, background is suppressed by subtracting charge of empty cells before the "event cell" from the signal charge.

- a 100 MHz PowerPC-604 processor with on-chip 16 kBytes data and instruction cache respectively
- 8 Mbytes of on-board DRAM memory
- PCI[7] standard backbone bus (bandwidth 128 Mbytes/s)
- IBM Lanai/Kauai Bridge chipset for interfacing the CPU subsystem to the memory
- VME D64 Master/Slave interface
- two custom-designed mezzanine cards carrying four Comlinear CLC949 Flash ADCs each

Each of the eight FADCs digitizes the raw data of 1280 readout strips, so that one RIO2 module processes the data of 10240 readout strips. In case of the CST, the signals are routed in a way that one FADC receives data from the p-side of a detector ladder, i.e. of two adjacent half-ladders (one read out at the $-z$-side, the other at $+z$, cf. Chap. 2.4), while the next FADC processes the corresponding n-side data.

In total, 8 modules for the CST and 4 for the BST placed into a common crate are used[8]. Apart from the digitization, the modules perform the online processing (i.e. the hit finding) of the raw data.

The connections between the front-end chip APC, the readout module RIO2, and the control module OnSiRoC are sketched in Fig. 3.2.

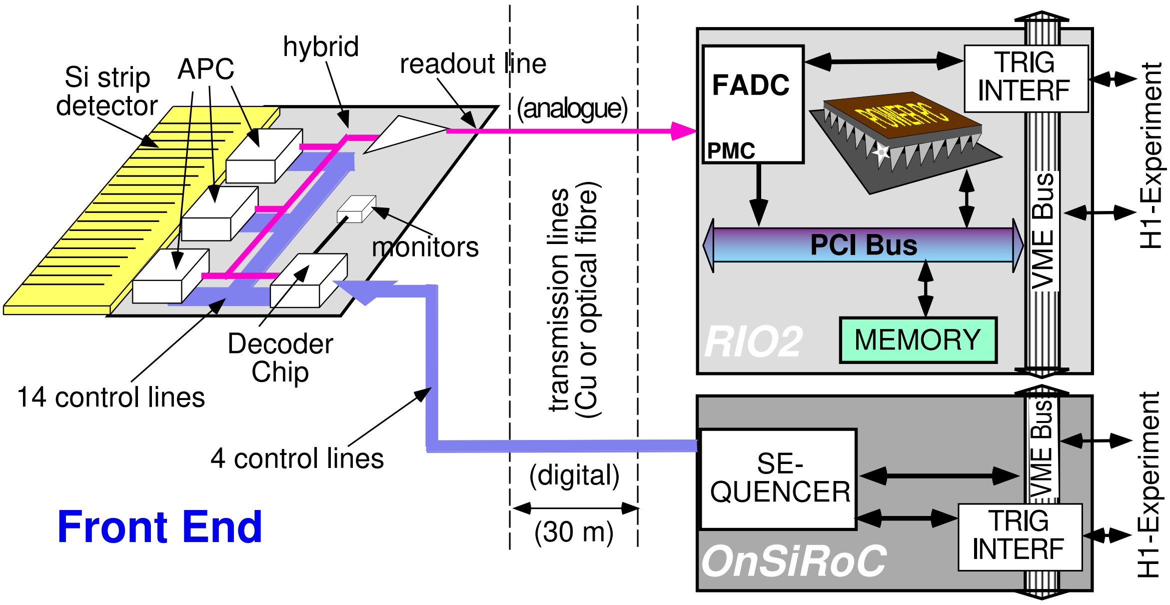

Figure 3.2: *Connections between front-end system and readout- and control modules*

---

[7] **P**eripheral **C**omponents **I**nterconnect, a bus system that has become an industrial standard in microcomputers

[8] Future expansions will establish a second RIO2 crate. CST and BST will then use different crates and one of them will host two additional RIO2 modules for the tracking detector of the new Very Low Q^2 spectrometer (VLQ).

Digitization stage

The readout modules are equipped with two custom-built PCI mezzanine cards (PMCs) that carry 4 Flash ADCs each [44]. On these cards the digitization process of the analog data from the front-end takes place. It is controlled by a programmable hardware logic (XiLinX 4006E) making use of the H1 trigger signals and of a signal from the OnSiRoC that synchronizes the front-end readout process described in the previous section and the digitization process. Since the front-end system operates independently of the RIO2 modules, the hardware logic has to determine by itself which of the analog pipeline cells is read out. A distinction of the cells is necessary since each cell is characterized by specific properties of the analog signal (pedestal, noise level, s. Chap. 3.2.2). For this purpose the number of HERA clock signals between the trigger signals is counted on the PMC[9].

After digitization the data together with the value of the pipeline counter are transferred to the system memory via the PCI bus. Both the OnSiRoC driving the front-end readout and the RIO2 modules performing the digitization have to signal the completion of their tasks back to the trigger system. Up to this stage, the data transfer is synchronous to the H1 trigger signals.

The effective decoupling of the readout and digitization step from the further stages is achieved by a partitioning of the system memory into 16 buffers for the raw data. This multi-event buffering allows the subsequent online data processing to run asynchronously to the H1 trigger signals.

In 1997, the time needed for the complete analog readout and digitization of the 122880 readout channels of CST and BST was 1.05 ms. This is slightly above the original limit of 800μs (cf. Chap. 2.2) but still below the value of the slowest readout branch and hence introduces no additional first-order dead time.

Online processing

Once the digitized raw data have been transferred to one of the 16 buffers of the RIO2 memory the PowerPC processor performs the hit detection and writes the reduced data to a designated memory area, from where they are collected by the master VMEtaxi processor via the fibre optic link and the VMEbus.

While the front-end readout process and the digitization are controlled by the H1 trigger signals, the program running on the PowerPC processor of the readout module is steered by the main H1 data acquisition process. This means that the run conditions (start, stop) and specific run parameters are set centrally and transmitted to the RIO2 modules. Consequently, the software on the latter is split into two levels:

Level 1: The main readout routine [45].
It has to initialize the module on startup, establish communication with the master VMEtaxi processor (and hence find out about run conditions), and to invoke the hit detection routines. Moreover, it is responsible for the memory buffer management, i.e. bookkeeping on free and occupied raw data buffers. This level thus controls the data flow while it does not manipulate the data themselves.

Level 2: The subdetector specific hit detection algorithms.
Different routines are employed for CST and BST on this level. The algorithms for the

---

[9] The number of the cell that contains the event from a specified bunch crossing is the number of clock signals modulo 32.

> CST as well as their implementation will be described in Chap. 3.2. In addition to the actual hit finding, the tasks comprise the determination and the dynamic updating of *readout constants*, namely pedestals and values for the noise of each readout channel. The level is thus responsible for the *contents* of the data stream.

A key idea of the implementation of the tasks is the independence of the two levels. The first one —a dedicated, well-defined task which will remain stable over the entire lifetime of the system— is programmed in Assembler and is executed automatically on start-up of the system.

The subdetector-specific level 2 has to provide the desired flexibility not only in terms of different algorithms for CST or BST, but also for different readout conditions (s. Chap. 3.1.3). In order to ease maintenance, it is programmed in C and compiled separately from the main task using an optimizing compiler for PowerPCs [46]. The resulting object module is loaded to the system memory where its routines are ready to be executed.

During run time communication between the two levels is established via input and returning arguments. The main readout routine calls the subdetector-specific level whose job is then to read data from the specified raw data buffer, find the hits and write them, correctly formatted, to the corresponding hit data buffer. If the hit finding routine ends successfully, the data are picked up by the VMEtaxi. The data flow is sketched in Fig. 3.3.

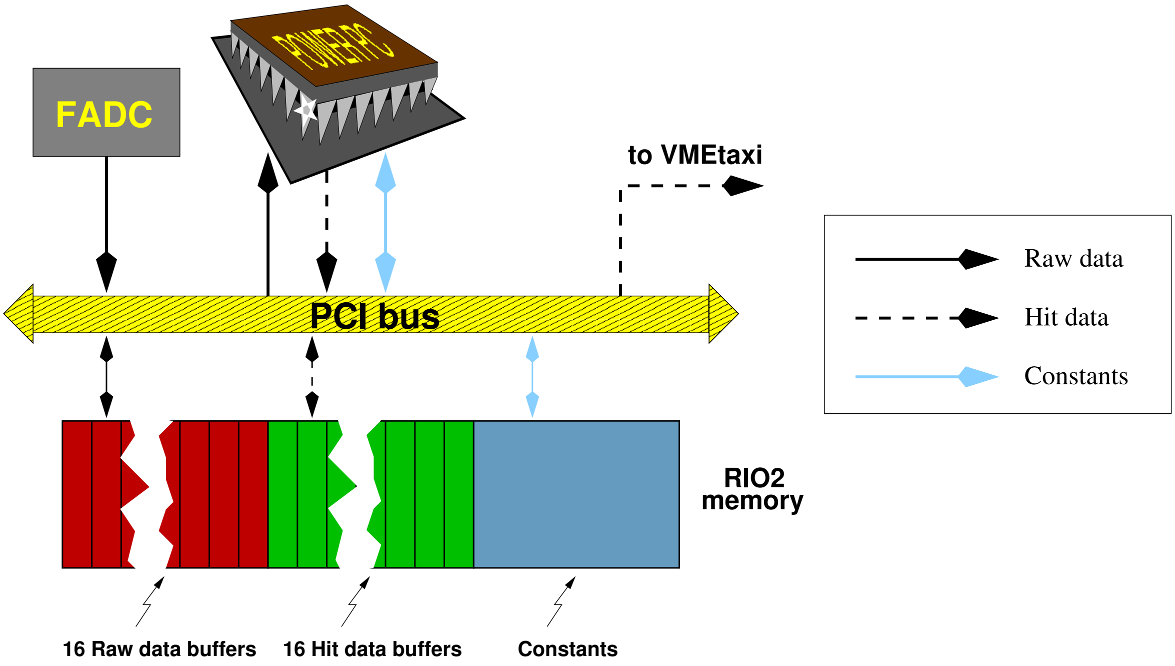

Figure 3.3: *Data flow on the RIO2 modules*

The system memory of the RIO2 readout modules is the central instance that connects the three parts of the system that are involved in the data flow:

1. the delivery of raw data from the FADCs as described in the previous section,
2. the processing of the raw data by the PowerPC itself,
3. the reading of the hit data by the master VMEtaxi processor.

In addition to storing raw and hit data the memory also has to provide space for the readout constants. Thirdly, the memory has a reserved area for communication between the three tasks, where run-specific system parameters are kept and the status of the data buffers is indicated. A complete memory map for the RIO2 system memory is shown in App. A.2.

It is clear that communication between the different processes and software layers is a key issue for a smooth operation of the system as a whole. The communication protocol on the readout modules of the silicon trackers adopts a concept used throughout the data acquisition system of the H1 detector: the memory-mapped mailboxes. Dedicated memory areas, the mailboxes, that are "visible" for all processors over the VMEbus, can be used to issue commands together with their arguments. The addressed processor in turn reacts to the command. An example is a "run start" command that is issued by the master VMEtaxi processor and causes the main readout routine on the RIO2 modules to check for raw data and eventually call the hit finding routine.

This concept dispenses with the need for an operating system on the RIO2 modules which would introduce additional complexity to the software.

The two major concerns about the software for event analysis (i.e. hit finding) at such an early stage and in real-time are execution speed and reliability. For the first point, it is mandatory that contributions to dead-time are avoided. If the online processing takes longer than the average time between the acceptance of events by the L2/L3 trigger, all 16 raw data buffers will be occupied soon so that no new event can be accepted. This sets an upper limit of 10 ms for the processing time if event rates of 100 Hz shall be tolerated. Reliability on the other hand is required since data that are rejected by the online analysis can never be recovered again.

For optimizing the program performance in terms of speed, all algorithms have been implemented in integer arithmetics which is in general faster than floating-point calculations as shown in Tab. 3.1. Time consuming operations like divisions have been replaced already in the code by bit shift operations wherever possible. The code also refrains from the use of mathematical library functions like `sqrt`.

instruction	# of clock cycles
integer add	1
integer multiply	3
integer division	20
integer load	2
floating-point multiply-add	3
floating-point divide	31
floating-point load-store	3

Table 3.1: *Instruction timing on the PPC604 processor (from [47])*

Execution speed is also limited by the time needed for memory access. This is partly due to the fact that the PCI bus is not only used by the processor for accessing the memory but also by the XiLinX task transferring raw data from the FADCs as well as by the master VMEtaxi processor requesting output data. The processor performance can thus be degraded if the bus is busy when the processor tries to access the memory. Since the PowerPC 604 processor on the RIO2 module is equipped with only 16 kBytes of data cache it cannot keep all the quantities needed for the analysis of an event in the cache. As will be described in Chap. 3.2, these quantities are the raw data and the readout constants.

It has therefore been tried to organize the readout constants in memory in a way that the number of memory accesses is minimized.

Data taking in 1997 has proven that with the present speed of the online routines and the 16-fold buffering the design event rates of ≈100 Hz can be taken.

The reliability of the implemented algorithms proved to be stable over the whole 1997 data taking period. This means that in particular, the values for the readout constants are determined and updated correctly, and the cuts for the rejection of noise are chosen in a sensible way, so that the balance between reducing the bandwidth on the one hand and collecting all signal hits on the other is kept at all times. The readout constants are introduced in Chap. 3.2.2, while the effect of the noise cuts will be discussed in connection with the offline reconstruction algorithms in Chap. 4.3.

3.1.3 Readout options

The operation of the processors of the readout system can be influenced in three ways:

1. different *readout modes* can be selected
2. a set of global *readout parameters* can be changed
3. different *readout masks* allow the (de)selection of single processor modules as well as of whole readout crates

These options are used for steering the code running on the processors. They all can be set through the main H1 data taking control application (“System Supervisor”) [48, 49]. On run-start, the master VMEtaxi processor of the Silicon branch passes the options to all readout modules.

During the 1997 data taking, the following readout modes were defined:

- Hits & Cluster (Data Type 0)
  This is the default mode, where the RIO2 module performs a hit- & cluster search, and writes data formatted as described in Chap. 3.1.4 to the hit buffers.
- Copy Raw (Data Type 1)
  This mode reformats the raw data as delivered from the FADCs and writes them to the hit buffers. It generates 20 kBytes of output per RIO2 module[10].
- Raw Data (Data Type 2)
  This mode bypasses the subdetector-specific level in the readout task. Raw data are copied to the raw data buffers and read again by the VMEtaxi. The output is hence an unformatted event block with a size of 32 kBytes per RIO2 module[11].
- Monitor (Data Type 3)
  A special mode for debugging that writes effectively all data being used when processing an event to the hit buffers, namely:
  - default hit- & cluster data

---

[10] One 16-bit word per readout strip: 2 bytes × 10240

[11] For historic reasons, 2048 16-bit words per FADC are copied (although only 1280 words have been digitized). The size is hence 2 bytes × 2048 × 8 FADCs.

  - the original raw data
  - the pedestals
  - the values for the noise
  - the values of the common mode (cf. Chap. 3.2.1)

- Extra (Data Type 4)
  This mode is foreseen for alternative or refined hit detection algorithms.

Some of these modes (Copy Raw, Monitor) are only intended to be used in conjunction with setting readout masks due to the event size they produce[12]. Their purpose is to give the possibility to investigate closer the operation of one particular readout module.

The global readout parameters contain (among others) thresholds for tuning the hit- & cluster algorithms and additional masks for selecting data from single FADCs on a RIO2 module to be treated specially. They are listed in detail in App. A.3.

3.1.4 Data formats

The data block that the Silicon readout branch assembles in every event is already formatted in a manner that it can be further processed offline with the standard H1 reconstruction software and its data-handling tools. The basic unit is a 32-bit word while blocks of words are structured as *banks*, memory blocks that can be identified unequivocally by their header words containing a name and the length. Such a named bank may also have a format, e.g. may be organized in (virtual) rows and columns with predefined meanings. The final assembly of a silicon data block is done by the master VMEtaxi processor. For this purpose it collects data from the output buffers of all RIO2 readout modules. The resulting bank is called SIFE[13]. In addition, banks that are produced by the BST pad trigger system are appended. Finally, a header bank (SDAQ) is created at the beginning of the event block indicating that data from the silicon branch are present. At the beginning of a run, the global readout parameter block `SiDAQSpec` described in App. A.3 is put into a bank called SIRS[14]. The format of all these banks is shown in App. A.4.

This section describes the formatting of the data for one RIO2 unit. Since the output of all readout modules is just appended, a "substructure" within the SIFE bank is needed to be able to distinguish between data from different modules. For this reason *header words* are introduced that mark a block of data within the SIFE bank and contain also its length.

Raw data The digitized data from the 8 FADCs are first written to the raw data buffers of the readout modules. Their order is the following:

---

[12] Note that the raw data size of a complete "normal" H1 event is of the order of $\approx$40 kBytes.

[13] **S**ilicon **F**ront **E**nd data

[14] **S**ilicon **R**un **S**tart record

`$0000:`	FADC 0 - strip 0	FADC 1 - strip 0
`$0004:`	FADC 2 - strip 0	FADC 3 - strip 0
`$0008:`	FADC 4 - strip 0	FADC 5 - strip 0
`$000C:`	FADC 6 - strip 0	FADC 7 - strip 0
`$0010:`	FADC 0 - strip 1	FADC 1 - strip 1
	⋮	⋮

i.e. for every strip number there is a block of eight 16-bit words for all connected FADCs. Due to the FADC resolution (12 bit + overflow) only 13 bits per word are used, so that the format of an individual 32-bit raw data word is:

```
000DDDDD'DDDDDDDD'000DDDDD'DDDDDDDD
```

In case of Raw Data readout (s. Chap. 3.1.3), the contents of the raw data buffers are copied to the central data acquisition system without any further processing. For each of the eight FADCs, 2048 16-bit data words are copied, which amounts to 32 kBytes per RIO2 module. The SIFE bank is then created by just appending these raw data blocks. No additional header words are inserted. For the analysis one therefore needs to know the mask of selected readout modules which is contained in the SIRS bank (s. App. A.4).

Formatted data In all other readout modes however, additional formatting by the PowerPC is performed. Before writing the data themselves, a block of ten header words is written first, the first one having the following format:

```
PPC Data Header Word

        BBxxxxxx'xxxxxxxx'xxllllll'llllllll

B:      2-bit subdetector: 00-CST; 01-BST; 10-VLQ
x:      subdetector specific (containing the RIO2 no. somewhere)
l:      14-bit length of PPC data block (in long words)
-------------------------------------
```

Offline, formatted data from one specific readout module within the SIFE bank can then be identified by their “subdetector”-bits, RIO2 number, and the length. The rest of the header words contains information on the operation of the program on the readout module:

- values from the PowerPC’s timing register that tell how fast a subroutine is being executed
- “Code version” labels
- the internal pipeline counter of the module
- the address of the raw data buffer used in this event
- a status mask of all raw data buffers that indicates the “load” of the module, i.e. how many events are still to be processed
- information on the status of the constants updating processes

These words allow online monitoring of the performance of the readout modules (s. Chap. 3.4).

After the header words follows the data block written by the PowerPC. It is again substructured with respect to the FADCs: data from one FADC are written sequentially (unlike the raw data format (s. above)). Each of these FADC data blocks again begins with a header word containing the length and the FADC number. The resulting overall structure of the data produced by the Silicon branch of H1 is illustrated in Fig. 3.4. The content of the FADC data blocks depends on the selected readout mode and is also coded into the FADC control word. Table 3.2 shows the most important types of data blocks for one FADC that the RIO2 modules write.

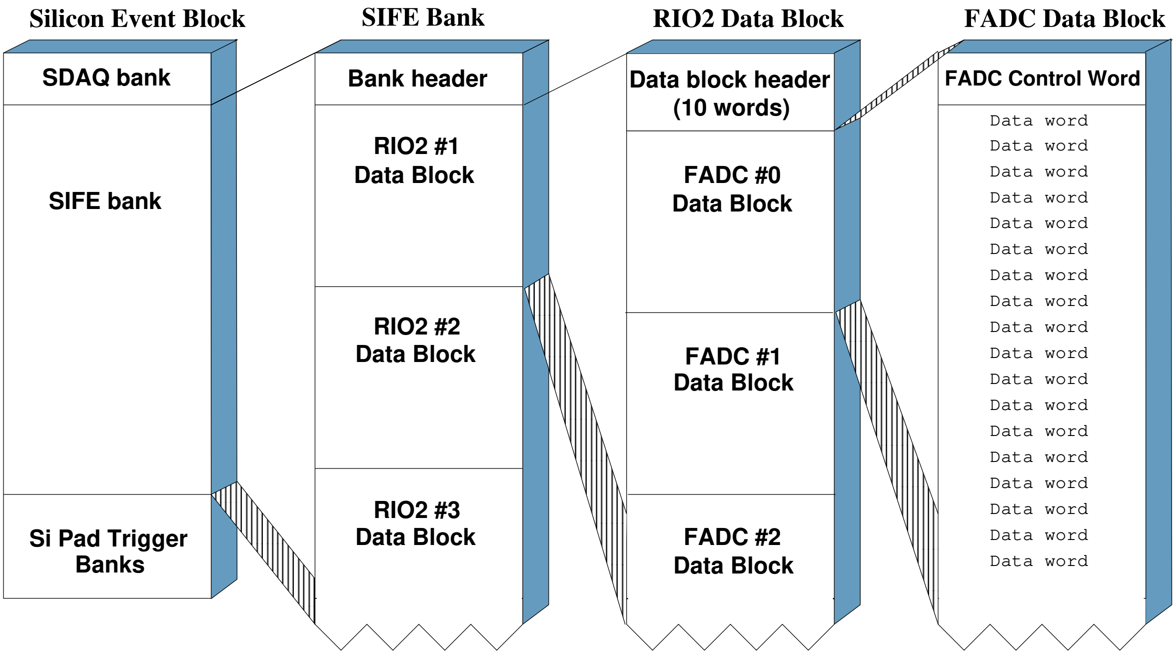

Figure 3.4: *Structure of a Silicon event data block*

Data Type	Content	Length	Readout mode(s)
Hit	one 32-bit word per strip belonging to a cluster	variable	Hit&Cluster, Monitor, Extra
Raw	**formatted** raw data: 16-bit words consecutively for each FADC	740 (CST), 640 (BST)	CopyRaw,Monitor
Ped	Pedestals (32-bit words)	1280	Monitor
Sig	Noise values (32-bit words)	1280	Monitor

Table 3.2: *The most important FADC data blocks*

However, most of these possible data types are provided for code development and debugging purposes only since their size is far too big. The default case is that the readout modules only write blocks with hit-&cluster data.

3.2 Online algorithms for the CST

This section describes the algorithms developed for online processing of the CST data and their implementation. As motivated in Chap. 3.1.2, the readout modules have to perform a cluster search in every event. Furthermore, they have to secure that correct readout constants, namely pedestals and noise variances are used. After a system-reset an initialization of the constants is therefore performed first whereas during running, the constants are updated dynamically. A general principle of all routines is that data are processed FADC-wise. In the case of the CST, one FADC digitizes the data of either p- or n-side of one detector ladder, i.e. two times 640 strip signals read out at the +z- and at the –z-side respectively.

3.2.1 Hit finding

The expected average occupancy of the microvertex detector is of the order of a few pars pro mille[15]. The actual number of words written depends on several sources:

- the track density in the detectors
- the cluster width of a hit, i.e. the spread of the charge drifting in the silicon
- the noise level
- the strictness of the cuts used in the cluster algorithms

The digitized raw data signal amplitude RAW_i for every readout strip consists of several contributions:

$$RAW_i = PH_i + PED_i + Noise_i + CM \tag{3.1}$$

where PH_i is the actual signal pulse-height, PED_i is the pedestal, $Noise_i$ the contribution from electronic noise, and CM the so-called common mode (s. below). The origin and the treatment of pedestal and noise will be described in the next section. The common mode contribution stems from a shift of the common baseline of the signals of one detector between single events. This effect is due to short-term fluctuations of the bias voltage of a silicon sensor and of the supply voltage of the preamplifiers. Thus, in order to extract the correct signal pulse-height, the magnitude of the common mode has to be determined for every event as a common quantity for groups of readout strips. Pedestals and noise on the other hand are specific quantities for every readout channel, but their fluctuations are slower, so that their calculation can make use of the raw data information of many events.

The hit finding for the CST is performed only if the pedestals PED_i and the variances VAR_i (the quantity describing the noise fraction of the raw data amplitude) have been initialized correctly for all readout strips i. (cf. Chap. 3.2.2). It consists of a two-pass algorithm processing the raw data RAW_i of every strip. The main loop runs over one half-ladder, i.e. 640 strips.

In every event the first pass over the data is used to evaluate the magnitude of the common mode for every APC (128 strips). It is calculated as the mean raw data value from all strips (denoted CM_{128}). To exclude large contributions from “hit strips”, the pulse-height PH_i for every strip is then evaluated as

$$PH_i \; = RAW_i \; - \; CM_{128} \; - \; PED_i \tag{3.2}$$

---

[15] A rough estimation gives 20 central tracks × 2 CST layers × 2 detector sides × 3 strips per cluster = 240 hit strips of a total of 81920 ⇒ 3 ‰.

and a 3σ-cut (where $\sigma = \sqrt{VAR_i}$) is applied as a robust estimator of the strip having been hit. Next, the common mode is evaluated again from the remaining “non-hit-strips”. The first pass hence actually contains two loops over the data. In case the number of “non-hit strips” is below 64, the CM_{128} is used.

In a second pass the pulse-height is evaluated this time using the common mode CM that is unbiased by contributions from hit strips:

$$PH_i = RAW_i - CM - PED_i \tag{3.3}$$

A pulse-height has to meet two criteria for the strip to be marked as a hit candidate:

$$\begin{aligned} PH_i &< 0 \\ PH_i^2 &> VAR_i \times CSTStripCut \end{aligned} \tag{3.4}$$

The first condition is due to the polarity of the analog signals. For the second one, the value of *CSTStripCut* can be selected as a run parameter (cf. Chap. 3.1.3). In 1997, it was set to 1.

An unused bit of the raw data word of a hit strip is used as a flag to be checked by the updating routine, cf. Chap. 3.2.2. As long as the above conditions (3.4) are true for neighbouring strips, the pulse-heights as well as the variances are summed up and stored. If the first non-hit strip is reached, the *Cluster Criterion* for the candidate strips is checked:

$$\left(\sum_{n=1}^{cw} PH_n\right)^2 \times cw \quad > \quad \left(\sum_{n=1}^{cw} VAR_n\right) \times CSTClusterCut \tag{3.5}$$

where cw is the number of strips belonging to the cluster candidate. For the *CSTClusterCut* a value of 16 was used in 1997. It can also be changed externally.

If statement (3.5) is true, a hit word containing the strip number i, the pulse-height PH_i, and the noise sigma ($= \sqrt{VAR_i}$) in a bit-compressed form is written to the output buffer for each strip (App. A.5). This allows to repeat the cluster search in the offline reconstruction process (s. Chap. 4.3).

The reason for using quadratic expressions, namely squared pulse-heights and variances, in Eq. (3.4) and (3.5) are considerations about computing time. Employing linear expressions (using the standard deviation σ_i as a threshold) would involve the use of a square root to obtain σ_i. For the processor, it is faster to use the squared quantity variance and take the square of the pulse-height.

The time needed for the hit finding for the 10240 readout strips connected to one RIO2 readout board is on average 5.8 ms (cf. Chap. 3.4.2).

With the default settings in 1997, the average event size of the silicon readout branch alone was ≈ 6 kBytes. This corresponds to an event size reduction factor of 60 compared to the raw data.

Handling monitor signals In addition to the strip data, CST events contain 8 monitoring signals for each FADC that are generated on the hybrid (commonly known as “Specials”). These signals allow an easy supervision of the readout chain and are especially useful for determining whether the detector and chip voltages are switched on. Since one of the signals is the voltage across an NTC[16]-resistor, the temperature on the hybrids can be monitored.

After the data of the two half-ladders connected to one FADC have been processed, 8 words with the monitoring signal information are eventually appended to the output buffer (Format s. App. A.5).

---

[16] **N**egative **T**emperature **C**oefficient

3.2.2 Continuous updating of constants

As described above, the cluster search algorithm depends on the correct *pedestals* and *variances* of all readout strips that contribute to the raw data amplitude. In contrast to the common mode which can vary from event to event, the variations of these quantities are slow compared to the readout frequency, so that information from many events can be used for their determination.

The pedestals are caused by the individual leakage currents of the readout strips. An additional contribution is due to different capacitances of the pipeline cells of the APC. Therefore, an individual pedestal value is kept for each pipeline cell of a readout strip.

A further contribution to the raw data amplitude is due to electronic noise introduced by the charge sensitive preamplifier on the readout chip. These noise fluctuations can be calculated and are stored as the variances of the signal amplitudes (after a subtraction of common mode and pedestal).

The values of pedestals and variances are sensitive to temperature fluctuations (among other effects) so that the task of the CST constants updating routine is twofold:

1. an initial calculation of pedestals and variances after a reset of the readout system
2. the dynamic updating of valid constants during normal running

Since the processing time spent for the updating procedure ($\approx 9\,\mathrm{ms}$, s. below) has to be added to the 5.8 ms that are needed by the hit finding algorithm, it is clear that the limit of 10 ms for the total processing time would be exceeded if an update took place with every event. In 1997, the updating procedure was executed every fourth event. As shown below, this is still sufficient to compensate even large fluctuations of the constants reasonably fast.

The CST keeps pipeline-buffer dependent pedestals in 32-bit words, which amount to a total of $10240\,\mathrm{strips} \times 32\,\mathrm{pipeline\,buffers} \times 4\,\mathrm{bytes} = 1280$ kBytes per readout module. The sigmas are not considered to be buffer dependent. Four 32-bit words per strip are kept (s. below), so that $10240\,\mathrm{strips} \times 4\,\mathrm{words} \times 4\,\mathrm{bytes} = 160\,\mathrm{kBytes}$ of memory space are needed[17].

Initialization: For the CST, a pedestal of a readout strip i and pipeline cell p is introduced as:

$$PED_{ip} = (RAW_{ip} - CM) \times PedScaleFactor \tag{3.6}$$

The reason for scaling the pedestal is the need for a higher precision than the "natural" 12-bit delivered by the FADCs. Otherwise, the dynamic updating algorithm would not be sensitive to fluctuations (s. Eq. (3.10)). The factor used in 1997 has been 64, which is equivalent to a bit-shift of 4. After a system reset, the first 64 events (for every pipeline cell) are used for initialization, that is the mean value for the above defined pedestals is calculated. After $32 \times 64 = 2048$ events (on average) one has obtained valid pedestals.

The next 1024 events are then used for initializing the variances. For every readout strip, the *pulse-height-sum* of the events j is accumulated:

$$PHS_i = \sum_{j=1}^{1024} (RAW_i^j - PED_i/PedScaleFactor - CM^j) \tag{3.7}$$

---

[17] One RIO2 readout module thus keeps $1280 + 160 = 1440\,\mathrm{kBytes}$ of readout constants. With 8 modules employed, the total amount of readout constants for the CST is 11.25 Mbytes.

Different pipeline cells are not distinguished here. The squares of the pulse-heights are also summed:

$$PHS_i^2 = \sum_{j=1}^{1024} (RAW_i^j - PED_i/PedScaleFactor - CM^j)^2 \tag{3.8}$$

After 1024 events the variance can be calculated from the mean values of the two sums:

$$VAR_i = \frac{1}{1024} PHS_i^2 - (\frac{1}{1024} PHS_i)^2 \tag{3.9}$$

The pulse-height-sum and the sum of squares are stored in memory for the dynamic updating (s. below). Internal counters guarantee that the hit finding starts only after valid constants have been established.

Dynamic updating: For updating the pedestals a "pseudo-pedestal" is calculated from the data of the current event (Eq. (3.6)) and added to the old pedestal with a certain weight:

$$PED_{new} = (1 - weight) \times PED_{old} + weight \times PED_{pseudo} \tag{3.10}$$

Currently, a weight of $\frac{1}{64}$ is being used. In Fig. 3.5 it is shown that, given a typical magnitude of the pedestals of 50 ADC counts, this algorithm only works for scaled quantities or for floating point arithmetics. A pure integer calculation is sensitive neither to a sudden pedestal jump (left) nor to a slow rise (right). The updating has followed the sudden jump after ≈250 events. This means that in reality, with an update taking place every fourth event and having 32 pipeline buffers, some 32000 events would be needed until a good agreement with the current pedestal is reached. At event rates of

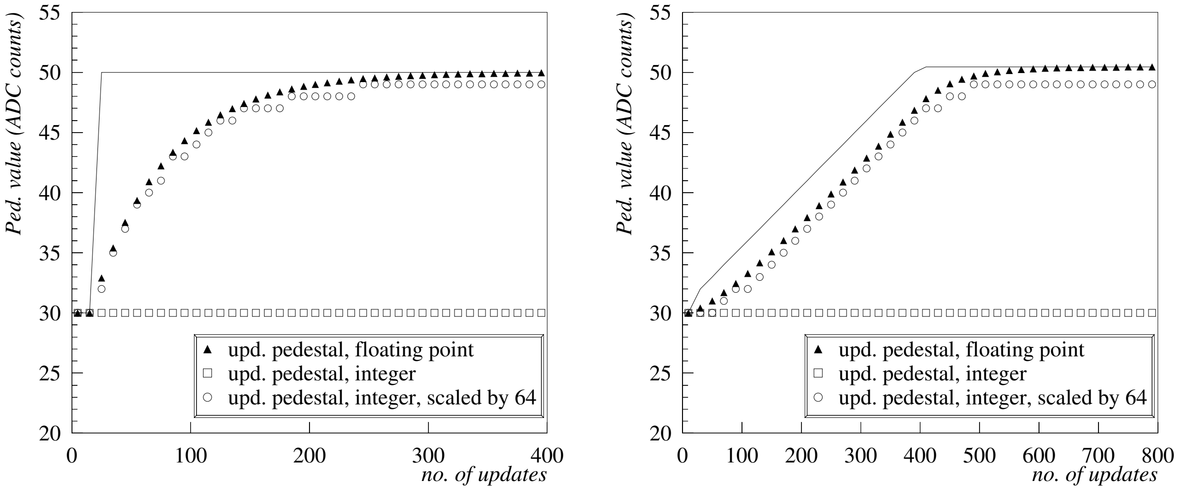

Figure 3.5: *Simulated pedestal behaviour with different data types. The line simulates the evolution of the "real" pedestal: a sudden jump of 66% (left) and a steady rise (right). The open circles show the updated values as produced by the implemented algorithm.*

50 Hz, this takes about 10 minutes. In the case of a slow drift, e.g. due to temperature variations, the update has followed the drift after 100 events corresponding to 4 minutes.

For the variances (Eq. (3.9)), a similar event-by-event update of the pulse-height-sum PHS and the sum of squares PHS^2 has proven to be inefficient for two reasons:

1. integer arithmetics sometimes leads to large fluctuations when subtracting quadratic terms
2. pulse height contributions from hit strips lead to wrong sums and variances

Therefore it was decided to accumulate PHS and PHS^2 according to Eq. (3.7) and (3.8) also during normal running. New variances can then be calculated periodically according to Eq. (3.9). With the updating routine being executed for every fourth event, new variances are then available after $4 \times 1024 = 4096$ events.

In order to exclude contributions from hit strips the sums are accumulated only if

- the pulse-height is below 2σ
- the strip has no hit (the “hit bit” of the raw data word is checked, as explained in Chap. 3.2.1)

For the variances, updating therefore means adding the pulse-heights from the current event to the sums. The number of valid “updates” is counted for every strip and also stored in memory. After 1024 update-events a new value for the variance is calculated if the number of valid updates for a given strip is greater than (1024/4), otherwise the old variance is kept. This could possibly lead to strips never getting new (i.e. better) variances: the *hot* strips that show an increased occupancy. If the number of valid updates for a strip is below (1024 – 64) which corresponds to an occupancy above 6%, the strip is marked as *hot* by setting an unused bit of the word that counts the valid updates. In this case, the sums will be accumulated even if the strip has a hit. The scheme is sketched in Fig. 3.6.

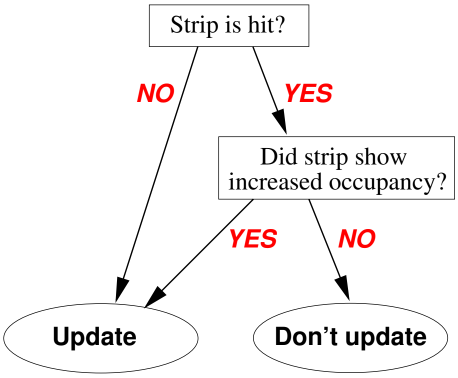

Figure 3.6: *Updating scheme for the variance of CST strips*

The average execution time for the updating routine consisting of a pedestal update as in Eq. (3.10) and of adding the pulse-height to the sums was found to be 9.1 ms in 1997 (s. Fig. 3.12).

3.2.3 Code implementation[18]

As described above, the routines for analyzing strip detector data are contained in a module separated from the firmware part of the readout software. Connection between the two layers is made by a single function call during the readout procedure of an event. Before executing the analysis routines it is therefore necessary to initialize the code on each module correctly, in particular to decide on CST or BST processing.

This is done by evaluating the *arguments* of the routine call. They are:

---

[18] This section is intended as a documentation of technical details for experts.

`SiMode`: readout mode (s. Section 3.1.3)
`Raw_Address`: address of raw data buffer for this event
`PPCunit`: no. of RIO2 board
`PIC`: pipeline counter as delivered by the XiLinX logic
`Hit_Address`: address of hit data buffer to write to
`*Nbytes_Hit`: length of data written to hit buffer
`*Ierror`: error code

The last two arguments are expected to be returned with proper values after the hit finding has finished. The routine then checks (and eventually modifies) the PowerPC's hardware implementation dependent register 0 (HID0)[19] in order to optimize the processor performance. The following bits have to be set:

- Bit 16: instruction cache enable
- Bit 17: data cache enable
- Bit 24: serial instruction execution enable
  this allows to benefit from the parallel processor architecture (it has several processing units that can work in parallel and thus increase the execution speed).
- Bit 29: branch history table enable
  this improves the conditional execution performance: the processor keeps a history of the code branches together with a prediction table for taking a specific branch. Specific to the PowerPC 604 architecture is the dynamic branch prediction: the probability levels assigned to a particular instruction depend on its history. The processor hence "guesses" which instruction is carried out next and can start fetching data and instructions in advance.

After having done some validity checks on the input arguments, the routine then decides whether the readout module is currently processing CST or BST data by checking the `PPCunit` number[20] and then evaluates all the necessary information to be able to process the data of each of the 8 connected FADCs sequentially. For this purpose, the following information is assembled for each of the FADCs:

- number of the RIO2 board and the FADC
- logical value which allows to exclude an FADC from being processed
- addresses of the Raw, Pedestal and Sigma data
- addresses of more constants (optionally)

CST and BST not only use different algorithms for the hit finding but also have their readout constants in the memory organized differently.

After this "setup" follows a `SiMode` switch. For the default case (Hits&Cluster mode) the actual hit finding routine is called for the 8 FADCs. In every fourth event, the constant updating routine is called additionally. The timing register of the processor is read out before and after the hit finding and the updating routines thus providing information about the time needed for the tasks.

---

[19] See [50] or [51] for information about the PowerPC 604 architecture.

[20] The 1997 setup had CST and BST modules in the same crate.

After all data have been processed and the found hits have been written to the specified buffer, the data header for the RIO2 board is filled. The event block is now ready to be collected by the master VMEtaxi processor. Before returning to the firmware task, some bits of the HID0 register have to be reset. Details on the implementation can be found in [52].

3.3 Slow control

The term slow control refers to the control and the supervision of detector parameters that vary slowly with respect to the event rate, i.e. that are not related directly to the data acquisition. Slow control tasks have to be initiated regularly during data taking by the shift crew operating the H1 detector. A major concern for their implementation is therefore robustness and simplicity. For the operation of the H1 silicon trackers there are two slow control tasks:

- controlling the voltages for the detectors and the readout chips
- loading sequencer code to the control modules OnSiRoC

The setup for the **voltage control** is different for the CST and the BST: the CST uses the OnSiRoC power supplies (cf. Chap. 3.1.1) while the BST uses custom-built power-download stations.

Both detectors use Macintosh computers that communicate directly with the voltage supplies via a MacVEE/Mac7212 interface [53, 54]. Dedicated graphical user interfaces cater for an easy operation and supervision of the parameters set. These applications include an online display of the voltages, and, in the case of the CST, also a display of leakage currents measured on the converter cards after the re-conversion of the optical analog signal as well as of temperatures measured on the endring printed circuits of the detector (Fig. 3.7). The applications also provide logging routines, so that a

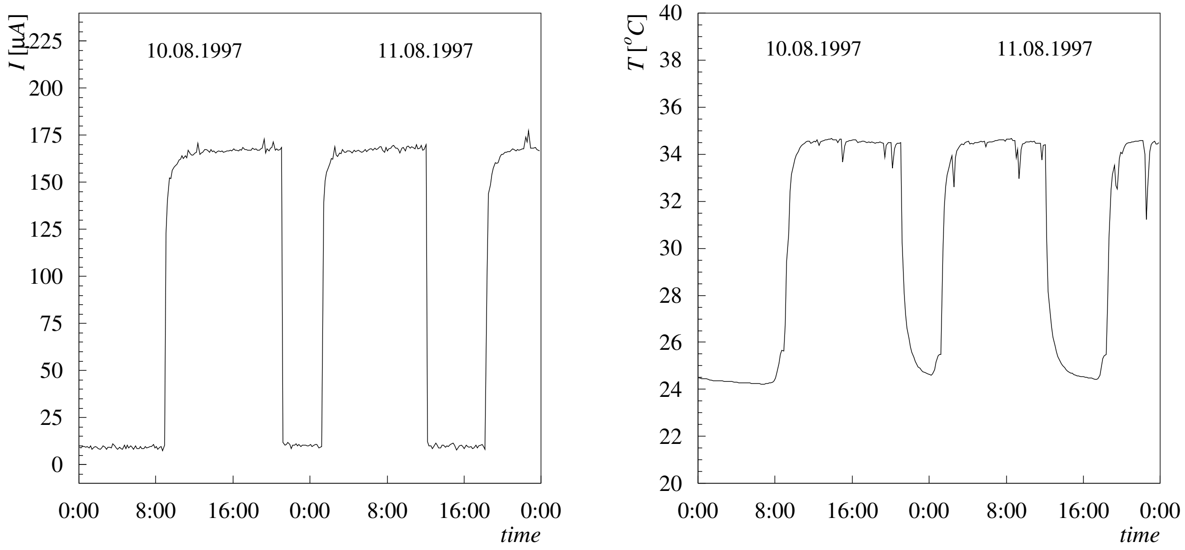

CST leakage current CST temperature

Figure 3.7: *Histograms of CST leakage current and temperature. The switching on and off of the detector voltage is reflected by immediate jumps of the currents and by slightly delayed temperature changes.*

detailed history of the detector operation parameters is available. Particularly interesting is the long-term evolution of the leakage currents which indicates the radiation damage of the silicon sensors. Fig. 3.8 shows the leakage current as measured on one of the CST converter cards for the whole 1997 data taking period. No significant increase is seen, an observation which has been confirmed by laboratory measurements in the 97/98 shutdown. It can be concluded that the protection of the detector from synchrotron radiation is sufficient.

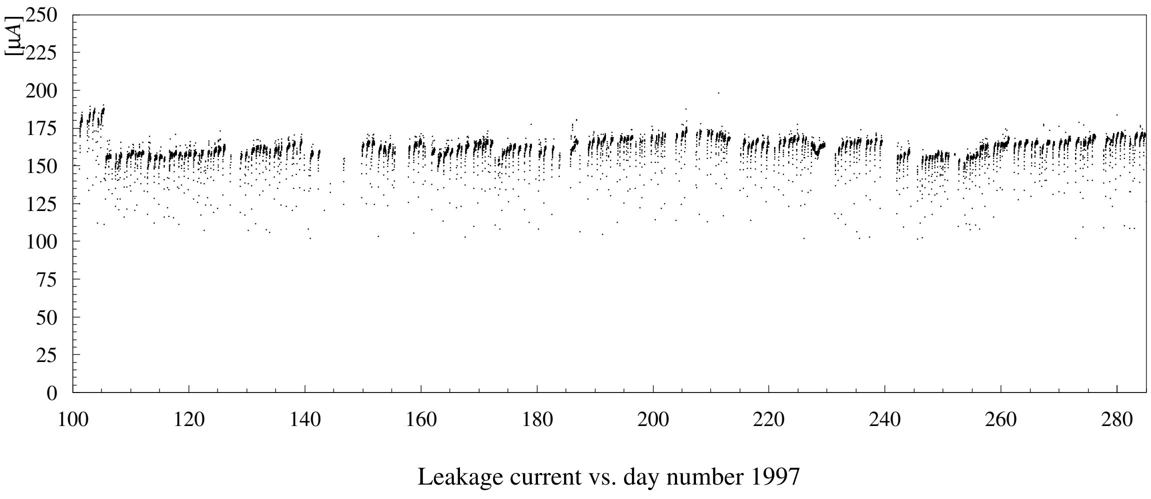

Figure 3.8: *Long-term history of the leakage current of the CST. The period covered ranges from 09.04.97 until 11.10.97. A cut has been applied on the detector voltages being off. The step at day number 105 is due to an adjustment of the bias voltage.*

For the **downloading of the sequencer code** to the OnSiRoCs, a common system is used by the two subdetectors. The idea is to keep the correct code and do the loading centrally. As mentioned in Chap. 3.1.1, binary files with sequencer instructions are created employing a compiler on a Macintosh computer. Different sequencer files are used for CST and BST. A dedicated application on this computer allows the downloading of the sequencer files to a reserved memory module via the VMEbus. This memory area can be addressed also via the fibre-optic VMEtaxi link that connects all crates of the silicon data acquisition branch.

The sequencer code is then loaded from the memory module into each of the OnSiRoCs on a *Warmstart*. This is a command issued centrally for all readout branches of the H1 experiment. Its purpose is in general to reset and initialize all front-end processors, i.e. processors that handle data before they are merged into the central data acquisition system. Implementing the sequencer loading on this stage ensures a maximal reliability.

Technically, the Warmstart command is sent from the H1 System Supervisor to the master VMEtaxi processor of the silicon branch. This processor identifies all OnSiRoCs, i.e. determines their VME addresses, and then copies the sequencer code from the memory module to the OnSiRoCs. Finally, the OnSiRoCs are initialized for data taking, which means that the registers controlling their operation are set to the correct values.

To activate the silicon detectors the shift crew hence has to:

- switch the CST voltages on
- switch the BST voltages on
- perform a *Warmstart* to load the sequencer code and to initialize the OnSiRoCs

The RIO2 processor modules responsible for digitization and online hit finding (cf. Chap. 3.1.2) are initialized automatically and do not need operator intervention.

3.4 Online data monitoring

Given the complex algorithms involved in the readout process and the size reduction of the data of the silicon detectors, it is clear that a dedicated system for an online monitoring of the performance of the readout processors and in particular of the hit finding algorithms is mandatory. For this purpose, the *Silicon Farm* was commissioned, a multi-processor system that receives fully assembled data blocks of the Silicon branch (cf. Chap. 3.1.4) and allows their evaluation by means of filling histograms.

These histograms can be viewed online and provide the opportunity of monitoring the performance of the readout system as well as the quality of the data. For the operation of the Silicon Farm, the following design goals were envisaged:

- keeping the need for user intervention minimal while as much information as possible is made available. To a large extent, the monitoring program is therefore entirely *data driven*, which means that it adapts automatically to the different types of data the Silicon branch produces[21].
- making an easy re-configuration of the program that fills the histograms possible. Due to the large number of channels that have to be supervised it is not possible to keep in memory let alone display all of the possibly interesting quantities of all detector strips at the same time[22]. It is however necessary to be able to access this information if desired, e.g. if a specific section of the detector seems to behave strangely. The strategy for the online monitoring software is hence to deliver an overview on the operation of all readout channels by default while letting the user decide which part of the system is to be monitored in more detail. For the selected part (e.g. a specific readout chip), special histograms are then created.
- offering the possibility of incorporating offline reconstruction software. This is meaningful since the data blocks processed by the Silicon Farm already have their final format which is written to tape, so that offline software can be employed without modifications.
- establishing connection to the slow control programs of CST and BST. For the CST for example, the data contain calibration voltages and voltages proportional to the temperature on the front-end hybrids (“specials”, cf. Chap. 3.2.1). These voltages are read out on the hybrids and are being processed in the same way as data from the detector strips. The online monitoring program extracts the hybrid temperatures and transfers them to the memory area of the CST slow control application. The latter then graphically displays the temperatures.

The following section describes the components and the software of the Silicon Farm. Online histograms are presented in Chap. 3.4.2.

---

[21] This corresponds to the readout modes introduced in Chap. 3.1.3.

[22] Histogramming just pulse-heights, noise, and a hitmap for all strips would mean keeping ≈ 100 Mbytes of histograms.

3.4.1 Components and software for the Silicon Farm[23]

The components of the Silicon Farm which are sketched in Fig. 3.9 are contained in the so-called *Master Monitoring Crate* of the Silicon branch and consist of several processor- and memory boards.

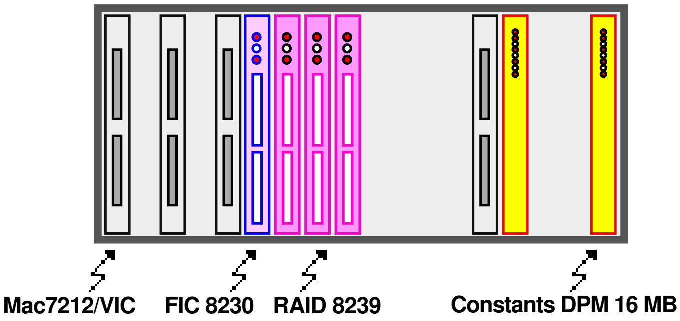

Figure 3.9: *Components of the Silicon Farm*

The central unit is a FIC8230[24] controller [55] which is the master processor in the crate. It has access to the memory boards, controls the programs on the other processors, and is able to communicate with the master VMEtaxi processor of the Silicon readout branch. Like on the RIO2 readout processors a mailbox concept is employed, thus no operating system is needed.

Three RAID8239 processor modules [56] perform the actual monitoring task, whereas three battery-backed up DPM8242[25] memory boards [57] are used to store object code to run on the processor boards (and to be loaded at startup) and constants for the online monitoring. One of the memory boards is employed to store the sequencer code for the OnSiRoCs, as described in Chap. 3.3. The crate is connected to a Macintosh computer via a MacVEE/Mac7212 interface [54]. There, a graphical user interface displays the status of all components and allows a configuration of the software.

For the evaluation of an event data block that has been assembled by the master VMEtaxi processor, the FIC acts as a data distributor: incoming events are buffered and transferred to the system memory of a RAID board that is flagged as free. The RAID boards then perform the monitoring task which essentially consists of filling histograms kept in each RAID memory. These histogram blocks can be accessed from the connected Macintosh computer in the control room via the VMEbus and displayed using a slightly modified version of the standard H1 online histogram viewing program KOOL [58].

Software layout

The online monitoring task consists of three software parts running on three different processors:

1. software for the FIC that handles the data stream and also user interventions
2. the monitoring and histogramming software itself that runs identically on the three RAID processor boards
3. the user interface on the Macintosh in the H1 control room

The **FIC part** of the software is written in Assembler and executed automatically on system startup to ensure maximum stability. The FIC is the master processor of the monitoring system. Communication with the RAID processor boards and the user interface application is established by means of dedicated memory areas (“mailboxes”), a concept used throughout the Silicon DAQ branch. This concept avoids overhead from using an operating system. The FIC is also connected to the master VMEtaxi processor of the Silicon readout branch, so that it receives information about the status and the selected parameters of the readout system (cf. Chap. 3.1.3). If the data acquisition is running, the

---

[23] This section is a documentation of technical details.

[24] **F**ast **I**ntelligent **C**ontroller

[25] **D**ual **P**orted **M**emory

FIC copies event data blocks from the master VMEtaxi processor to its own memory from where they are transferred to one of the RAID processor boards, together with the event number.

The **RAID part** of the software is written in C in order to ease memory access and the handling of the structured data. It consists of two layers:

- the lower layer initializes the board and handles incoming events. It communicates with the FIC and reacts on user interventions. In case the data acquisition is running it identifies specific data banks and passes their addresses onto the upper layer.
- the upper layer is subdetector-specific. As mentioned in Chap. 3.1, CST and BST use slightly different data formats, and may need specific monitoring. The layer is comparable to offline software: rather than handling memory addresses, it knows about banks and the attributes they contain[26]. Specific histograms can be booked and filled using the fast histogram package LHIS that was developed for the H1-Level 4-Filter Farm [59].

On startup of the RAID program, the memory is set up first by defining addresses for:

1. the mailbox memory area that can be accessed from the FIC and from the user interface (at a fixed address)
2. a parameter block with parameters of the current data acquisition run that are copied from the FIC (fixed address)
3. two event buffers into which the FIC directs incoming data
4. a buffer for histogram data
5. several buffers for detector-specific constants (e.g. pedestals, noise sigmas)

The program then reacts on the run conditions (run start, run end, event) that are signaled by the FIC as well as on mailbox messages sent by the user interface. At run start, the appropriate histograms for the selected readout mode are booked (s. next section). If an event data block has been delivered by the FIC, it is scanned for known banks, for the SIFE bank in particular (cf. Fig. 3.4). At this stage, the event data block is also checked for its consistency. This means that the number of words contained in a bank and the length indicated in its header must match. If the structure of the data has been found to be reasonable, all relevant parameters, the addresses of the data banks in particular, are then passed to the upper software layer. Here, the contents of the data blocks are extracted and filled into the appropriate histograms.

The code for the two layers is compiled and linked on a remote workstation and then downloaded to the boards from the control Macintosh.

The **user interface** (SiMoCS) running on the Control Macintosh is also programmed in C using a Macintosh-specific graphics package. In its *main window* (Fig. 3.10) the status of the FIC- and the RAID processors is shown, namely which run and event they are processing, which parameters are set for the Silicon data acquisition branch, and the addresses of the memory buffers described above. These parameters are copied from the parameter blocks in the FIC- and RAID memories. Selecting and downloading object code to the processor boards as well as resetting and booting is also possible. Furthermore, the application allows to save the data in the RAID histogram buffers to the Macintosh hard-disk.

---

[26] It is possible to run offline routines on this software layer.

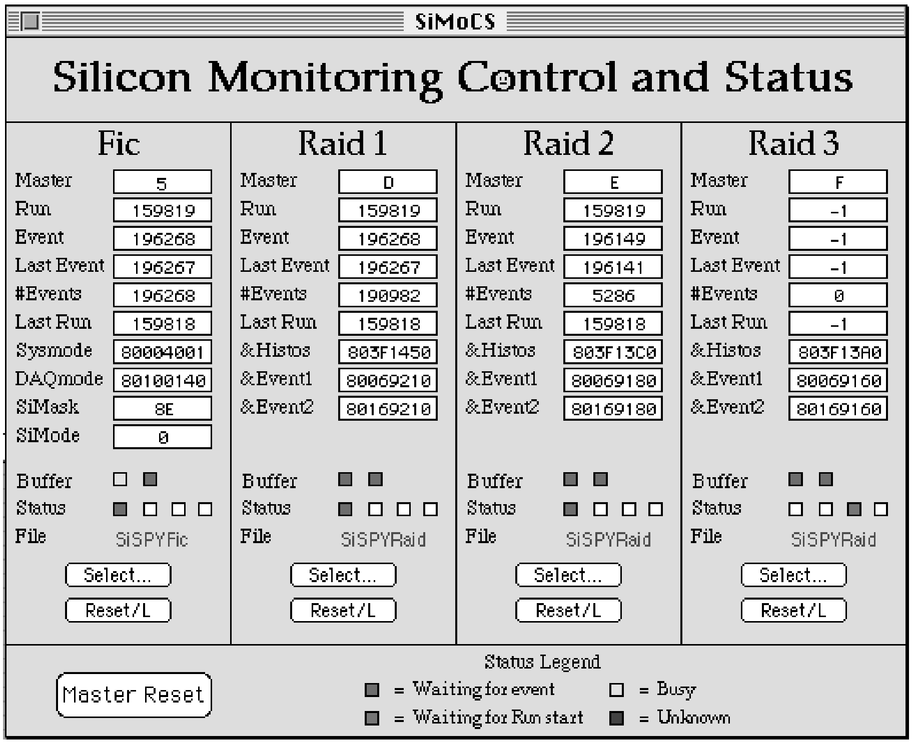

Fic
Master 5
Run 159819
Event 196268
Last Event 196267
#Events 196268
Last Run 159818
Sysmode 80004001
DAQmode 80100140
SiMask 8E
SiMode 0
Buffer ☐ ■
Status ■ ☐ ☐ ☐
File SiSPYFic

Raid 1
Master D
Run 159819
Event 196268
Last Event 196267
#Events 190982
Last Run 159818
&Histos 803F1450
&Event1 80069210
&Event2 80169210
Buffer ■ ■
Status ■ ☐ ☐ ☐
File SiSPYRaid

Raid 2
Master E
Run 159819
Event 196149
Last Event 196141
#Events 5286
Last Run 159818
&Histos 803F13C0
&Event1 80069180
&Event2 80169180
Buffer ■ ■
Status ■ ☐ ☐ ☐
File SiSPYRaid

Raid 3
Master F
Run -1
Event -1
Last Event -1
#Events 0
Last Run -1
&Histos 803F13A0
&Event1 80069160
&Event2 80169160
Buffer ■ ■
Status ☐ ☐ ■ ☐
File SiSPYRaid

Figure 3.10: *SiMoCS: Main window*

For each of the processor boards there is a *Console window* (Fig. 3.11) that captures output from the processor programs. This feature is essential for efficient debugging: in the picture the front-end data bank SIFE as found in one event has been printed to the console. Even low-level debugging via command line input is possible (useful if the monitoring task crashes). The steering of the monitoring software is done via a third window of the SiMoCS application. The user can select specific RIO2 modules, FADCs, APCs, or even strips. These parameters are copied to the RAID memories. The RAID program then books and fills extra histograms for the selected units (s. next section).

For details on the software implementation see [60].

3.4.2 Monitoring histograms

The histograms are kept separately in the memory of each RAID board. The viewing application SiKOOL runs on the control Macintosh and adds the histogram contents of the three boards automatically. The application allows the definition of *views*, groups of histograms that are to be displayed together.

By default, the monitoring system of the Silicon branch produces 3 different types of histograms:

1. histograms with information about the Silicon Farm itself
2. histograms about status and operation of the RIO2 readout modules
3. sub-detector-specific histograms filled from data of CST or BST

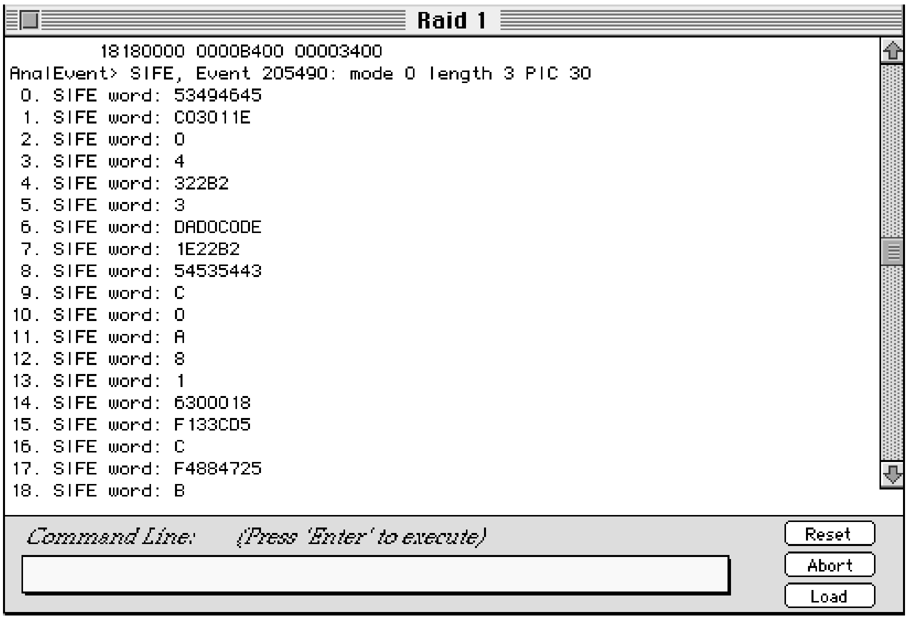

```
        18180000 0000B400 00003400
AnalEvent> SIFE, Event 205490: mode 0 length 3 PIC 30
 0. SIFE word: 53494645
 1. SIFE word: C03011E
 2. SIFE word: 0
 3. SIFE word: 4
 4. SIFE word: 322B2
 5. SIFE word: 3
 6. SIFE word: DADOCODE
 7. SIFE word: 1E22B2
 8. SIFE word: 54535443
 9. SIFE word: C
10. SIFE word: 0
11. SIFE word: A
12. SIFE word: 8
13. SIFE word: 1
14. SIFE word: 6300018
15. SIFE word: F133CD5
16. SIFE word: C
17. SIFE word: F4884725
18. SIFE word: B
```

Figure 3.11: *SiMoCS: Console window for RAID board #1*

The histograms of the latter two types depend on the contents of the event data blocks. If formatted data have been written by the readout modules, and the SIFE bank hence contains header words from the individual modules (cf. Chap. 3.1.4 and Fig. 3.4), information on the performance of the readout processors can be extracted from the data. In this case, the following histograms are filled for all readout modules having contributed to the event:

- data length
- time needed for the hit finding routine
- time needed for the constant updating routine
- pipeline counter
- no. of raw data buffers that are occupied

Fig. 3.12 shows as an example a set of histograms for one RIO2 readout module processing CST data. Explanations are given in the figure caption. These histograms are identical for all readout modules.

On the contrary, histograms displaying information extracted from the data words may be different for CST and BST data. Moreover, they do also depend on the types of the data blocks (cf. Tab. 3.2). As an example, again histograms for the RIO2 module #1 that processes CST data are presented. The readout mode was Hits & Cluster, which is the default mode (cf. Chap. 3.1.3). In this case a detailed hit map providing one bin per strip and distributions of the pulse-heights and of the noise sigmas are histogrammed. These quantities are contained in the data words in a bit-compressed form, cf. Chap. 3.2.1 and App. A.5. Fig. 3.13 shows the hit maps for the 8 FADCs of the readout module. Each of the histograms no. 10100-10107 has 1280 bins. It can be seen that in general the occupancy level is uniform for all readout strips though some do show an increased activity. These strips get a special treatment after the next application of new sigmas (cf. Chap. 3.2.2). The sigma distributions

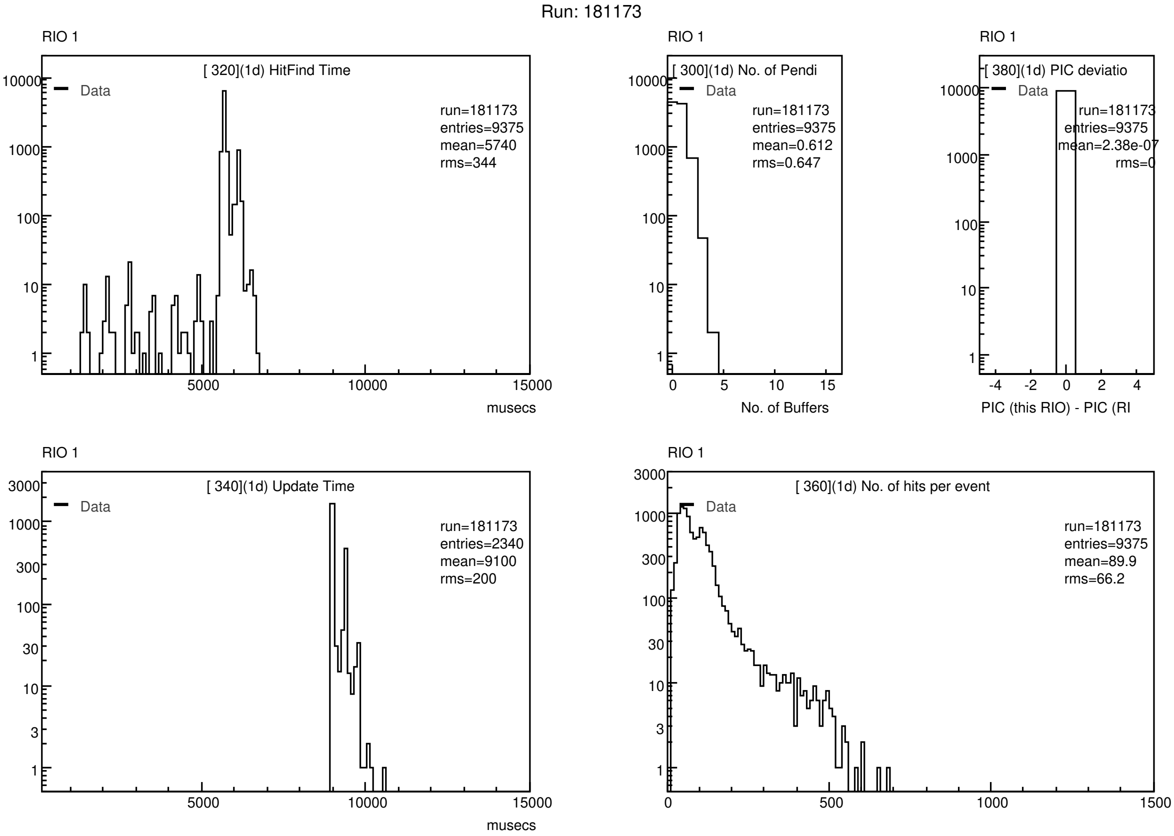

Figure 3.12: *Online histograms for the performance of the readout module RIO 1. Histograms displayed from top left:*
No. 320 shows that the average time for the hit finding routine is 5.7 ms. The peaks at lower values are due to the routine being interrupted if too many hits have been found.
No. 300 indicates that up to 4 (of 16 in total) raw data buffers are flagged as occupied during processing. This number is event-rate dependent and shows the number of yet unprocessed events: the "load" of the board.
No. 380 shows that the pipeline counter as used on this RIO board shows no deviation to the reference pipeline counter.
No. 340: the average time for the constants updating routine is 9.1 ms.
No. 360: the average data length is about 90 32-bit words corresponding to a size reduction factor of 57. However, a considerable fraction of larger events exists.

for the same readout strips are contained in Fig. 3.14 and show that the noise level for the contributing strips is in general stable at the level of about 20 ADC counts.

If raw data are found in the event block, the monitoring program books and fills histograms that display the raw data amplitude for every readout strip of one selected readout module. This raw data "event display" provides a means to test the basic functionality of the detectors. In particular, dead regions can be identified, and the DC level of the analog pulses can be checked.

During the 1997 running, the above mentioned histograms had been predefined for all RIO2 modules in readout giving a total number of about 500 histograms using $\approx$900 kBytes of memory. Additionally, it was possible to "zoom into" the shown distributions: e.g. displaying the pulse-height or sigma

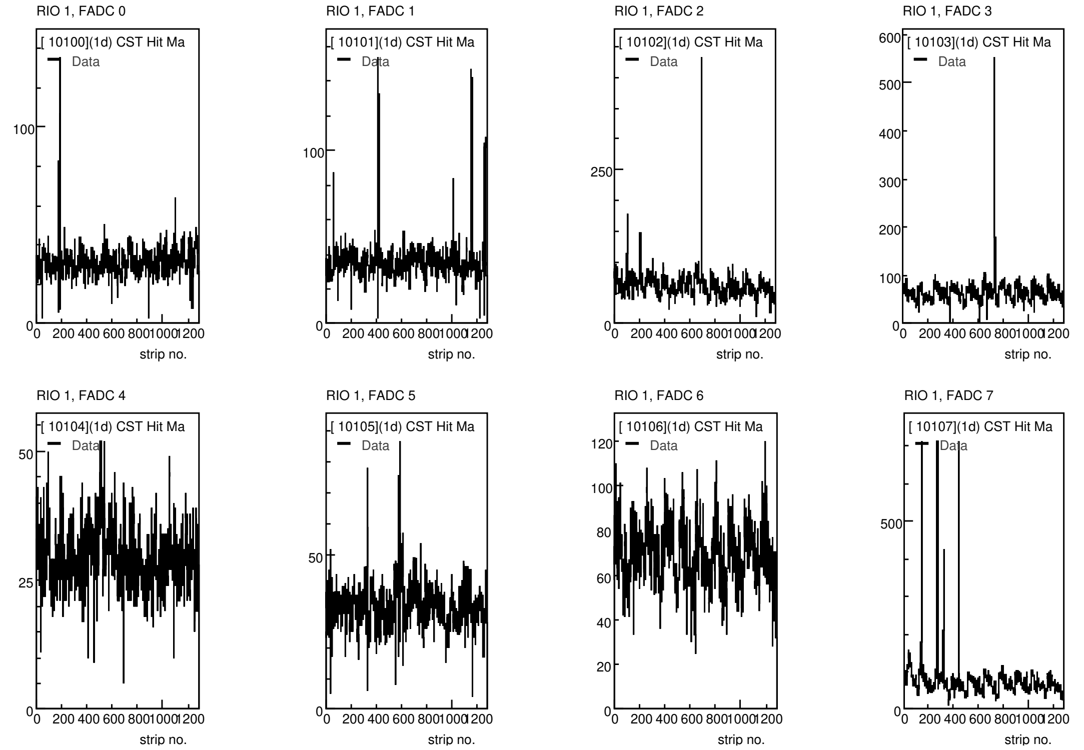

Figure 3.13: *Online hitmap for the channels processed by the readout module RIO 1*

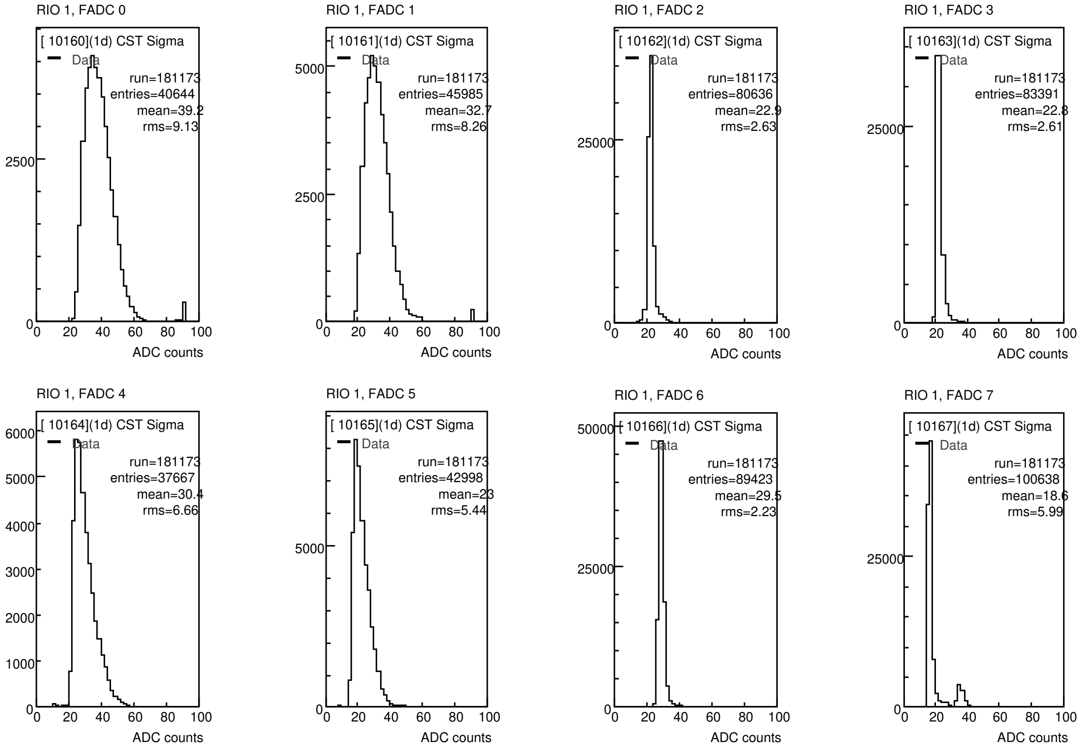

Figure 3.14: *Online noise sigma distributions for the channels processed by the readout module RIO 1*

distribution for a specific readout chip or even for a specific strip by selecting the desired unit through the graphical interface on the Macintosh. In this way, it is for example possible to check whether the second peak in histogram no. 10167 (Fig. 3.14, bottom right) stems from a specific group of strips. These histograms of “regions of interest” are only booked on user request.

Chapter 4

Event reconstruction with the vertex detector CST

The vertex detector CST measures up to four spacepoints for each particle traversing the detector. The offline reconstruction has to find these spacepoints and transform them into H1-coordinates. The high precision of the CST measurement as compared to the track measurement in the Central Jet Chamber allows a considerable improvement of the track parameters. This improvement is achieved by means of a combined track fit with the CST spacepoint parameters and the CJC track parameters as input. The final goal is then to determine the primary and all secondary vertices in every event precisely.

4.1 Overview

The CST reconstruction module CSTREC (flow diagram depicted in Fig. 4.1) reads the front-end data banks as written by the RIO2 readout boards (cf. Chap. 3.1.4). It then performs the following steps that will be described in the following sections:

1. offline cluster reconstruction (Chap. 4.3)
2. transfer of found clusters to spacepoints in H1-coordinates (Chap. 4.4)
3. assignment of spacepoints to tracks measured in the CJC (Chap. 4.5)
4. combined fit of spacepoint- and track-parameters (Chap. 4.6)

As output, CSTREC writes a bank containing the local clusters and a bank containing track parameters from the combined fit. For the assignment and the fit of the spacepoints the track parameters as reconstructed by the CJC have to be read in. The improved track parameters are utilized for the determination of run-vertex parameters (Chap. 4.7).

Vital for a consistent reconstruction is the application of the correct alignment corrections to the CST spacepoints. Their determination is performed independently of the CSTREC software module and is briefly sketched in Chap. 4.2. For the 1997 data taking period, the alignment constants have been determined and are available for the reconstruction.

The software module is designed to conform with the standards of H1 software. It is planned to run doing the offline reconstruction (L5) as well as on the L4 filter farm. The software hence makes use of

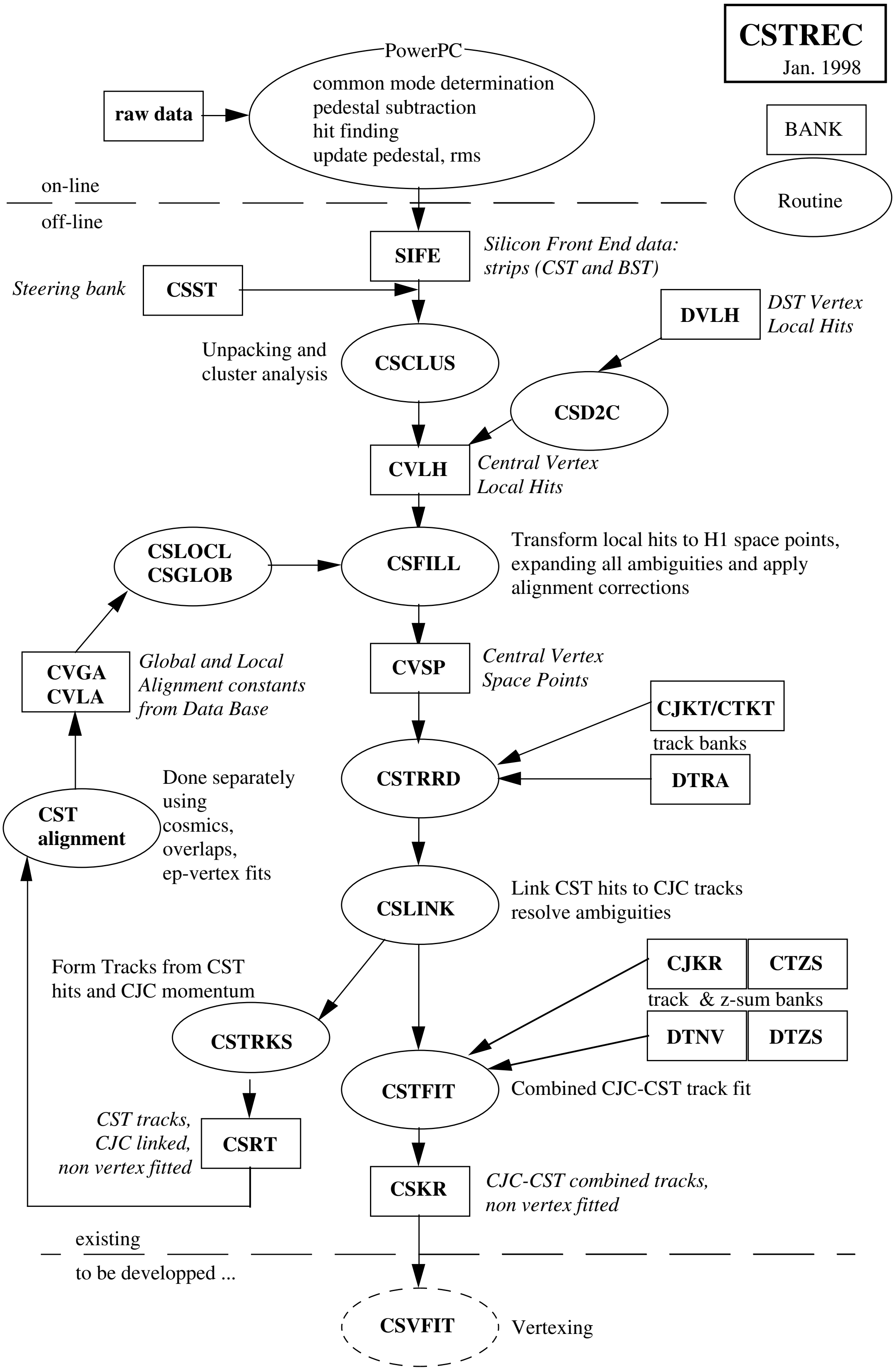

Figure 4.1: *Flow diagram of the CSTREC reconstruction module*

the BOS system for data management [61]. Data are organized in *banks* which can have a predefined format (→ *table*). Banks read and written by CSTREC will be introduced in the appropriate sections.

4.2 Alignment

In order to benefit from the precision of the CST measurements that are of the order of 10μm, the correct alignment of the detector with respect to the surrounding subdetectors, namely the central jet chambers, is mandatory. A commonly employed method is the calculation of alignment constants from the measured data (software alignment).

The alignment procedure is divided in two parts:

- The local alignment constants parameterize the deviation of each detector half-ladder from its nominal position. With six parameters per half-ladder (three translations and three angles, Fig. 4.2), a total of 384 values have to be determined. Six constraints are applied to the 384 parameters in order to keep the position of the whole detector unchanged.

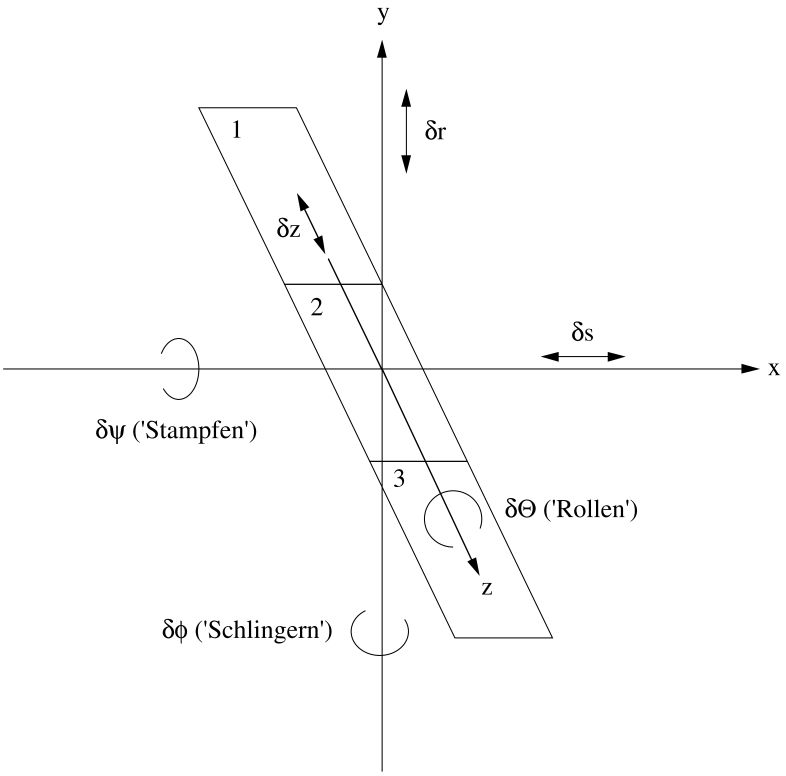

Figure 4.2: *Local alignment parameters for a CST detector half-ladder: three translations and three Euler angles.*

- Another six degrees of freedom are allowed for the CST as a whole. The global alignment constants describe the deviation from the nominal CST position with respect to the CJC.

The procedure for the CST starts with the assignment of measured clusters to tracks from the CJC (cf. Chap. 4.5). Then, helix tracks are calculated that pass exactly through the linked clusters by using the position of the clusters in outer and inner layer of the CST and taking the curvature from the linked CJC tracks. In the following, these tracks are referred to as *forced* tracks. Their determination is described in Chap. 4.6.3. Two data sets are employed for calculating the alignment constants:

- data from penetrating cosmic particles that traverse both CST layers twice. For these particles, two forced tracks can be calculated, one in the upper and one in the lower detector half. By matching the two track halfs the CST half-ladders can be aligned.
- data from electron-proton interactions. Here, the constraint that the tracks have to originate from a common vertex is utilized.

Furthermore, the overlapping geometry of the CST is exploited. Tracks that pass through two detector half-ladders in one layer impose additional constraints on the relative orientation of the two. In any case, the constants are determined by a constraint fit that is performed iteratively. Additional input is taken from laboratory measurements of the half-ladders that were carried out before the assembly of the detector.

The consistency of the alignment can be demonstrated by checking parameter distributions of cosmic track pairs. A cosmic ray muon is reconstructed as two track "legs" in the upper and lower detector part respectively whose parameters (Tab. 2.3) are correlated. An example is shown in Fig. 4.3: The

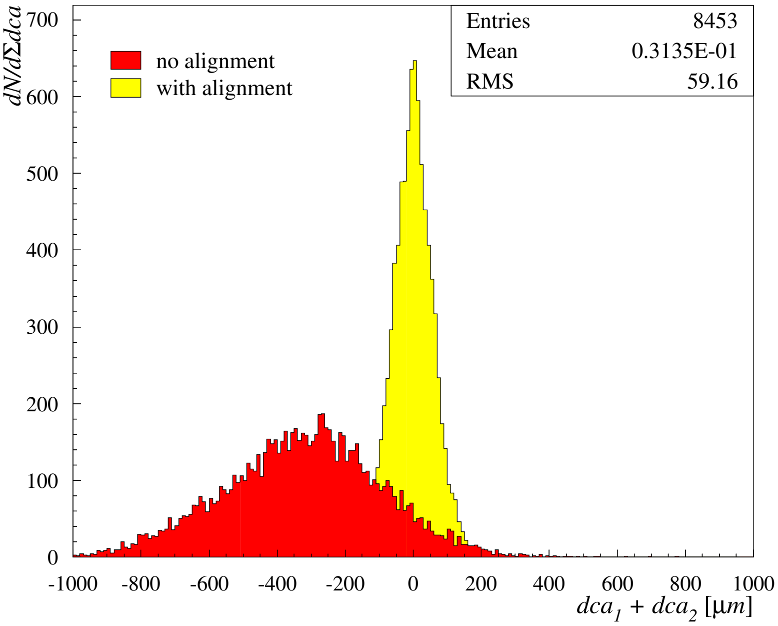

Figure 4.3: *Effect of applying alignment corrections to CST measurements. Dark histogram:* $dca_1 + dca_2$*-distribution for CST tracks without alignment corrections, light histogram: same tracks calculated with corrected coordinates for the CST measurements.*

sum of the *dca*-values of the two track halfs is centered at 0 and narrowed considerably after the application of the alignment corrections. The width of the distribution reflects the track resolution, s. Chap. 4.6 for detailed studies.

A single set of alignment constants turned out to be sufficient for the whole 1997 data taking period. They have been written to the H1 database and are available for the CST reconstruction software (s. Chap. 4.4).

4.3 Cluster reconstruction

The format of the CSTREC input bank SIFE has been described in Chap. 3.1.4. For every strip belonging to a cluster candidate, one 32-bit word containing the pulse-height PH, the variance VAR and the strip number n is available. Together with the FADC and the readout board number that are also contained in the bank, the strip can be assigned to a *detector half-ladder*, which is the basic entity for further reconstruction.

The offline cluster search is analogous to the online algorithm (cf. Chap. 3.2.1) albeit with stricter cluster cuts. A cluster candidate is formed by a number cw of consecutive strips each having a pulse-height that is greater than 1σ (where $\sigma = \sqrt{VAR}$). The cluster is accepted if the following condition holds:

$$(\sum_{i=1}^{cw} PH_i) > (\sum_{i=1}^{cw} \sqrt{VAR_i}) \cdot CSTOfflineClusterCut \tag{4.1}$$

where $CSTOfflineClusterCut$ equals 5 for p-side clusters and 4 for n-side clusters respectively[1]. For an accepted cluster the *Center of Gravity* CoG is calculated:

$$CoG = \frac{\sum\limits_{strips} PH_i \cdot n_i}{\sum\limits_{strips} PH_i} \tag{4.2}$$

This gives the position of the hit in units of the strip pitch (p-side: 50μm, n-side: 88μm). Finally, one row is added to the bank containing the CST cluster information (CVLH[2]) with the following information:

- half-ladder number
- flag for p- or n-side
- cluster center of gravity CoG in units of strip numbers
- no. of strips cw belonging to the cluster
- number of first strip in cluster
- cluster pulse-height $\sum_{i=1}^{cw} PH_i$ in ADC counts
- cluster significance: $sig = \sum_{i=1}^{cw} \frac{PH_i}{\sqrt{VAR_i}}$

The resulting distributions for the significance sig of the found clusters are plotted in Fig. 4.4. The light histograms show the distributions for all found clusters while the distributions for clusters that will later be linked and fitted to CJC tracks are overlayed (dark histograms). The noise hits are

---

[1] For the online algorithms, the cluster cut is 4 for both detector sides, cf. Eq. (3.5).

[2] **C**entral **V**ertex **L**ocal **H**its

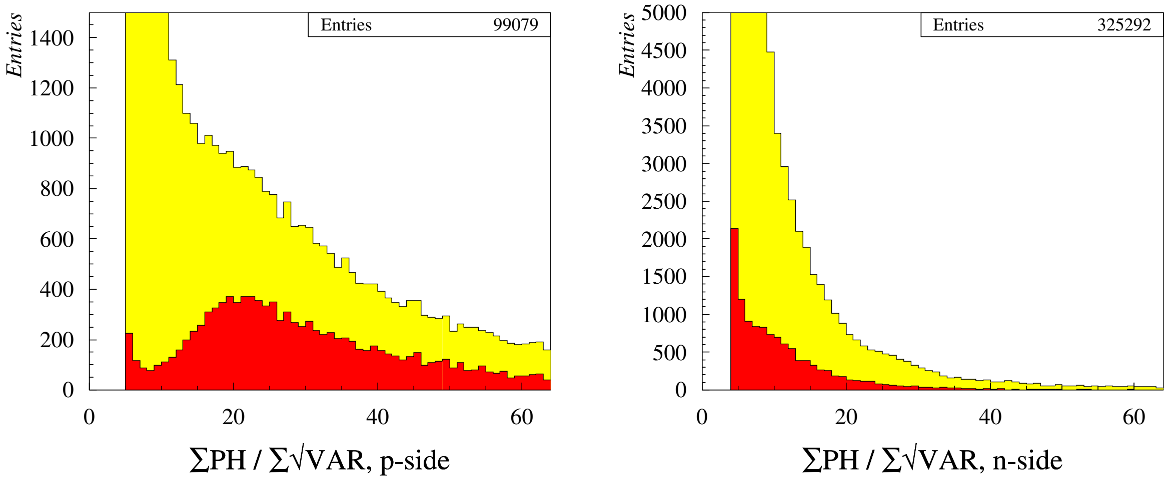

Figure 4.4: *Significance distributions for p- and n-side clusters. Light histograms: all clusters found; dark histograms: clusters linked and fitted to CJC tracks.*

dominant for both detector sides. On the p-side, the clusters contributing to the signal can clearly be separated, while a separation on the n-side is more difficult. The shape of the p-side distribution suggests to raise the cluster cut to 7σ provided the clusters below 7σ are falsely linked. The problem of separating noise hits and minimizing the level of falsely linked clusters is discussed in Chap. 4.5.

The much higher noise level on the n-side is due to the increased capacitance of the detector side which is caused by the double metalization that is needed to obtain the 90°-readout. It is also reflected in the fact that more than three times as many clusters are found on the n-side as compared to the p-side. This ratio can be reduced if the online routine only searches for n-side clusters if a hit has been found on the corresponding p-side, a feature that will be implemented for the 1998 data taking.

The width of the clusters is shown in Fig. 4.5. In both projections, it depends on the incidence angle ζ between the particle direction and the normal vector of the silicon sensor plane. The larger this angle is, the longer is the path length of the particle in the active material, and the higher the number of strips towards the charges drift (Fig. 4.6). On the n-side that measures the z-coordinates of the crossing tracks, ζ_n is related to the polar track angle Θ as $\zeta_n = \pi/2 - \Theta$. On the p-side, ζ_p is a function of all three track parameters κ, Φ, and dca. The large tails of the cluster width distributions are due to the low single strip threshold of 1σ in both the online (Eq. (3.4)) and the offline cluster search routines. Raising this cut would however lead to inefficiencies [32].

4.4 Calculation of spacepoints

The next step for the CST reconstruction is the combination of p- and n-side clusters to form three-dimensional *spacepoints*. The position information is obtained independently in R-Φ-coordinates (p-side) and in z (n-side). Due to the threefold ambiguity in z —3 silicon sensors are daisy-chained— it is for the present only possible to form *candidates* by combining position information of all p- and n-side clusters of one half-ladder. The ambiguities can only be resolved by assigning a track measured in the CJC to a spacepoint candidate (s. next section). The number of candidates NSP per event is

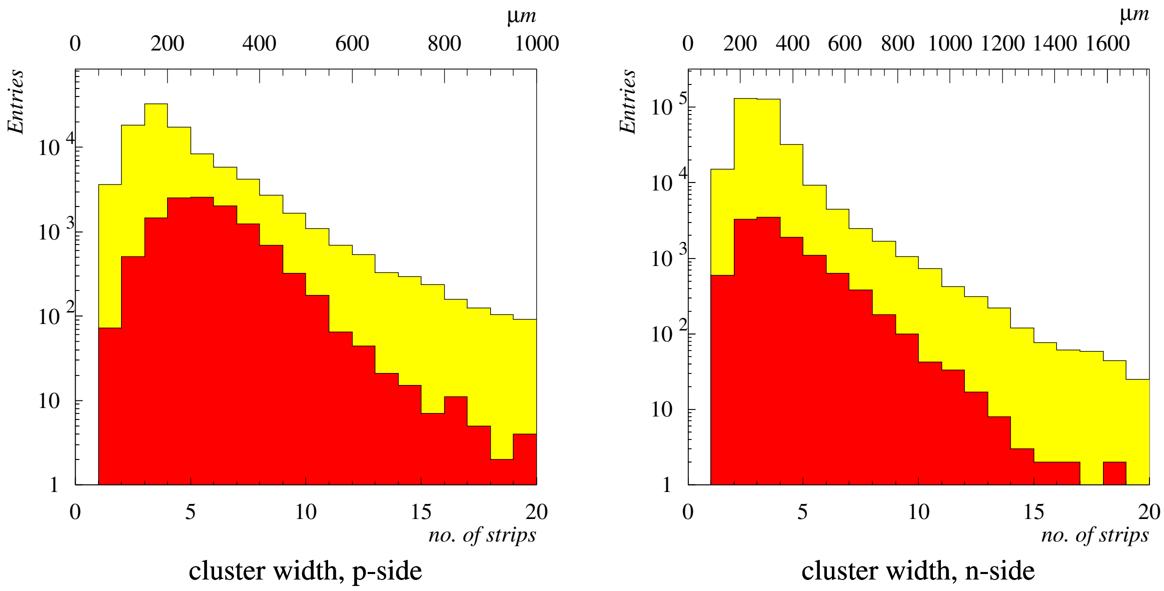

Figure 4.5: *Cluster width distributions for p- and n-side. Light: all clusters found; dark: clusters linked and fitted to CJC tracks.*

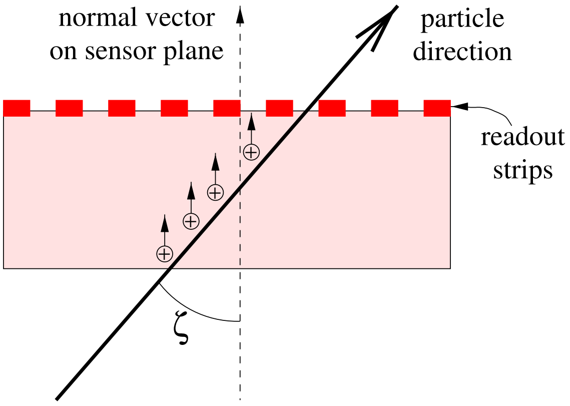

Figure 4.6: *Schematic drawing of the dependence of the number of strips carrying signal charge on the incidence angle ζ of the particle on the silicon sensor*

thus given by

$$NSP = \sum_{i=1}^{64} NCL_p^i \times NCL_n^i \times 3 \tag{4.3}$$

(NCL_p^i and NCL_n^i being the number of clusters found on a half ladder on p- and n-side respectively) and amounts to about 1500 per event. Each spacepoint is formed by transforming the local coordinates (half-ladder number and *CoG* in units of strip numbers) into (polar) H1-coordinates assuming ideal geometry for the CST. The final coordinates are then obtained by applying the alignment corrections to the spacepoint. For every spacepoint candidate the following information is stored in the CVSP[3] bank:

- coordinates (R, Φ, z)
- errors on the coordinates assuming intrinsic resolution
- internal references for further reconstruction: half-ladder number, ambiguity flag (the same clusters can form an inner, middle, or outer spacepoint w.r.t. $\pm z$)
- pointers to the clusters forming the spacepoint

The intrinsic resolution of the CST has been determined to be $15\,\mu$m in R-Φ and $\approx 25\,\mu$m in z (depending on the polar angle Θ of the track[4]) [34].

With the determination of the three-dimensional spacepoints, the “stand-alone” part of the CST reconstruction is finished. Any further steps need additional input from the Central Jet Chamber surrounding the vertex detector.

4.5 Track linking

Since the CST is a double-layered vertex detector, it cannot reconstruct tracks on its own: the combinatorial background from the combinations of *all* spacepoints in the inner and outer layer would be far too high so that the physically meaningful tracks could not be determined.

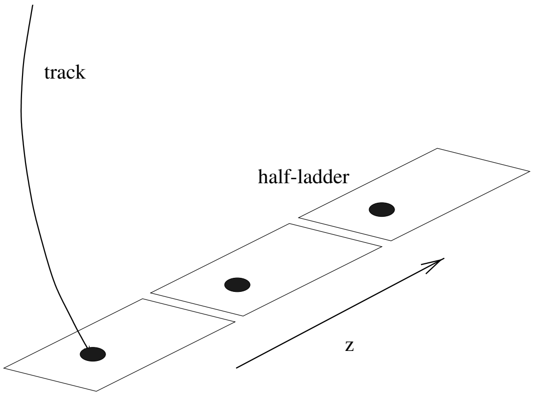

Figure 4.7: *Resolving the ambiguity in z by linking a track*

This is caused by the noise level of the detector and also by the fact that 3 z-strips share a common readout line which increases the number of hit candidates by 3 (Eq. (4.3)). Resolving the ambiguities and rejecting the noise hits can therefore only be achieved by assigning tracks measured in the CJC to spacepoints measured in the CST (Fig. 4.7). An important point in this respect is that tracks used for this purpose have been already *vertex-fitted* by the CJC reconstruction program. The additional vertex constraint results in a much higher precision of the track parameters and thus only allows a correct assignment.

The linking of CST spacepoints to tracks measured in the CJC is done by extrapolating the track onto the surface of the two CST layers and by calculating the *residuals* to the spacepoints measured on the respective half-ladder within a given tolerance in units of the track extrapolation error (5σ). The spacepoint with the smallest residuum is then assigned to the track. The procedure is done separately for the R-Φ- and the z-coordinates.

The quality of the assignment is closely related to the noise level in the detector: noise hits may be linked accidentally. Raising the hit- and cluster thresholds (Eq. (3.4), (3.5), (4.1)) however leads to inefficiencies since true clusters are also suppressed. Four cases of misidentification can occur:

a) a track is not linked since neither noise nor signal spacepoints are present.

---

[3] **C**entral **V**ertex **S**pace **P**oints

[4] The error on the z-coordinate of the spacepoint is therefore updated as soon as a track has been linked to it.

b) a track is not linked although a signal spacepoint is present within 5σ of the extrapolation error

c) a track is linked to a noise spacepoint though a signal spacepoint is present

d) a track is linked to a noise spacepoint since no signal spacepoint is present

In order to study these contributions one has to use simulations where signal and noise hits are known. Another possibility is the use of penetrating cosmic tracks that cross both layers of the CST twice. In this case a track is matched to three crossings, and the residuals of the fourth, the distances to the track in R-Φ and in R-z are studied. In this way it is possible to tag the signal hit and to compare it to the linked hit.

The results show the quality of the linking on the n-side to be much worse than on the p-side. This is due to several reasons that contribute to the misidentification cases:

- the lower signal-to-noise-ratio on the n-side (to case c) and d))
- the cluster cut (Eq. (4.1)) rejecting some signal hits (to case a) and d))
- the gaps in the active material along z (to case a), c), and d))

In particular it can be shown that the fraction of linked noise hits where the “real” signal hit was present (case c)) was $\approx 9\%$. This fraction can be reduced by employing an additional condition for the n-side linking: Fig. 4.8 shows that the shapes of the significance distributions for tagged signal clusters and for noise clusters are different. The shapes are parameterized by the two spline functions

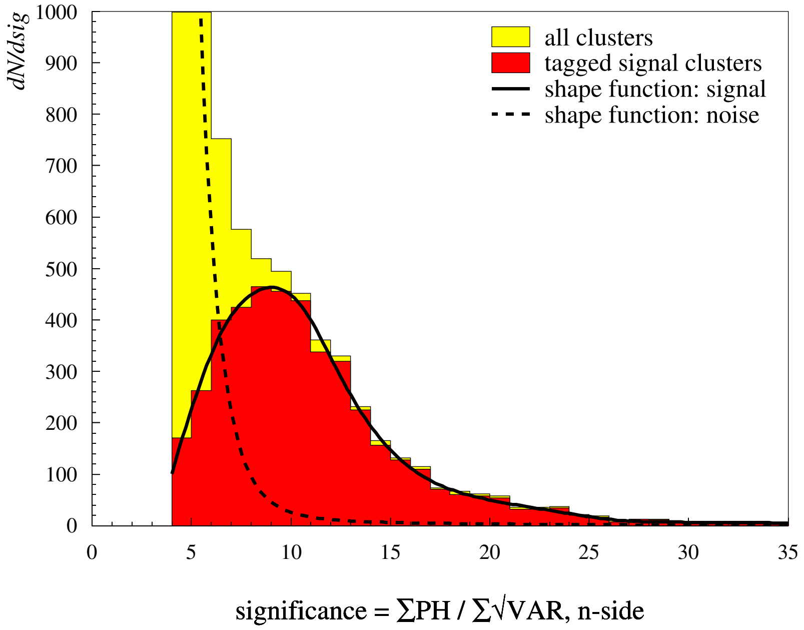

Figure 4.8: *Shape functions for separating signal- and noise clusters. Light histogram: all clusters on half-ladders crossed by a track, dark histogram: tagged signal clusters, solid curve: shape function* $S_{signal}(sig)$ *for signal clusters, dashed curve: shape function* $S_{noise}(sig)$ *for noise clusters*

$S_{signal}(sig)$ and $S_{noise}(sig)$. Instead of just taking the spacepoint with the smallest z-residuum, these shape functions are then considered as well. This is done by evaluating *probability functions* for all spacepoints to be signal or noise.

For constructing the signal probability function, a Gaussian extrapolation error for the z-residuum is assumed, and a weight w_S associated with the signal efficiency (92.5%) enters (σ_z is the z-error of the cluster):

$$P_S = w_S \cdot S_{signal}(sig) \cdot \frac{1}{\sqrt{2\pi}\,\sigma_z} \cdot \exp(-\frac{\Delta z^2}{2\sigma_z^2}) \tag{4.4}$$

For the noise function, a constant distribution is assumed, and the weight w_N is identified with the noise density on the sensors (0.66 cm^{-1})

$$P_N = w_N \cdot S_{noise}(sig) \tag{4.5}$$

The final criterion for a spacepoint to be assigned to a track is to have the largest value of

$$W_S = \frac{P_S}{P_S + P_N} \tag{4.6}$$

of all candidates on the respective half-ladder.

The application of this method in the n-side linking procedure reduces the number of wrong links where the correct one is present to $\approx$3% (s. Chap. 4.6.2). The significance distribution for the tagged signal clusters also shows that the 4σ-cut (Eq. (4.1)) on the cluster pulse-height already rejects signal hits. Lowering it further would increase the noise level dramatically and lead to more falsely assigned hits. Further improvements to the linking efficiency are expected by using the polar angle information one obtains when assigning two spacepoints in inner and outer CST layer to a track.

For the linking procedure on the p-side it was shown that $\approx$4% of all links were wrong. Due to the better signal-to-noise ratio an improvement was possible by raising the cluster cut (Eq. (3.5)) and simultaneously lowering the cut on the track extrapolation error. The first measure rejects more noise clusters while the second allows the linking to be more generous.

The improvements of the modified linking procedures are demonstrated in the next section describing the combined fits of CST spacepoints and linked CJC tracks.

Technically, the linking procedure updates the cluster- and the spacepoint banks (CVLH and CVSP) with pointers to the linked track.

4.6 Track fitting

The precise spacepoint information delivered by the vertex detector is used to improve the tracks measured by the CJC by means of a *constrained track fit*. Whereas the track–spacepoint-linking uses the *vertex-fitted* CJC-tracks that have already been improved by imposing a vertex constraint, the fit procedure goes back one step and takes the non-vertex-fitted, “original” CJC track parameters. Hence the combined CJC-CST track fit is independent of and almost unbiased by any vertex hypotheses. The track fit is carried out for R-Φ- and the R-z-projections separately (Chap. 4.6.1 and 4.6.2). The results will be compared to the ones obtained from the CST “forced” tracks, where the curvature is taken from the linked CJC track and a track is calculated that passes exactly through the two linked CST hits (Chap. 4.6.3).

4.6.1 Fit in the R-Φ-plane

For each CJC-track linked to n CST spacepoints, $3 + n \times 2$ variables are to be fitted:

- three track parameters from the CJC: curvature κ_{CJC}, azimuthal angle Φ_{CJC}, and distance of closest approach to the origin dca_{CJC}
- two parameters for each CST spacepoint: radius R and azimuthal angle Φ

The basic idea of the fit is that the vector x of these variables has to satisfy a set of *constraint equations* given by the fact that ideally, each of the CST spacepoints i should lie on a circle defined by the 3 CJC parameters (Fig. 4.9):

$$f(x)_i = \kappa_{CJC}\ (R_i^2 + dca_{CJC}^2) - 2\,R_i\ (1 + \kappa_{CJC}\, dca_{CJC})\ \cos(\Phi_i - \Phi_{CJC}) + 2\, dca_{CJC} \overset{!}{=} 0 \qquad (4.7)$$

where the index i denotes the spacepoint. The fit minimizes the corrections Δx to the *measured* quantities x using the least squares method. After all iterations

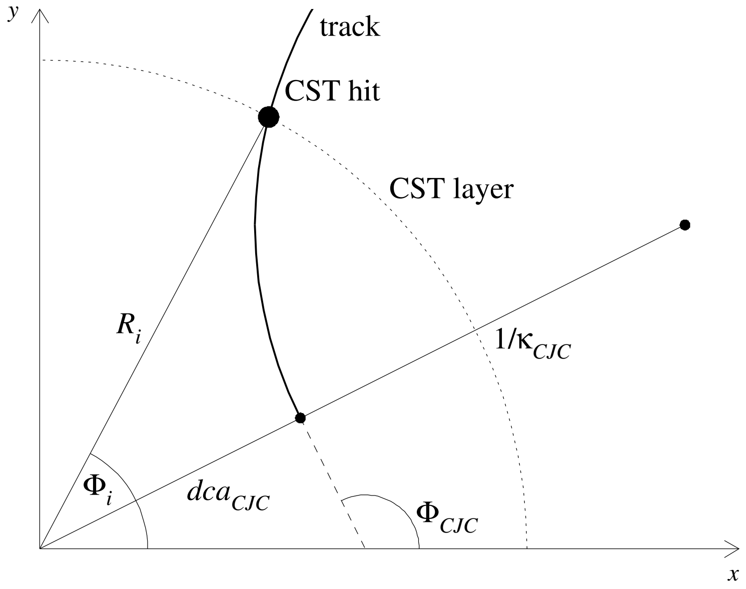

Figure 4.9: *Track and spacepoint parameters in the R-Φ-plane (= x-y-plane). A track parameterized by the variables κ_{CJC}, Φ_{CJC}, and dca_{CJC} crosses a CST layer (indicated by the dotted line) where the measured hit has the coordinates R_i and Φ_i.*

$$f(\hat{x}) = f(x + \Delta x) = 0$$

must hold. Using the least squares method, this is equivalent to

$$\Delta x^T V^{-1} \Delta x = \min \qquad (4.8)$$

where V is the covariance matrix of the parameter vector x. The corrections Δx are obtained using the method of Lagrange multipliers [62]. One introduces an additional parameter for each of the constraint equations and determines the minimum of

$$Q(\Delta x, \lambda) = \Delta x^T V^{-1} \Delta x + 2\lambda^T f(x + \Delta x) \tag{4.9}$$

Since the constraint equations (4.7) depend nonlinearly on the components of the parameter vector x the problem has to be solved iteratively. In each iteration, the equations are approximated by linear equations

$$f_{old} + A(\Delta x - \Delta x_{old}) = 0,$$

where Δx is the correction to be calculated, Δx_{old} are the correction values of the previous iteration, and f_{old} are the function values at $x + \Delta x_{old}$. The matrix A contains the derivatives $\partial f_j / \partial x_i$ calculated at the position of the previous values $x + \Delta x_{old}$. The problem of finding a minimum for Eq. (4.9) is then equivalent to solving the matrix equation:

$$\begin{pmatrix} V^{-1} & A^T \\ A & 0 \end{pmatrix} \begin{pmatrix} \Delta x \\ \lambda \end{pmatrix} = \begin{pmatrix} 0 \\ -f_{old} + A\Delta x_{old} \end{pmatrix} \tag{4.10}$$

The normal case for the CST reconstruction is that 2 spacepoints are linked to a track resulting in a total number of 7 fit parameters, 2 constraint equations, and the need to calculate 10 partial derivatives $\partial f_i / \partial x_j$ in each iteration. The software used for the constrained fit is standard H1 software [63] also applied in the CJC reconstruction module. After the final fit iteration the quantity

$$c = \Delta x^T \, V(\hat{x})^{-1} \, \Delta x$$

follows a χ^2 distribution with n degrees of freedom, where n is the number of constraint equations ($\equiv$ number of linked CST spacepoints).

Individual variables $\hat{x}_i$ can be tested statistically by studying the *pull-distributions*:

$$P = \frac{\hat{x}_i - x_i}{\sqrt{V(x)_{ii} - V(\hat{x})_{ii}}} \tag{4.11}$$

These quantities should have the properties of a standardized Gaussian distribution: a mean value of 0 and a width of 1. The pulls are particularly sensitive to the values $V(x)_{ii}$ of the input covariance matrix. In our case these are the errors on the track parameters delivered by the CJC and the uncertainties of the CST spacepoints which are identified with the intrinsic resolution. An important step in this respect is to correct the parameters and covariances measured in the CJC for energy loss and multiple scattering of the particle before it reaches the CJC itself. The energy loss and the resulting change of the particle momentum are calculated by means of evaluating the Bethe-Bloch formula for the different layers of material the particle traverses (each having a specific radial thickness and radiation length). The uncertainties on the track parameters introduced by multiple scattering are calculated according to Eq. (2.5) and (2.6).

However, the pull distributions for κ, Φ, and *dca* (Fig. 4.10) show that the values of their elements in the input covariance matrix are still not correct.

A scaling of the values of the CJC-elements in the covariance matrix by a factor of 2.5 (increasing the errors by $\sqrt{2.5} = 1.6$) improves the situation (Fig. 4.11).

Introducing a scaling factor for the CJC track parameter uncertainties can be justified since the CJC is known to have had operational problems during the 1997 data taking period. These led not only to a

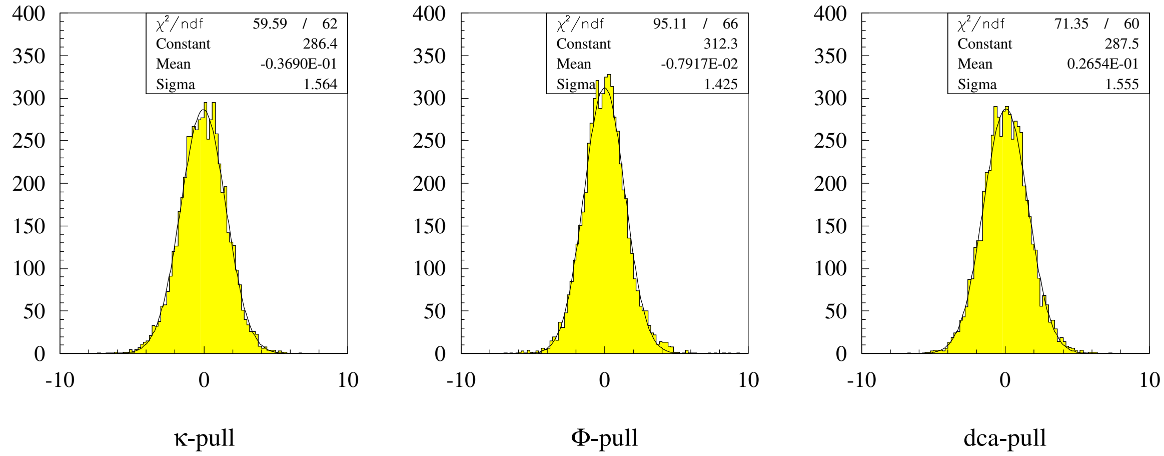

Figure 4.10: *Pull distributions with unmodified covariance matrices*

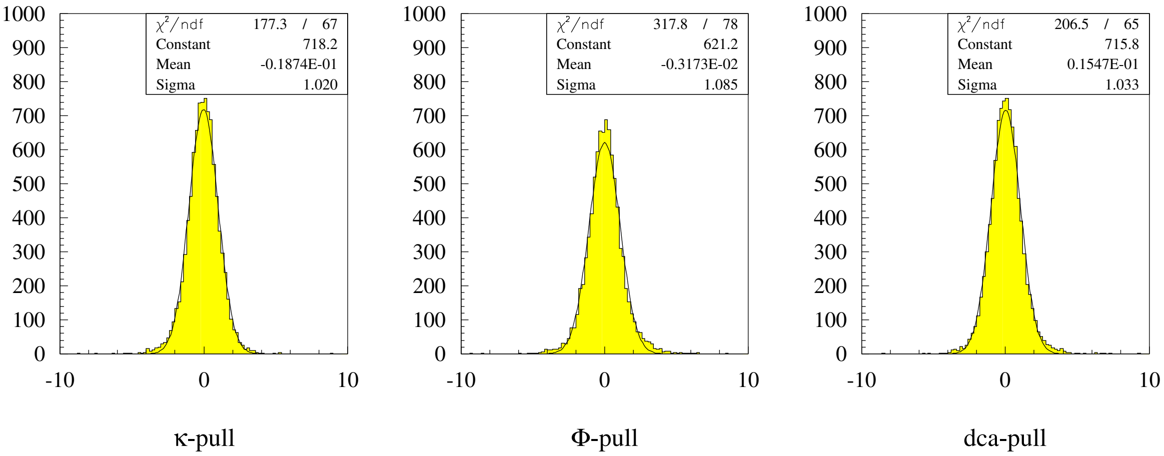

Figure 4.11: *Pull distributions with CJC errors increased by a factor of 1.6*

loss in efficiency, but also to uncertainties in the calibration which in turn affects the track parameter resolution[5].

Technically, the track fit starts with the list of CJC vertex-fitted tracks to which the CST spacepoints have been assigned (Chap. 4.5). If one or more linked hits have been found, the non-vertex-fitted origin of the linked track is looked up. Before performing the constrained fit, energy loss and multiple scattering corrections are calculated for the track parameters and covariance matrix elements. One has to allow for these corrections since a particle traverses material before being measured in the CJC[6]. After a successful fit, the resulting parameters are again corrected for multiple scattering in the beam pipe because it has to be traversed by the particle before being measured in the CST. The new

---

[5] The CJC2 was completely rewired during the 1997/98 shutdown.

[6] The corrections are therefore dependent on the radius where the first CJC hit was found and on the polar angle Θ of the track

parameters for the R-Φ-coordinates of the track are then stored in a track bank (CVFT[7]) together with the number of linked spacepoints, the χ^2 of the fit, the index of the original linked CJC track, and the indices of the individual CST spacepoints. The CVFT bank is later updated by parameters obtained by a fit in the R–z-plane.

An event with tracks as reconstructed by the CJC and as improved by the fit using CST spacepoints is shown in Fig. 4.12.

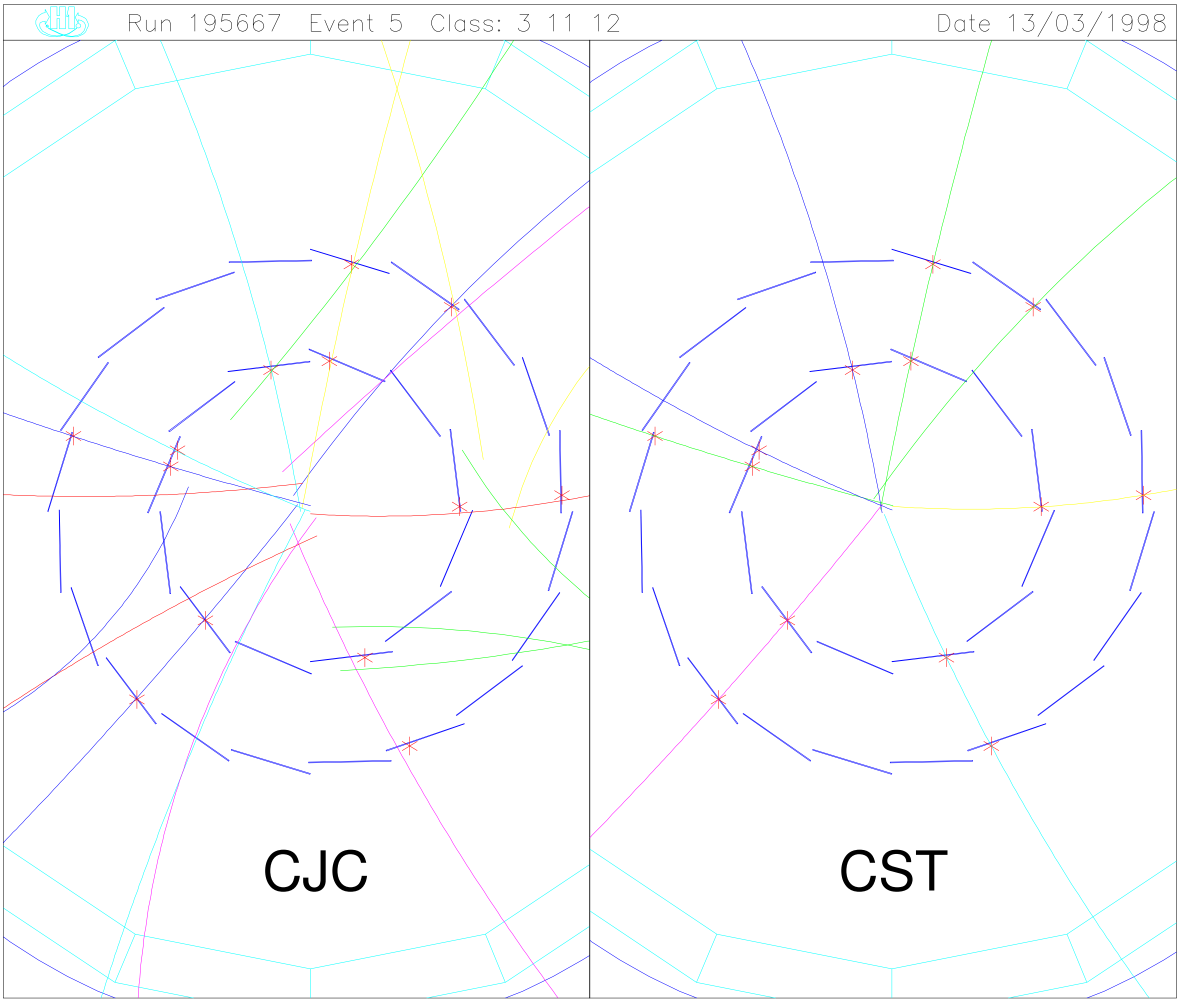

Figure 4.12: *R-Φ-view of an event with CJC tracks (left) and CST–CJC fitted tracks (right)*

---

[7] **C**entral **V**ertex **F**itted **T**racks

Quality of the track fit The quality of the track fit can be checked by studying cosmic ray muons traversing the two CST layers twice. They are reconstructed as two track "legs" (Fig. 4.13) whose parameters have to fulfill the following criteria given the H1-coordinates conventions (cf. Chap. 2.3.2):

$$\begin{aligned} \kappa_1 + \kappa_2 &\overset{!}{=} 0 \\ |\Phi_1 - \Phi_2| &\overset{!}{=} \pi \\ dca_1 + dca_2 &\overset{!}{=} 0 \end{aligned} \tag{4.12}$$

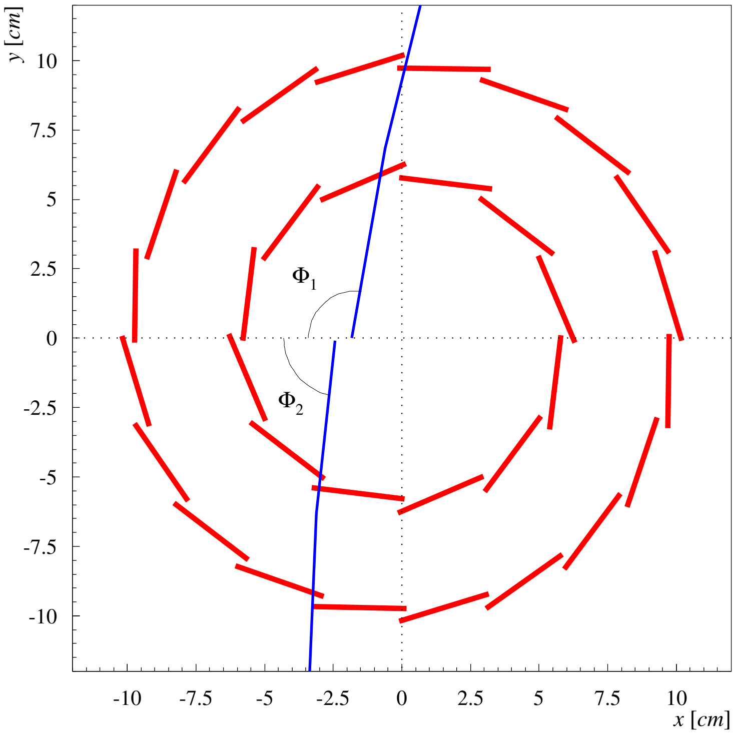

Figure 4.13: *R-Φ-view of a cosmic ray muon reconstructed as two "legs" in the CST. The differences of the track parameters are exaggerated.*

In the CJC reconstruction program a fit using the above conditions is performed with cosmic track candidates. The resulting tracks are used for the CJC–CST linking where they take the part of the vertex-fitted tracks in *e*-*p*-data processing.

A comparison of the fitted parameters with the ones measured by the CJC alone shows the benefits of using the precise CST spacepoint information: Fig. 4.14 contains the three distributions (Eq. (4.12)) for the fitted tracks and for the original tracks measured by the CJC. To be able to neglect any effects from multiple scattering, only tracks with a transverse momentum p_t greater than 4 GeV have been considered. The following characteristic parameters can be extracted:

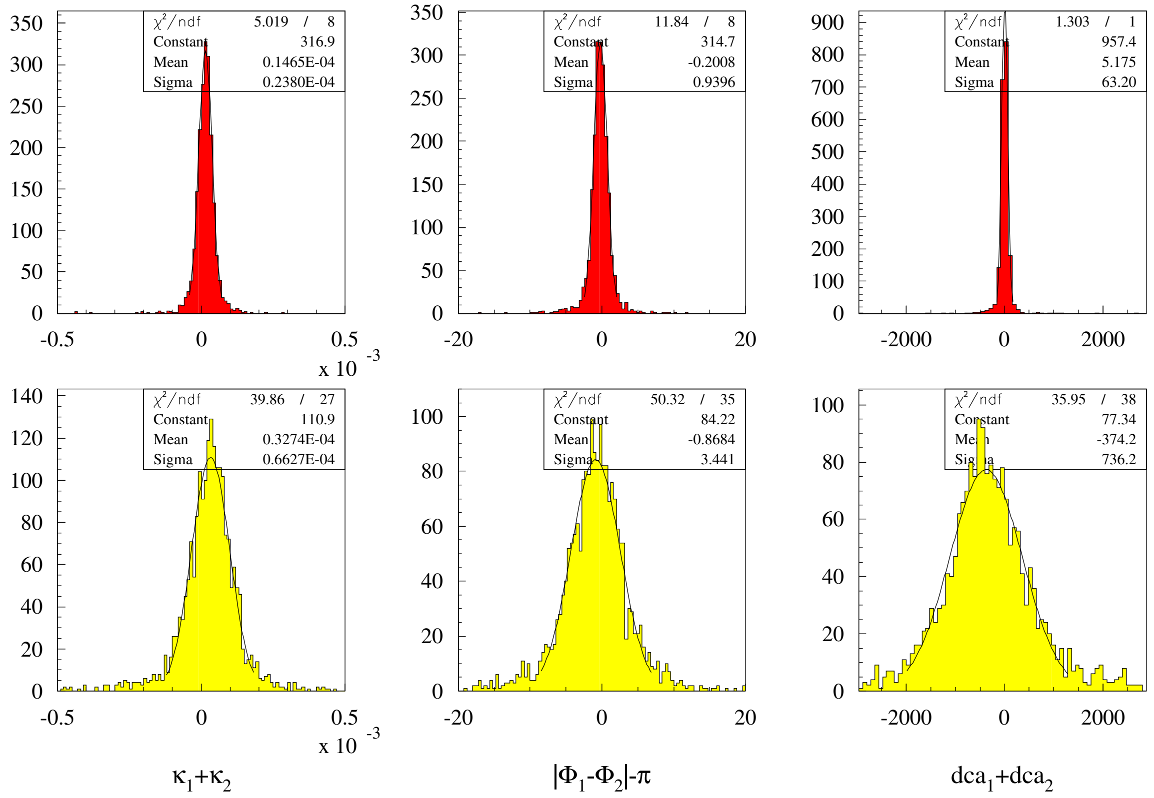

Figure 4.14: *Characteristic distributions for a cosmic track pair. Top: parameters measured by CJC+CST. Bottom: parameters measured by CJC only*

		CJC alone	CST–CJC
$\kappa_1 - \kappa_2$	mean	3.27×10^{-5} cm^{-1}	1.47×10^{-5} cm^{-1}
	width	6.63×10^{-5} cm^{-1}	2.38×10^{-5} cm^{-1}
$\lvert\Phi_1 - \Phi_2\rvert - \pi$	mean	-0.87 mrad	-0.2 mrad
	width	3.4 mrad	0.94 mrad
$dca_1 + dca_2$	mean	-374.2 μm	5.2 μm
	width	736.2 μm	63.2 μm

The resolution of the κ-peak is improved by a factor of 2.5, for Φ by a factor of 3.5, and for the *dca* by a factor of 11. The fact that the distributions for the parameters obtained using CST measurements are centered at 0 shows that the CST is properly aligned.

The mean value of the *dca*-peak for the CJC track parameters however shows a significant deviation from 0 which indicates that deficiencies in the detector alignment or the reconstruction itself must be present. Moreover, the position of the distribution shows a dependence on the track incidence angle Φ (Fig. 4.15). This inconsistency deteriorates the resolution of the fitted tracks.

For a single track linked and fitted to CST spacepoints the following resolutions can be deduced from the 2-leg parameter distributions:

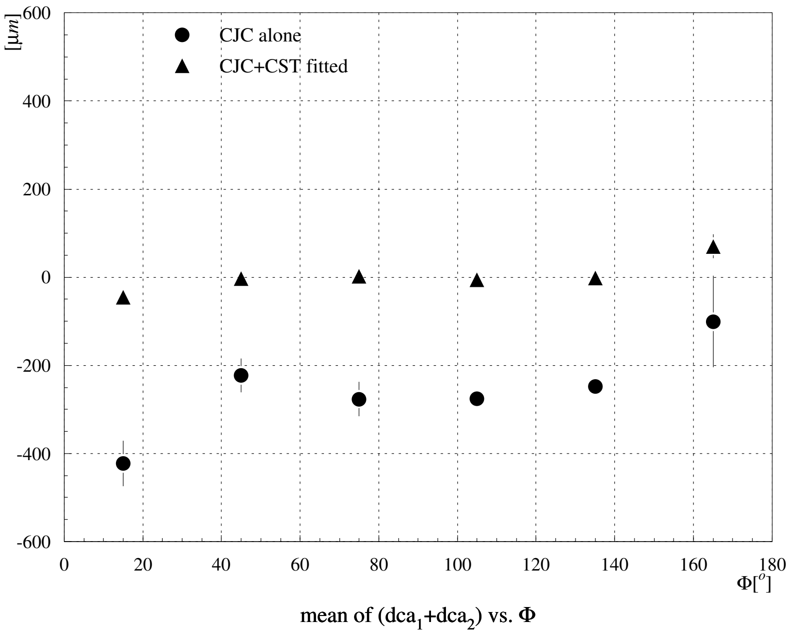

Figure 4.15: *Mean value for* $dca_1 + dca_2$ *as a function of the track angle* Φ *(Errors are statistical)*

$$\begin{aligned} \sigma(\kappa) &= 1.68 \times 10^{-5}\,\mathrm{cm}^{-1} \\ \sigma(\Phi) &= 0.7\,\mathrm{mrad} \\ \sigma(dca) &= 44.7\,\mu\mathrm{m} \end{aligned}$$

These values, especially the one for the *dca*, should improve in 1998 provided that the inconsistencies of the track parameters as reconstructed by the CJC have disappeared. They are compatible with the intrinsic resolution of the silicon sensors (cf. Chap. 4.4) which entered the fit as an input value of the covariance matrix. The resolution is sufficient to resolve the beamspot by doing a subsequent primary vertex fit which means that for the first time, it is now possible to determine the primary event vertex with an accuracy higher than the one given by the dimensions of the beam spot. For a given event, the quality of the vertex fit will however depend on the fraction of low-energetic tracks whose resolution is deteriorated by multiple scattering.

The distributions for the cosmic tracks can also be used to study the efficiency of the p-side linking. As mentioned in Chap. 4.5, a fraction of ≈4% of the links on the p-side is wrong and leads to outliers in the parameter spectra. Part of those are due to linked noise hits where the signal spacepoints would have been present. The significance distribution for the p-side clusters (Fig. 4.4) suggests to rise the default cut of 5 on this quantity to 7, thus lowering the noise level. Simultaneously, the cut on the track extrapolation error on the sensor surfaces is relaxed from 5σ to 10σ. The resulting distributions for the *dca*-sum of the two cosmic track legs are shown in Fig. 4.16. The number of successfully fitted track pairs is slightly higher (+ 1.6%) which is due to the relaxed track extrapolation error cut. At the same time the ratio of entries under the peak is enlarged from 89.4% on the left to 92.6% on the right. This shows that p-side clusters with a significance below ≈7 are indeed due to noise. Since each of the entries corresponds to 4 linked spacepoints, this is equivalent to a raise of the fraction of

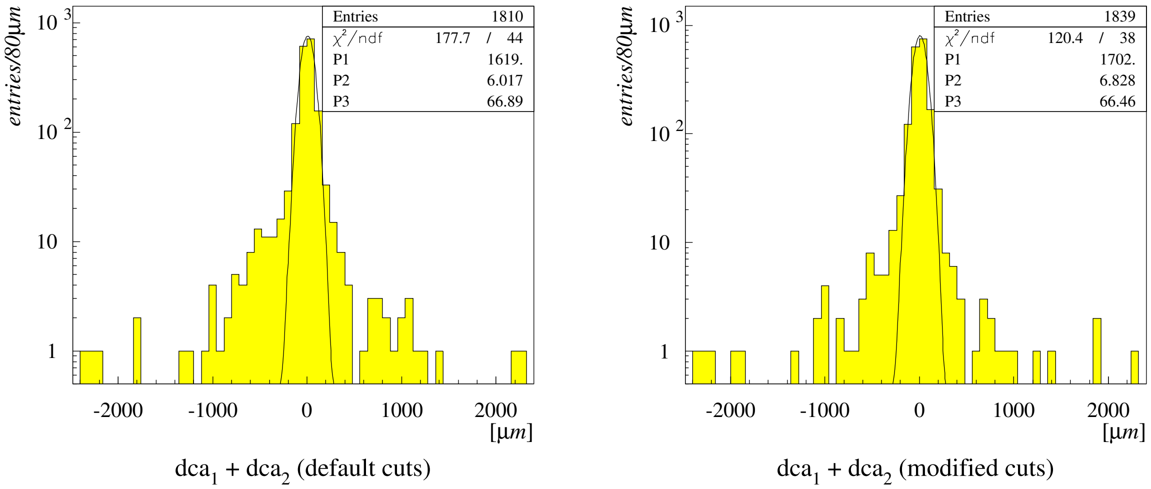

Figure 4.16: *Improvement of the p-side link-efficiency by raising the cluster significance cut. The histograms (log scale) show the dca-sum distributions of the CST fitted tracks with the default cuts for the linking (left) and with the modified cut values (right) with normalized Gaussians fitted to them.*

correctly linked hits from 97.3% to 98.1%.

The remaining inefficiency is due to *split clusters*, where a single cluster is divided by a dead strip or noise fluctuations. The cluster algorithm then calculates a wrong center of gravity which leads to wrong parameters in the track fit if the cluster is still linked, or to missing links. Simply allowing for a one-strip gap in a cluster (and thus merging cluster parts) however deteriorates the double track resolution of the vertex-detector.

A possible solution is either to exploit pulse-height or significance information to distinguish "integral" clusters from cluster parts that should be merged, or to postpone the decision until the linking step when information on the number and the density of tracks crossing a silicon sensor is available.

4.6.2 Fit in the R-z-plane

The track fit in R-z is a straight line fit in the S-z-plane, where S is the track's arc length in the transverse plane. In addition to the z-information of the CST spacepoints and the CJC hits, linked hits from the z-chambers are also taken into account.

The fit variables are z_0 and $\tan\lambda$ which is the slope of the track in the S-z-plane. It is related to the polar angle Θ in the H1-coordinate system by $\Theta = \arctan(1/\tan\lambda)$. The S-z-projection of the track helix is then given by

$$z_i = \tan\lambda \cdot S_i + z_0 \tag{4.13}$$

since the magnetic field along the z-direction is uniform (s. Fig. 4.17). Using a least squares method the following quantity is to be minimized:

$$\chi^2 = \sum_{i=1}^{n} w_i \cdot (z_i - (S_i \cdot \tan\lambda))^2 \tag{4.14}$$

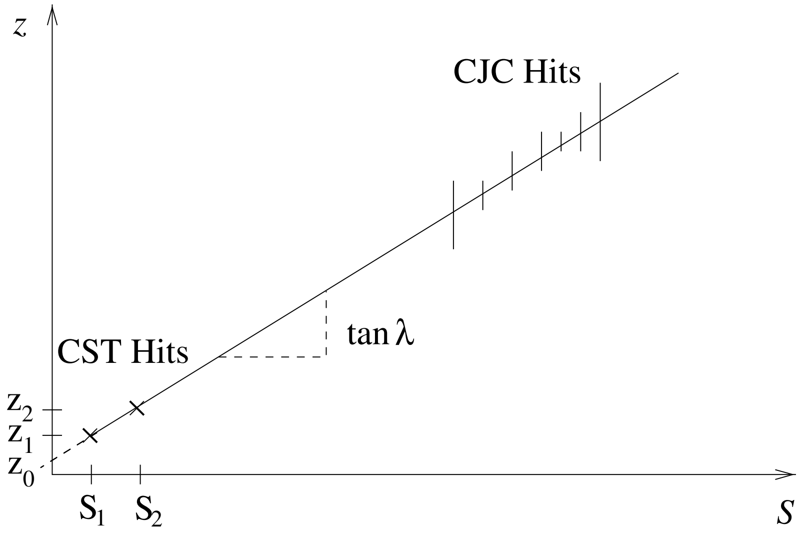

Figure 4.17: *Track fit parameters in the S–z-plane*

where (z_i, S_i) are z-position and track arc length of every z-hit entering the fit and w_i is the weight of the z-hit which is identified with the inverse of its uncertainty. Requiring the partial derivatives $\partial\chi^2/\partial z_0$ and $\partial\chi^2/\partial \tan\lambda$ to be zero, one obtains the normal equations:

$$A \begin{pmatrix} z_0 \\ \tan\lambda \end{pmatrix} = b \tag{4.15}$$

$$\text{where} \quad A = \begin{pmatrix} \sum w_i & \sum w_i \cdot S_i \\ \sum w_i \cdot S_i & \sum w_i \cdot S_i^2 \end{pmatrix} \quad \text{and} \quad b = \begin{pmatrix} \sum w_i \cdot z_i \\ \sum w_i \cdot z_i \cdot S_i \end{pmatrix}, \tag{4.16}$$

and the sums run again over all z-hits used. The parameters A_{ij} and b_i ("z-sums") determine the parameters $(z_0, \tan\lambda)$ as well as their covariance matrix (given as A^{-1}). For a linked CJC track, z-sums are available already if it was fitted to a primary or secondary vertex by the CJC reconstruction program.[8] This fit is analogous to the fit of the CST spacepoints to a track described here: the vertex position imposes a constraint on the track parameters which can be exploited to remove CJC hits that do not support the vertex fit. The z-sums then represent the contributions of the remaining CJC hits to the vertex fit. They are updated if a z-chamber hit is linked to the track.

Therefore, all the CST-R-z-fit has to do is to add the contribution of every linked CST spacepoint to the z-sums and solve Eq. (4.15) for $(z_0, \tan\lambda)$.

Considering the magnitudes of the uncertainties of CJC- and CST hits contributing to the z-sums, it is clear that the CST spacepoints dominate the fit completely: their errors are of the order of $50\,\mu$m whereas the CJC errors in z are of the order of centimeters. The larger radii of the CJC hits that result in larger arc lengths S_i cannot compensate for this difference in precision. For a given track the contribution of all CJC hits to the element A_{11}, the sum of the weights w_i, is ≈ 1, while a single CST hit adds $1/(5 \times 10^{-3})^2 = 40000$. The difference of the lever arms on the other hand is only a factor of the order of 10. Therefore the fit in R-z is highly sensitive to CST hits that have been assigned falsely.

---

[8] Since CSTREC uses the vertex-fitted tracks of the CJC for the linking, this is always the case for tracks considered for the CST–CJC fit.

For a track linked to one or more CST spacepoints, the first step of the z-fit is to obtain the z-sums from the CJC and eventually from the z-chambers. Next, the arc length S at the z-position of each of the spacepoints is calculated. The error on the z-coordinate measurement has already been calculated during the linking procedure from the intrinsic resolution and the polar angle Θ of the linked track. z, $1/\sigma(z)^2$, and S are the quantities needed for updating the z-sums. The new parameters for z_0 and Θ are stored in the CVFT bank.

Fig. 4.18 shows an event as reconstructed by the CJC alone and with the CST spacepoints used for the determination of the parameters. The improvement is even more striking than in the R-Φ-plane.

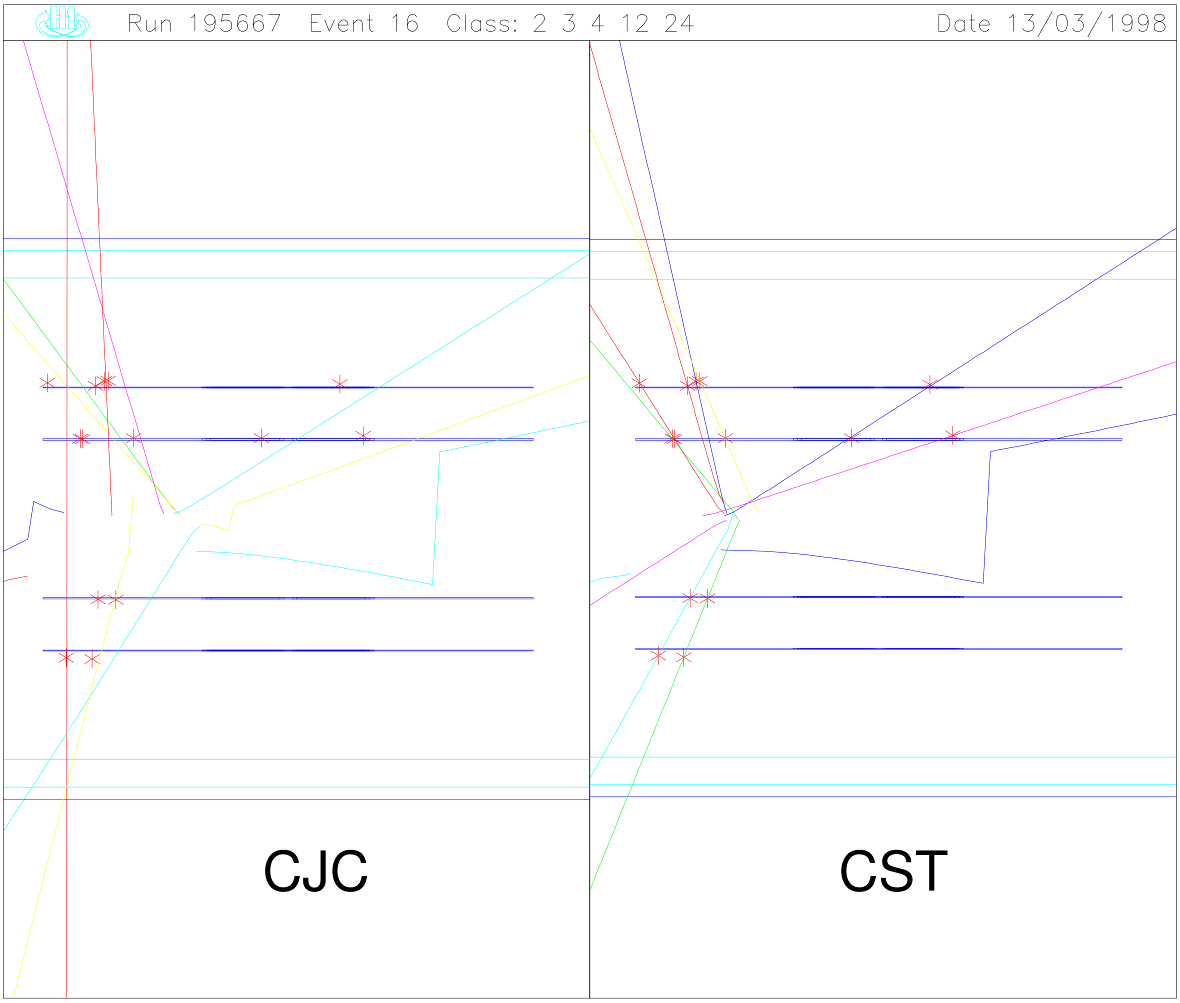

Figure 4.18: *R-z view of an event with CJC tracks (left) and CJC–CST fitted tracks (right)*

Quality of the R–z-track fit Again the parameters of cosmic tracks measured by the CJC alone and of CST–CJC fitted tracks are investigated, where the fitted tracks have exactly two linked CST hits. The tracks in the sample have a transverse momentum $p_t > 4\,\text{GeV}$. The conditions for the two track legs in the R–z-plane are:

$$\Theta_1 + \Theta_2 \stackrel{!}{=} \pi \tag{4.17}$$

$$z_{0_1} - z_{0_2} \stackrel{!}{=} 0 \tag{4.18}$$

The distributions of these two quantities (Fig. 4.19 and 4.20) show that the improvement with respect to the CJC tracks is large. Taking the width of the "signal" peaks of Fig. 4.20 (P6 for z_0, P4 for Θ)

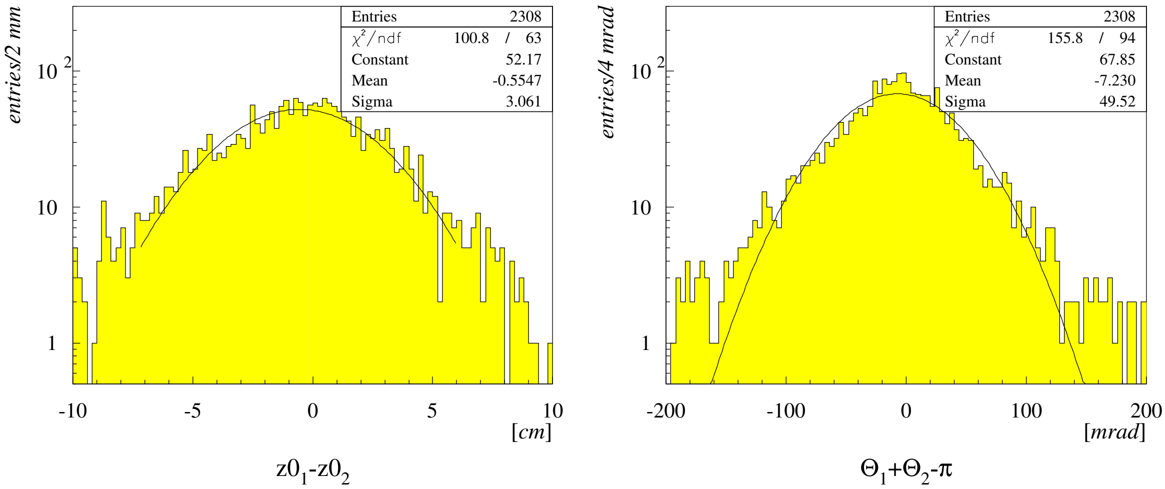

Figure 4.19: *Cosmic track parameters measured by the CJC in R-z (log scale). A simple Gaussian fit gives a z_0-resolution of 2 cm (left) and a Θ-resolution of 36 mrad (right).*

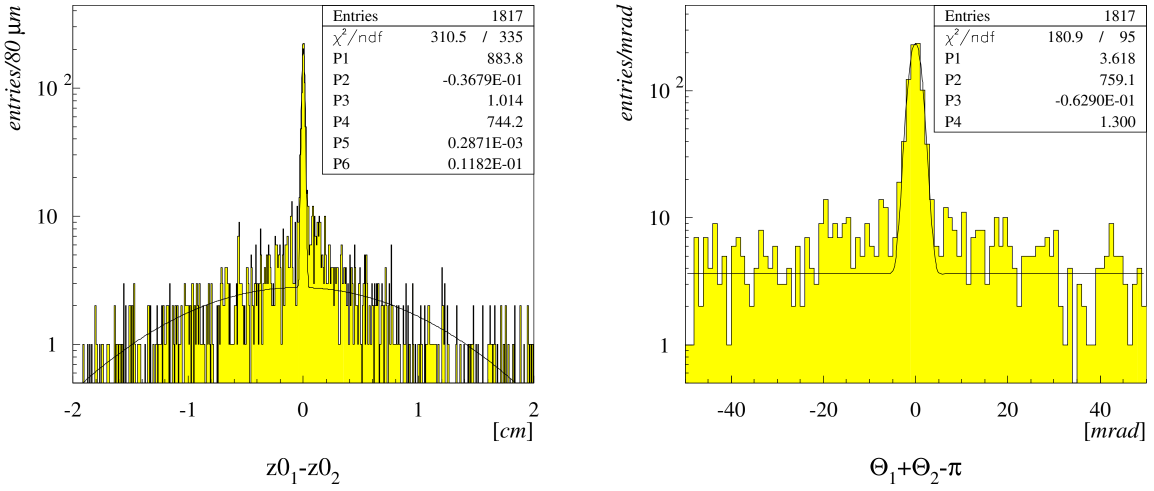

Figure 4.20: *Cosmic track parameters measured by the CST in R-z. Two normalized Gaussians (*P1-P3 *and* P4-P6*) have been fitted to the z_0-distribution (left) and a Gaussian (*P2-P4*) plus a constant term (*P1*) to the Θ-distribution (right).*

as a value for the track resolution, one obtains the following values for a single track (by applying a factor of $1/\sqrt{2}$):

$$\boxed{\begin{aligned}\sigma(\Theta) &= 0.9\,\text{mrad}\\ \sigma(z_0) &= 83\,\mu\text{m}\end{aligned}}$$

However, it is also visible that a non-negligible amount of wrong CST hits lead to a constant background. In the z_0-distribution, only 42% of the cosmic track pairs has a z_0-difference in the "signal" peak. Since each of the tracks has 2 linked CST-spacepoints, this is equivalent to a link efficiency of $\sqrt[4]{0.41} \approx 0.8$ for a single CST hit. It is clear that this value has to be improved, especially with regard to a reliable determination of vertices. Only a small part of the inefficiency ($\approx$3%) is due to the gaps in the active material along z.

Detailed studies with cosmic tracks have shown that another 8% of the inefficiency stems from missing hits. The remaining contribution from wrongly assigned spacepoints, where the correct hit is in fact present, is thus 9%. The primary goal for an improvement of the linking procedure is to save these links.

As mentioned in Chap. 4.5, the linking inefficiency in z is mainly due to the low signal-to-noise ratio on the n-side of the silicon sensors which makes a separation of signal and noise hits difficult (Fig. 4.4). From the cosmic studies, probability density functions for n-side clusters to be signal or noise have been obtained. For an individual cluster, a likelihood for the two cases can thus be calculated and be considered for the linking in addition to the z-residuum. Fig. 4.21 shows the parameters distributions obtained with this improved linking concept: The z_0-difference for 55% of the track pairs is now in the range of the "signal" peak, corresponding to a single hit linking efficiency of 86%. The contribution from wrong hits (while the correct one is present) has been reduced to 3%. For tracks traversing both CST layers further improvement is expected by additionally considering the residuals

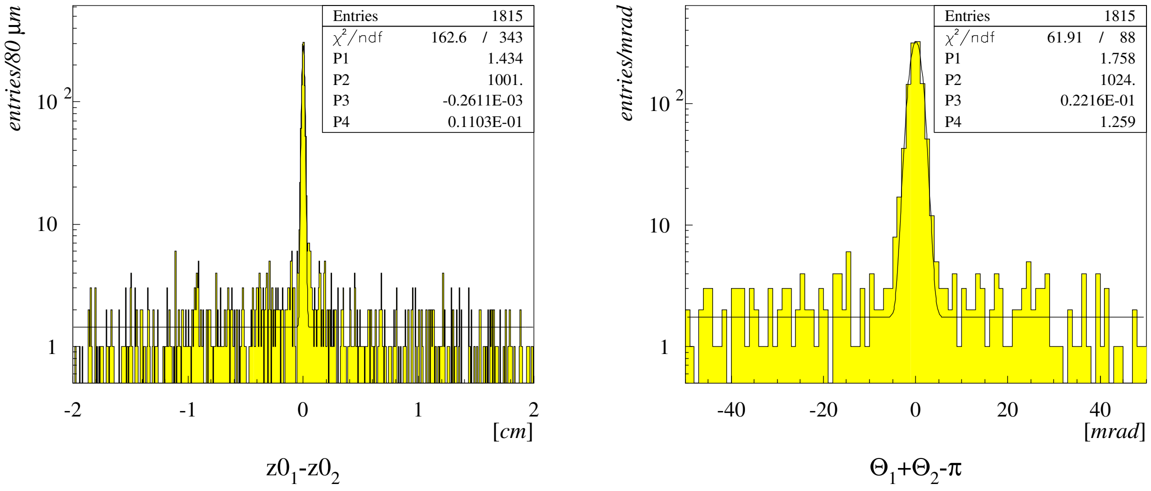

Figure 4.21: *Cosmic track parameters with the improved z-linking procedure. A normalized Gaussian plus a constant term has been fitted to both distributions.*

of the polar angle Θ_{CST} that is defined by the two linked CST hits with respect to the Θ-value from the CJC.

4.6.3 CST "forced" tracks

The combined CST–CJC track fit described in the previous sections processes all relevant track parameters and their errors in a mathematically well-defined manner. It works independently of the number of linked CST hits, in particular if the track traverses only one CST layer. On the other hand, it is potentially sensitive to inconsistencies and errors "inherited" from the CJC reconstruction.

In order to minimize the contribution of these influences, the CSTREC module produces another set of tracks: the "forced" CST tracks that have already been introduced for the alignment procedure (cf. Chap. 4.2). After the linking step, if CST hits in both layers have been assigned to a track, a helix track is calculated that passes exactly through the two spacepoints and has the curvature of the linked CJC track.

The input vector $(\kappa, x_1, y_1, z_1, x_2, y_2, z_2)$ (the index denotes the spacepoint of the inner and the outer CST layer, respectively) is transformed into $(\kappa, \Phi, \Theta, dca, z0)$ being the standard helix parameterization. The calculations are described in [34]. A covariance matrix is calculated by performing error propagation on the uncertainties of the input parameters that are assumed to be uncorrelated. Like for the fitted tracks, corrections describing energy loss and multiple scattering in the beam pipe are applied to the track parameters and their covariances. The tracks are stored in the track bank CVRT[9].

A comparison of these tracks with the equivalent tracks obtained by the constrained fit proves the resolutions to be comparable. Fig. 4.22 shows the parameter distributions for the cosmic track pairs as obtained with the forced tracks. Since the curvatures κ are taken from the linked, cosmic-fitted CJC tracks, they are exactly equal to each other (a result of the cosmic fit). Φ, dca, Θ, and z_0 can however be used to extract track resolutions. From the width of the peaks one obtains for the single-track-resolution:

$$\boxed{\begin{aligned} \sigma(\Phi) &= 0.73\,\mathrm{mrad} \\ \sigma(dca) &= 49\,\mu\mathrm{m} \\ \sigma(\Theta) &= 0.96\,\mathrm{mrad} \\ \sigma(z_0) &= 78\,\mu\mathrm{m} \end{aligned}}$$

The fact that these values are almost the same as the values for the fitted tracks indicates that the resolution of the latter is indeed deteriorated by some effect in the CJC reconstruction leading to wrong elements in the covariance matrix.

---

[9] **C**entral **V**ertex **R**adical **T**racks

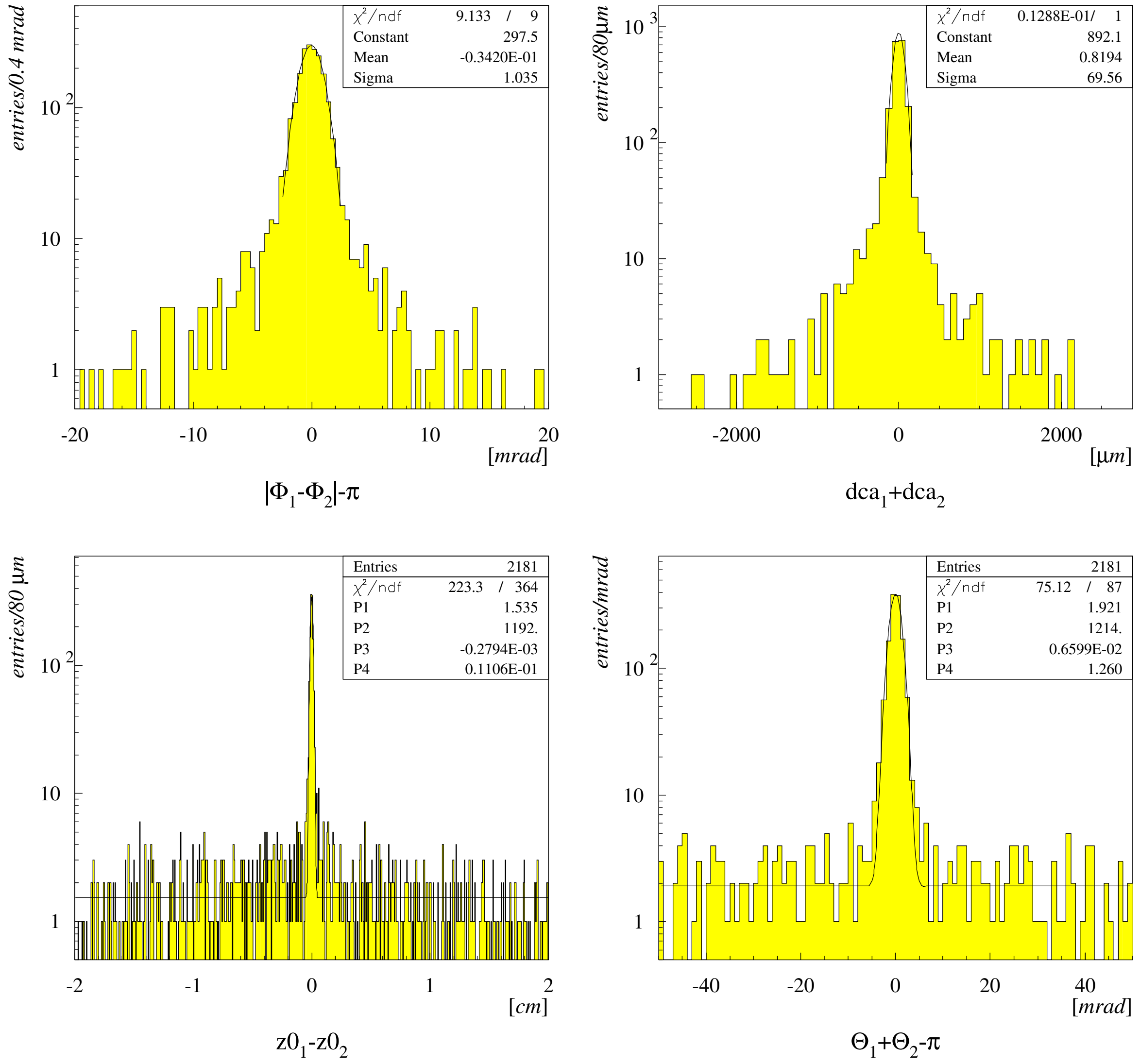

Figure 4.22: *Characteristic distributions for "forced" CST cosmic tracks. The distributions have to be compared to those of the fitted tracks (Fig. 4.14 and Fig. 4.21)*

4.7 Determination of run-vertex parameters

The precise determination of the primary and all subsequent vertices in an event is of major importance for all physics analyses. The position of the primary vertex is restricted to the area where the primary e–p-interaction takes place. This area is determined by the position and the extension of the colliding particle bunches. At HERA, the particle bunch extension is $\sigma_x \approx 180\,\mu$m in x-direction, $\sigma_y \approx 50\,\mu$m for y, and several centimeters for the z-component. Additionally, the beam axis (along the z-direction) is tilted with respect to the z-axis of the H1 detector. These parameters are however stable during one fill in the storage ring.

The extensions of the beams and thus the uncertainties on the primary interaction point have to be compared to the achievable resolutions when performing a vertex fit with tracks measured in an event: whereas the z-component can be determined for every event, the interaction area in R-Φ is small compared to the precision of the measured tracks when considering *CJC information alone*. The best measurement of the primary event vertex is hence a combination of the z-coordinate determined from tracks of the event with the parameters of the beam position and extension in x and y.

Therefore, the parameters for the beam position and the beam tilt with respect to the H1 coordinate system are being determined from tracks measured by the CJC in many events exploiting their stability. For every data acquisition run, the *run-vertex* parameters are stored:

- the x- and y-coordinates at $z = 0$: x_0 and y_0
- the slopes in x-z and y-z that parameterize the beam tilt: s_x and s_y

These quantities are determined on the L4 filter farm already, so that they can be used by the L5 reconstruction process. Here, the position of the primary vertex is calculated for every event by determining the z-coordinate z_{PV} first and then calculating the x- and y-coordinates by evaluating:

$$x_{PV} = x_0 + s_x \cdot z_{PV} \tag{4.19}$$

$$y_{PV} = y_0 + s_y \cdot z_{PV} \tag{4.20}$$

With this method, the uncertainties on x_{PV} and y_{PV} are dominated by the beam extensions since the errors on the run-vertex parameters are small due to the good statistics when averaging over many events.

With *additional CST measurements* however, the measured track resolution is sufficient to determine x- and y-coordinates of the vertex position from tracks for every event with a precision that is more accurate than the beam extensions. However, the run-vertex parameters still can be employed in this case, e.g. as start values for a vertex fit.

Therefore, the CSTREC software module determines the run-vertex parameters (x_0, y_0, s_x, s_y) on the basis of the CST fitted tracks in the same manner as the procedure with CJC tracks alone. The tracks stored in the CVFT bank (cf. Chap. 4.6.1) are pre-selected according to the following criteria:

transverse momentum:	$p_t > 300\,\text{MeV}$	no. of linked CST hits:	NLCST ≥ 2
polar angle:	$20° < \Theta < 160°$		
dca:	$\lvert dca \rvert < 5\,\text{cm}$	probability of the CST–CJC track fit in R-Φ:	$\mathcal{P}_{R-\Phi} > 0.3$

For an accepted track, the parameters $(\sin\Phi, \cos\Phi, dca, \sigma(dca), z0, weight)$ are stored, where *weight* is a function of the track length. After a predefined number of tracks (500) has been collected, mean values of the four run-vertex parameters are calculated. At run end, the mean values are then averaged and written to the database. The software for this task is also employed in other fields where run-dependent quantities are determined from data [64]. It is designed to run in multi-processor environments, which both the L4 filter farm and the L5 reconstruction machine are. An individual processor collects and stores the track parameters on its own. The calculated run-vertex parameters are merged and averaged at run end only.

Fig. 4.23 shows the distributions of the run-vertex position for the data acquisition runs taken in 1997. The shift of the beam position from the nominal axis towards positive values of x and y is visible. The

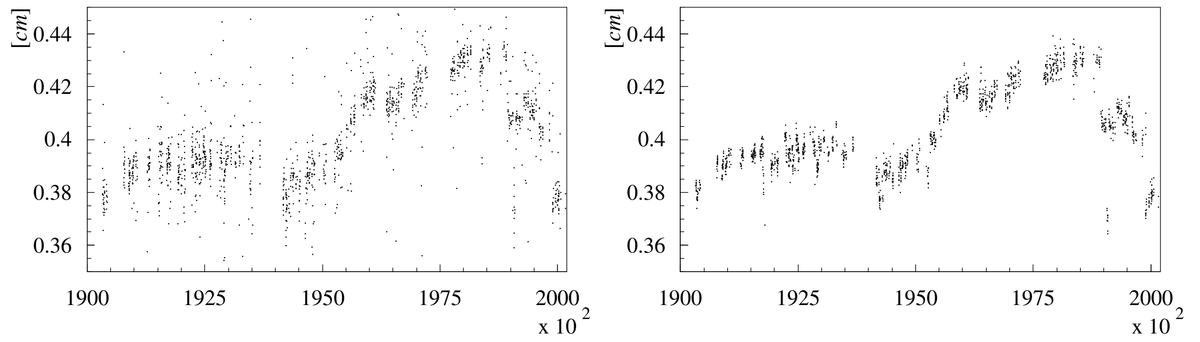

CJC run-vertex: x vs. run number

CST run-vertex: x vs. run number

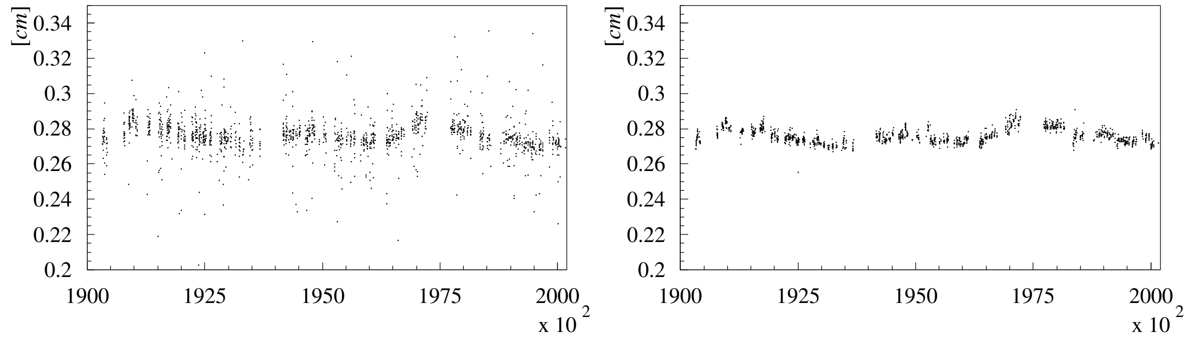

CJC run-vertex: y vs. run number

CST run-vertex: y vs. run number

Figure 4.23: *Distribution of the x- and y-coordinates of the run vertex for the data taking period 1997 determined by the CJC (left) and with CST tracks (right)*

distributions obtained from the determination with the CST tracks show smaller fluctuations from run to run. The outliers in the CJC values are due to poor statistics: the run has been too short to obtain precise values. The disappearance of these outliers when using CST tracks reflects the higher accuracy of the tracks used for the calculation. It is the reason that the CST needs fewer tracks and therefore reaches a stable result faster. This greater stability of the CST run-vertex could be exploited in changing the scheme of its determination: storing values no longer for each data acquisition run regardless its duration but rather using the errors on the values as a criterion for the quality of the run-vertex and store it if a certain level is reached. Longer runs would then have several entries for the run-vertex parameters.

4.8 Input and output data

Being a standard H1 reconstruction module, CSTREC is designed to operate in three domains:

1. online reconstruction on the L4 filter farm supporting the trigger decisions
2. final online reconstruction (L5) of the data taken
3. reconstruction of simulation data (the CST is included in the H1 detector simulation since 1998)

The software is identical for all three applications, the only particularity being a different input stage for the reconstruction of simulated events.

The simulation of an event in the CST tracks the generated particles traversing the detector and simulates the charge generation and the drift in the silicon towards the readout strips in detail. The final output of this simulation step are the strips that carry signal, which means that noise is not yet included (the bank is called CSTS). For this reason, CSTREC first adds randomly generated noise and then creates the cluster bank CVLH (cf. Chap. 4.3). All following reconstruction steps are then again identical to those of real data.

This means that at present, the effects of the cluster finding algorithm are not taken into account for simulated data. To make their treatment really consistent, the noise generation should be moved to the simulation step, preferably with quantities derived from real data, e.g. half-ladder dependent noise densities or a noisy/dead channel map. The output should then be of the same format as the output from the readout processors, so that the full reconstruction —including cluster algorithms— can be performed.

A special situation exists for the data that have been taken in 1997. For the online event reconstruction, only a part of the CSTREC module was available, namely the cluster reconstruction. The resulting output bank was the CVLH bank containing the parameterizations of the found clusters. Physical analyses of these data therefore have to include the CST reconstruction to have the improved track parameters available. As described in Chap. 2.2, analyses use a compressed subset of the full reconstructed data, the so-called DST banks. In 1997, the CVLH bank was therefore compressed and stored in the DST files (then called DVLH).

In order to allow CST information to be included in the analyses in a convenient way, CSTREC was designed to be able to process the compressed DST data of 1997 as well. In this case the cluster reconstruction is skipped, the cluster bank DVLH is decompressed instead and then the CST spacepoints are assembled. The additional information on the CJC tracks needed for the linking and the track fitting is read from different banks than in the default case but then used in the same manner. This feature makes it possible to run CSTREC as part of an analysis job without the need for a separate reconstruction step. The final output —the improved tracks— is then available for further evaluation.

The recognition of the different "modes of operation" (processing normal data, simulated data, or DST data) is entirely driven by the input data itself, i.e. depends on the banks present in the event. The decision step being the first routine to be executed by CSTREC for any event is sketched in Fig. 4.24. In any case, if CST input data have been found, the module produces banks containing track parameters that incorporate the CST measurements and whose entries are related to tracks measured in the CJC.

The *final reconstruction step* of the CSTREC module is however performed even if no CST data are available for an event. The purpose of this step is to provide a bank (named CSKR) with *all* non-

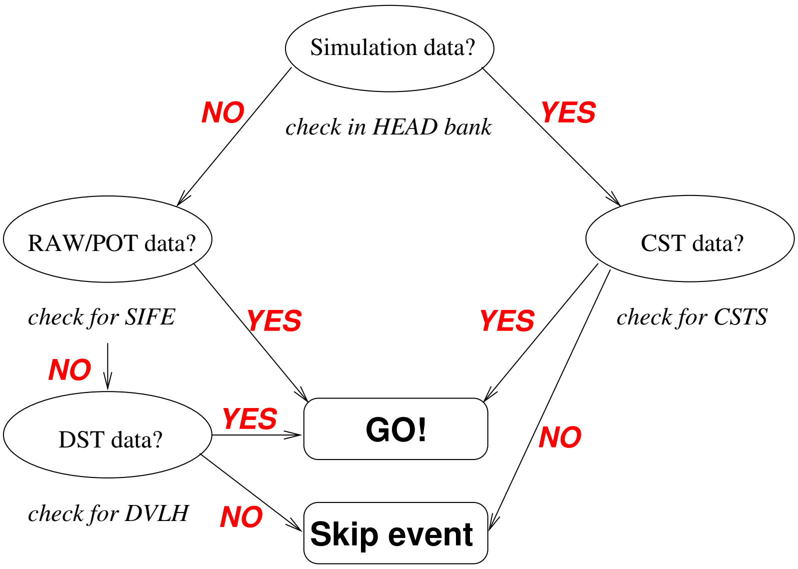

Figure 4.24: *CST input data banks to be checked before processing*

vertex-fitted central tracks with their best measured parameters. Due to the limited acceptance of the CST, only a part of the central tracks will be improved by the CJC–CST fit. If this is the case, the parameters stored in the CVFT bank are copied to the final track bank.

If a track has not been measured by the CST, the parameters as measured by the CJC are taken and corrected for energy loss and multiple scattering. The parameters are modified further, if z-sums have been calculated by the CJC reconstruction program.[10] Then, new values for Θ and $z0$ are calculated. In doing so, contributions from the z-chambers are also taken into account, if present.

---

[10] This is equivalent to the CJC track having been fitted to a vertex, cf. Chap. 4.6.2.

Chapter 5

Semi-muonic decays of heavy mesons

With the ability of the CST to measure tracks with a resolution of the order of $100\,\mu$m, its most prominent field of application is the study of heavy quarks. The reason is the long life time of hadrons containing a b- or a c-quark of typically $\sim 10^{-12}\,$s that results in a sizeable separation of the production- and the decay vertex of the heavy quark. Tab. 5.1 shows the decay lengths of heavy flavoured mesons. In order to measure the decay of a heavy meson, its production and decay vertices thus have to be determined with an accuracy that is sufficient to resolve the decay length. This means that the track of a decay product of the heavy meson has to be separated significantly from its production vertex. At H1, the resolution of the primary vertex is currently determined by the beamspot size of $\sigma_x \approx 180\,\mu$m and $\sigma_y \approx 50\,\mu$m, as explained in Chap. 4.7. Considering in addition the uncertainties of a track of a decay particle as determined by the CJC alone which are of the order of 150–250$\,\mu$m in x-and y-direction, it is clear that without CST information, the decay length of heavy mesons cannot be resolved. As shown in Chap. 4.6.1, the CST is capable of reducing the track errors by a factor of 2/3 to $\approx 50\,\mu$m in the R-Φ-plane, so that the combined track-vertex-resolution is smaller than the decay length of the B-mesons and might even be sufficient to resolve the decay length of $D^{\pm}$-mesons.

	mass [MeV]	$c\tau$ [μm]
$D^{\pm}$	1869.3 ± 0.5	317
D^0	1864.5 ± 0.5	124.4
$D_s^{\pm}$	1968.5 ± 0.6	140
$B^{\pm}$	5278.9 ± 1.8	462
B^0	5279.2 ± 1.8	468

Table 5.1: *Masses and decay lengths of heavy mesons*

For this reason, an explorative study has been carried out in order to demonstrate that the improved track resolution obtained with the CST does indeed allow to tag heavy quark decays. It has been focussed on the *semi-leptonic* decay channels of the heavy quarks, in particular on the modes with a muon in the final state. The latter are preferable to electrons or positrons since muons are measured in a dedicated part of the H1-detector where the background due to misidentified hadrons is smaller.

The study relies on the measurement of a muon in the central region of the iron barrel detector which is linked to a track in the central tracking devices and the CST. The data sample (s. Chap. 5.3) was selected to be enriched in b-quarks in order to benefit from their comparably large decay length. The impact parameter method (introduced in Chap. 5.2) was chosen for the investigation of the decay lengths. In comparison, a minimum bias data sample which is not enriched in muon content but fulfills the same selection criteria was investigated (Chap. 5.3.2).

In addition, studies on simulated data have been performed for samples containing $c\bar{c}$- and $b\bar{b}$-events respectively. For this purpose, the simulation program for the detector response of the CST was employed for the first time. The resulting distributions are compared to the ones obtained from data.

Thorough analyses of the semi-muonic decays of b-quarks in the H1-detector have been performed in [8] and [23].

5.1 Monte Carlo studies

The properties of the decay of heavy mesons have been studied with Monte Carlo (MC) data samples. The Monte Carlo generator AROMA [65] has been used to simulate the production of a $c\bar{c}$- or a $b\bar{b}$-pair and the subsequent semi-muonic decay of one of the quarks.

The AROMA generator simulates the production of heavy quarks in electron-proton scattering via the boson-gluon fusion process. In leading order $O(\alpha^2 \cdot \alpha_s)$ photoproduction as well as deep inelastic scattering contributions are calculated taking into account all electroweak processes and considering the quark masses ($m_b = 5\,\mathrm{GeV}/c^2$, $m_c = 1.5\,\mathrm{GeV}/c^2$). Higher-order effects are accounted for by means of correction factors for the differential cross-section. This treatment results in a good agreement of the generator predictions for the inclusive quark distributions with NLO calculations.

The generated partons then undergo fragmentation processes. This step is implemented in a separate program package (JETSET [66]). Since fragmentation processes are long range interactions and cannot be described in the framework of perturbative QCD calculations, phenomenological models have to be applied. In AROMA, different models can be chosen, the standard being the Lund string fragmentation model.

The resulting output are the four-momenta and the identities of all the particles involved. In the next step, the detector response is simulated using a program based on the GEANT package [67]. This step is completed with the *digitization* stage, where the signals of all detector components in the same form as the ones in real *ep* data are obtained. These signals are processed further using the same reconstruction programs as for real data. The same analysis steps as for real data can be used subsequently.

For the two samples with $c\bar{c}$- and $b\bar{b}$-pairs, a cut on the transverse momentum of the decay muon of $p_t > 2\,\mathrm{GeV}$ has been applied already on the generator level. The simulation and reconstruction has been performed only for events passing this generator cut. Tab. 5.2 shows the characteristic quantities of the Monte Carlo samples. In the following, some properties of events containing heavy quarks will be introduced by exploiting the *generated* quantities.

Kinematic distributions of the generated events

Some kinematic distributions for both the generated $c\bar{c}$- and the $b\bar{b}$-events are shown in Fig. 5.1. The range of the virtuality Q^2 was not restricted, thus both photoproduction and DIS events are contained in the samples. In the distribution of the quark-antiquark center-of-mass energy $\hat{s}$ the production

	$c\bar{c}$	$b\bar{b}$
σ_{ep} [nb]	606.68	3.13
$\int \mathcal{L}dt$ [pb^{-1}]	10.78	47.62
generated events	6600000	150000
events passing generator cut: $p_t(\mu) > 2\,\mathrm{GeV}$	7011	4860
events with decay muon measured in the CST	2674	1931

Table 5.2: *Parameters of the employed Monte Carlo samples. The number of events measured in the CST is determined after digitization and reconstruction.*

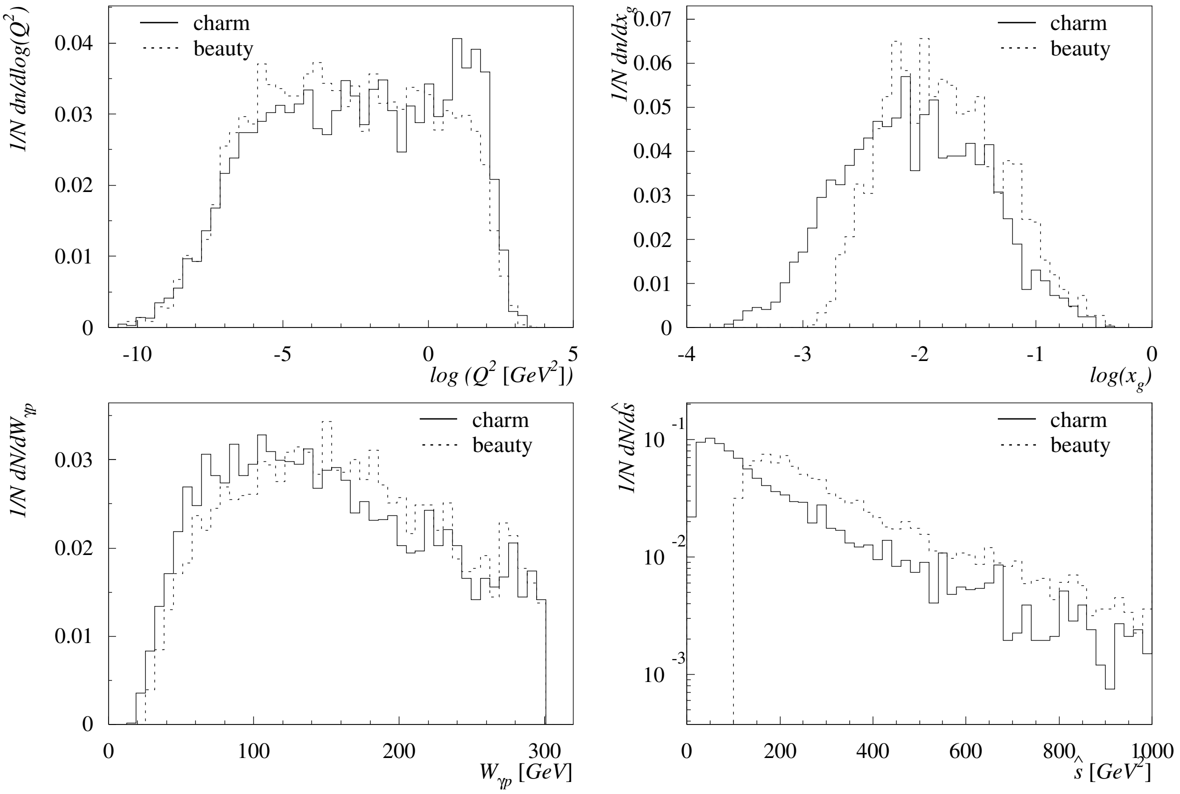

Figure 5.1: *Kinematic distributions for events generated by* AROMA *(each normalized to 1)*

threshold for beauty quark pairs of $\hat{s} = 100\,\mathrm{GeV}^2$ is clearly visible. The photon-proton center-of-mass-energy $W_{\gamma p}$ is on average slightly higher for $b\bar{b}$-production than for $c\bar{c}$-production. The same is true for the momentum fraction x_g of the interacting gluon.

Fig. 5.2 shows the transverse momentum spectrum and the polar angle distribution for the decay muon of the generated heavy quark. The p_t-spectrum for muons from b-decays is harder due to the higher b-quark mass. Also, the b-muons tend to be emitted at lower polar angles: their boost in proton direction is larger.

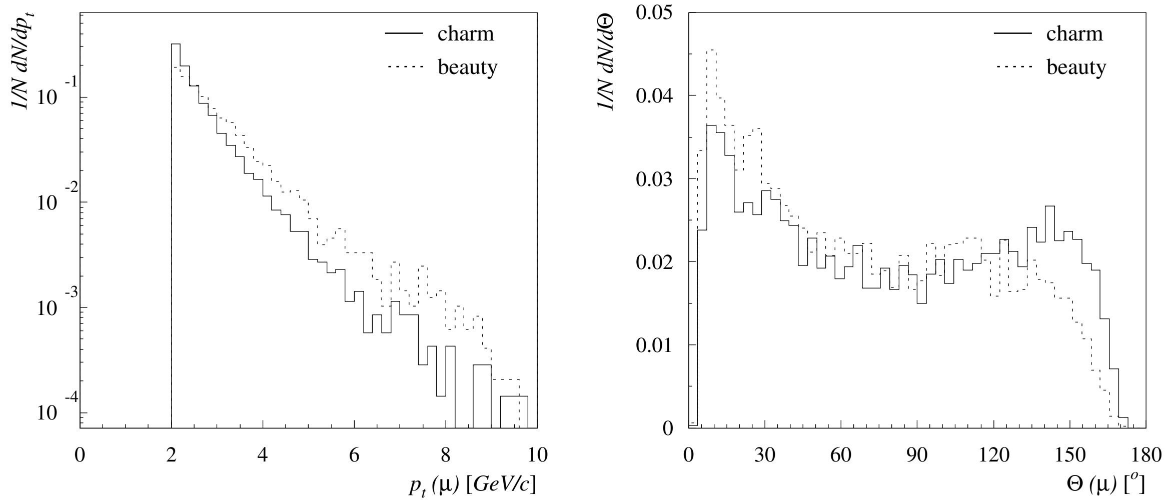

Figure 5.2: *Kinematic distributions for the generated muons*

The effect of requiring the decay muon to be measured in the CST is sketched in Fig. 5.3. This condition presupposes the reconstruction of the muon track in the CJC and its linking and fitting to hits in the CST as well as the measurement of the muon in the iron detector. The selection steps are described in Chap. 5.3. Requiring a CST measurement of the muon is equivalent to restricting the polar angle range (the nominal acceptance of the CST is $30^\circ < \Theta < 150^\circ$). Therefore, events with small values of $W_{\gamma p}$ are rejected. The spectrum of the quark-antiquark center-of-mass energy $\hat{s}$ is however not distorted but just scaled. The same holds for the p_t-distributions for both b- and c-quark decay muons that keep their shapes when requiring a CST measurement.

Heavy meson decays

About 90% of the heavy quarks fragment into mesons. In $c\bar{c}$-events for instance, the production fraction of D^0- mesons is $\approx$ 60%, for $D^\pm \approx$ 24%, and for $D_s \approx$ 10% [68, 69]. Most of the decay muons hence originate from heavy mesons whose properties are studied in more detail here. The quantities shown are for mesons whose decay muon has been reconstructed in the CST and are in general restricted to the R-Φ-plane.

Fig. 5.4 shows the projections of the *generated* decay lengths onto the transverse plane ($\equiv l^{R\Phi}_{decay}$). Six heavy mesons have been considered. The probability that a particle of mass m and momentum p

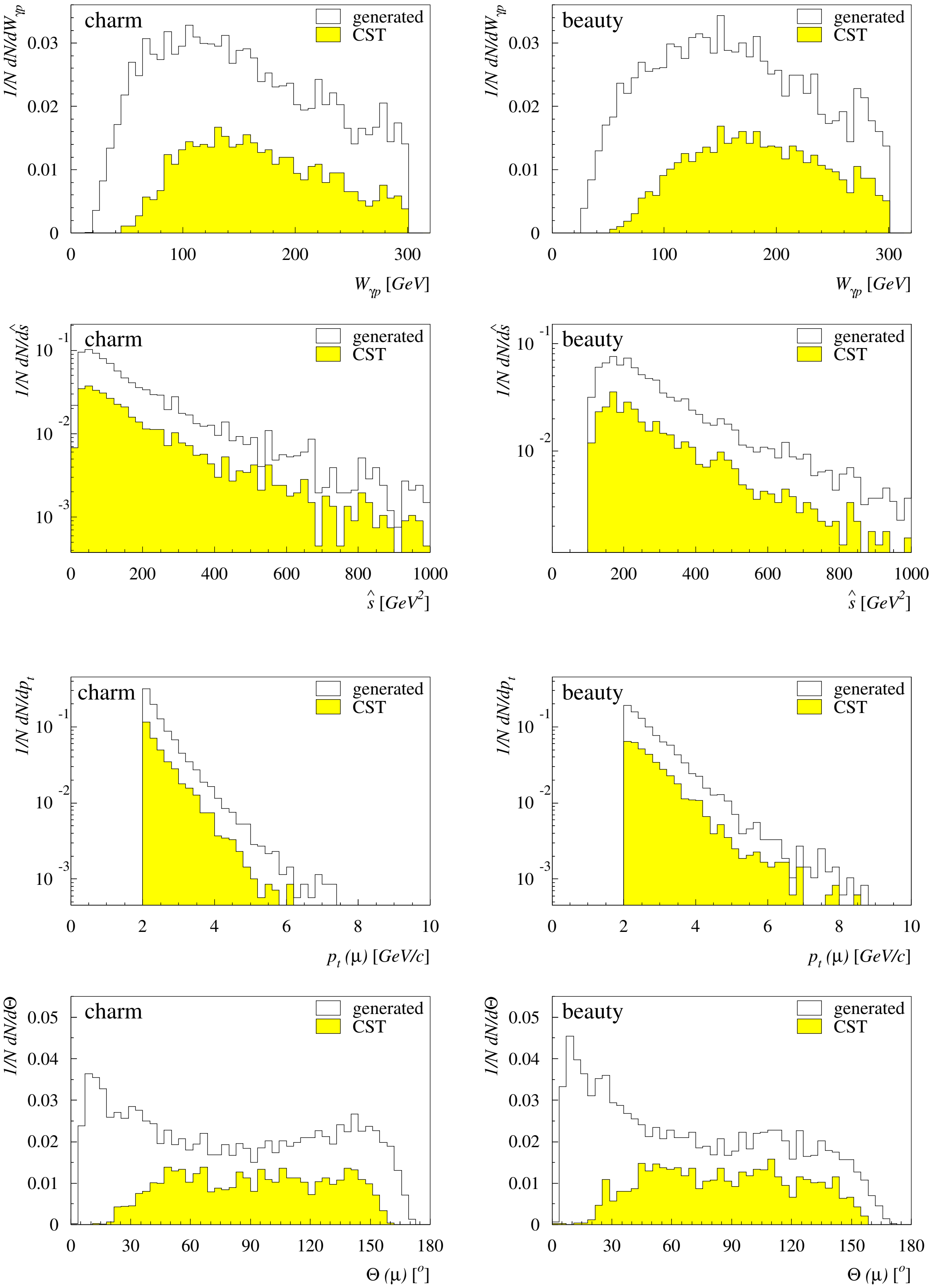

Figure 5.3: *Kinematic distributions for all generated muon events and for those measured in the CST: charm (left) and beauty (right)*

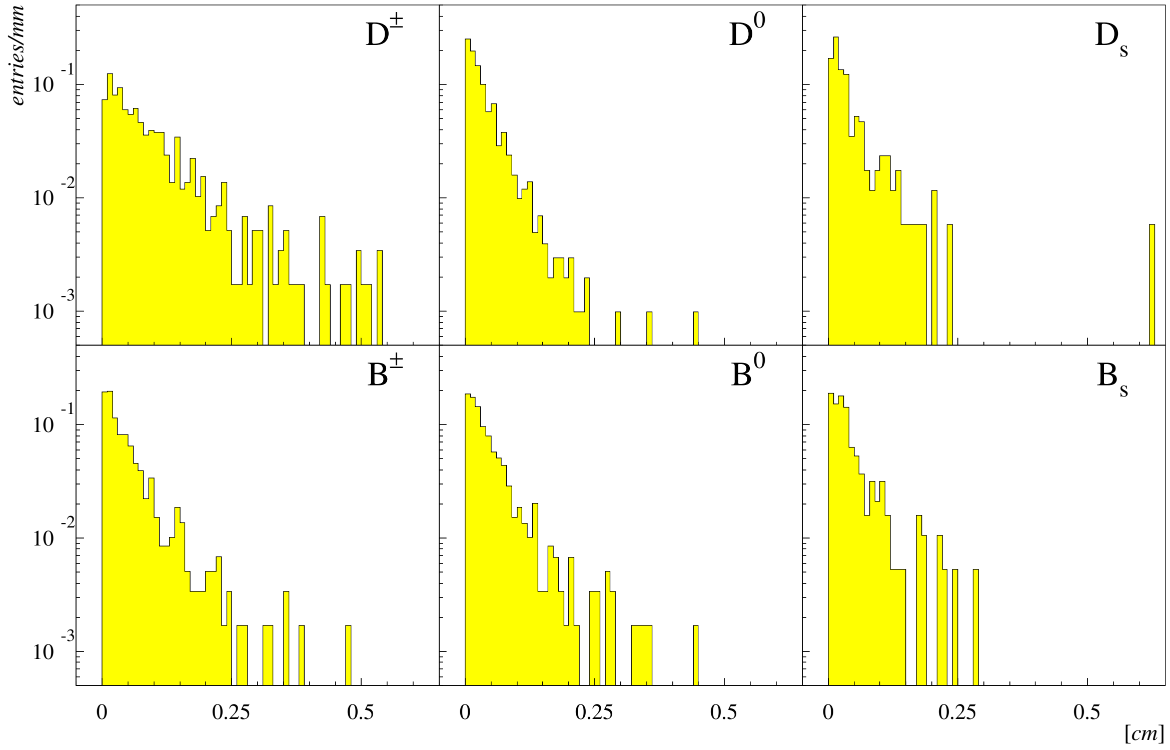

Figure 5.4: *Transverse decay lengths* $l_{decay}^{R\Phi}$ *for the heavy mesons as generated by* AROMA *(histograms normalized to 1)*

travels the distance l before decaying is given by

$$\mathcal{P}(l) = \exp(-\frac{m \cdot l}{|p|} \cdot \frac{1}{\tau}) \tag{5.1}$$

From the distributions of the transverse decay length one can therefore retrieve the mean decay length $c\tau$ by taking into account the transverse momentum of the heavy meson and its mass. By means of fitting the distributions of the considered mesons one obtains:

$D^\pm$:	308 ± 37	μm	$B^\pm$:	514 ± 40	μm
D^0 :	123 ± 6	μm	B^0 :	447 ± 36	μm
D_s :	317 ± 150	μm			

The errors are due to the limited statistics of the Monte Carlo samples. The Monte Carlo generator hence describes the decay properties of the heavy mesons correctly.

The transverse momentum spectra (with respect to the z-axis: Fig. 5.5) show a sharper edge at low momenta for the charmed particles. This is a consequence of the higher mass of the B-meson: in order to produce a muon with $p_t > 2\,\text{GeV}$, the D-meson has to have a higher momentum than the B.

Another effect which is due to the mass difference of the heavy quarks is the difference of the distributions for the decay angle α in the R-Φ-plane between heavy meson and muon (Fig. 5.6, left). A muon from a charmed meson tends to be emitted at low angles with respect to the meson flight direction while the distribution for muons from B-mesons extends to large values of α. Finally, the

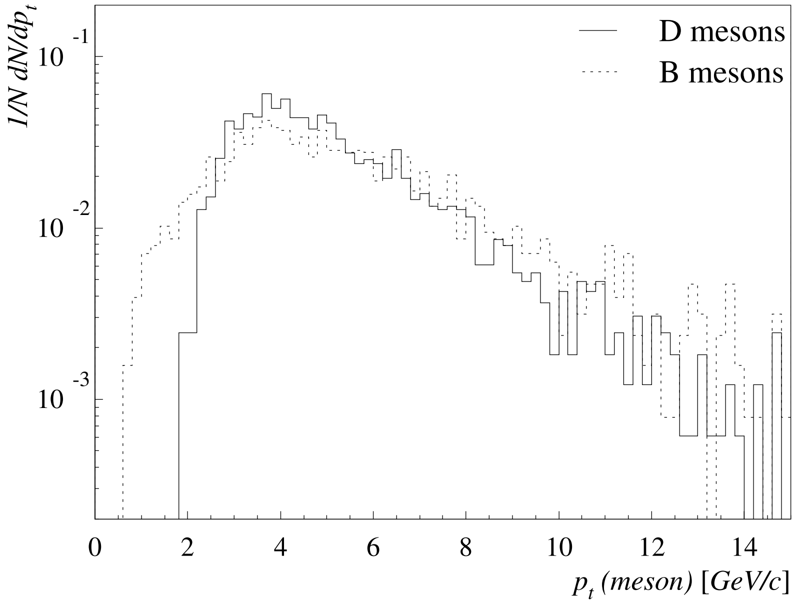

Figure 5.5: *Transverse momenta of the heavy mesons with respect to the z-axis*

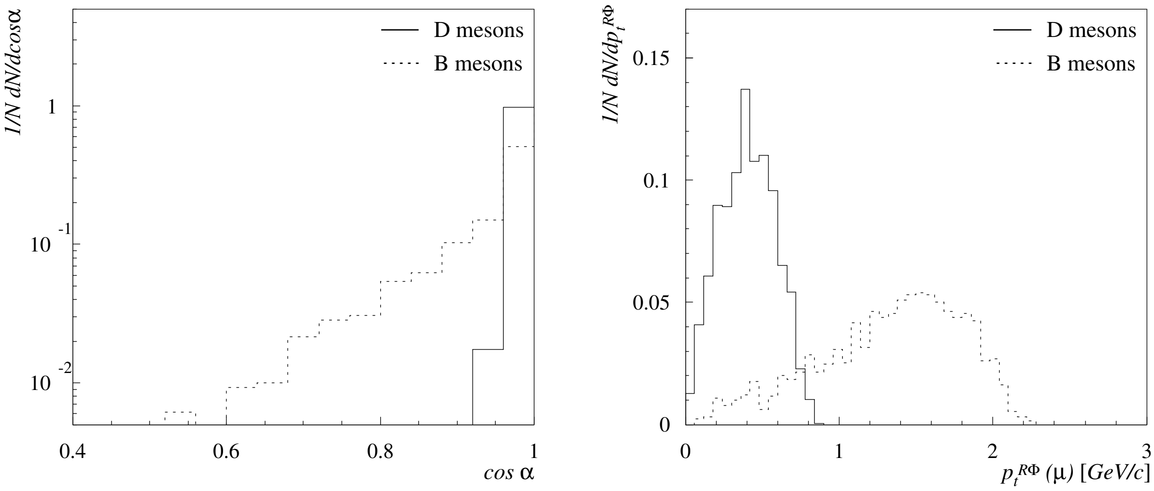

Figure 5.6: *Decay angle α in the R-Φ-plane between muon and heavy meson (left) and relative transverse momentum of the muon with respect to the heavy meson (right)*

distributions of the relative transverse momentum of the decay muon *with respect to the heavy meson direction* ($p_t^{R\Phi}(\mu)$: Fig. 5.6, right) show a harder scale for muons originating from B-mesons which is again a consequence of their higher mass.

The quantities α and $p_t^{R\Phi}$ are thus qualified for a separation of $c\bar{c}$- and $b\bar{b}$-events. However, the flight direction of the heavy meson is of course not accessible directly in the reconstruction of data. It is therefore approximated by suitable quantities which will be introduced in Chap. 5.3.

5.2 Impact parameter method

For the lifetime measurements of heavy quarks, two standard methods are commonly applied:

1. the vertex method: primary ($\equiv$ production-) and secondary ($\equiv$ decay-) vertex are reconstructed from the charged tracks. The distance between the vertices is the decay length l_{decay} which is related to the lifetime τ:

   $$l_{decay} = \beta\gamma c\tau \tag{5.2}$$

   A necessary condition for applying this method is that at least two charged particles are created at both the primary and the secondary vertex to allow the vertex reconstruction. Moreover, the accuracy of the determination of primary as well as secondary vertex has to be sufficient to resolve typical decay lengths of heavy mesons of the order of $100\,\mu$m. The method hence depends strongly on the momentum of the decaying particle.

2. the impact parameter method: the impact parameter is the orthogonally closest distance between a particle track and the primary vertex and thus carries information on the particle originating from the vertex or not. The impact parameter δ of e.g. a muon from a heavy quark decay is related to the decay length as

   $$\delta = l_{decay} \cdot \sin\Theta \cdot \sin\alpha \quad , \tag{5.3}$$

   where Θ is the polar angle of the decaying hadron and α is the angle between the direction of the hadron and the direction of the muon in the R-Φ-plane (s. Fig. 5.8). An example for the application of the method is the measurement of the B hadron life time at LEP [70, 71].

Two advantages of the impact parameter method are the but weak dependence of δ on the momentum of the decaying hadron and the fact that the decay vertex does not have to be reconstructed. The former fact can be made plausible by considering the decay topology with the assumption of a decay of a hadron with mass m_{had} and momentum $p_{had} = \beta\gamma m_{had}$ into a muon. For simplicity, let the decay happen in the R-Φ-plane, i.e. $\sin\Theta = 1$. Then

$$\tan\alpha = \frac{p_\perp(\mu)}{p_\parallel(\mu)} \tag{5.4}$$

is the decay angle in the laboratory system expressed by the momentum components of the muon orthogonal and parallel to the decaying hadron. With $p_\perp^*$, $p_\parallel^*$, E^* being the momentum components and the energy of the muon in the hadron rest frame, the following relations hold:

$$p_\perp = p_\perp^*$$

$$p_{\parallel} \;=\; \gamma(p_{\perp}^{*} + \beta E^{*})$$

Since $\tan\alpha \approx \sin\alpha$ for small decay angles and since $\beta \approx 1$ it follows that

$$\sin\alpha \sim \gamma^{-1} \sim p_{had}^{-1} \;, \tag{5.5}$$

i.e. for the impact parameter δ the p_{had}-dependences in l_{decay} and $\sin\alpha$ nearly cancel resulting in a weak dependence of the impact parameter on the momentum of the decaying hadron [72].

Fig. 5.7 shows the impact parameter δ_{gen} on the generator level calculated according to Eq. (5.3). The mean values of the δ_{gen}-distributions for $c\bar{c}$ and $b\bar{b}$ decay muons are 80 and 140μm respectively.

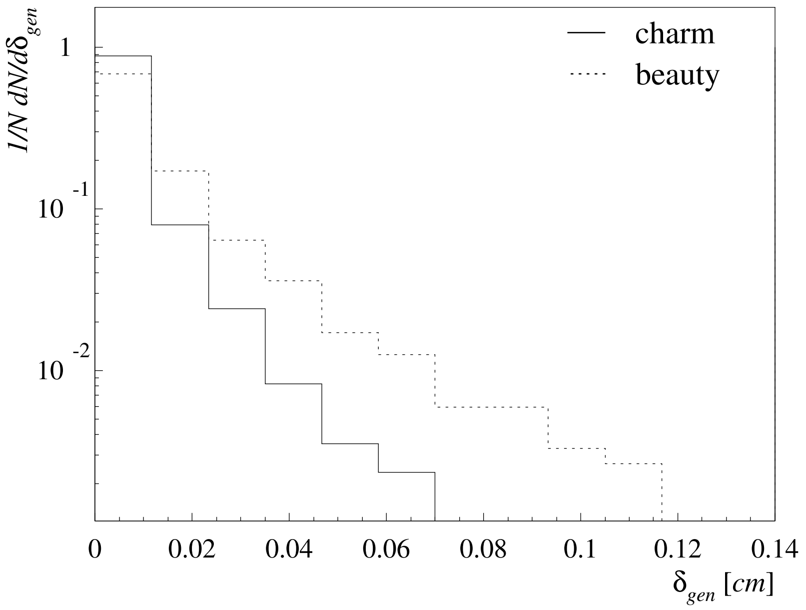

Figure 5.7: *Impact parameter of the decay muon as generated by* AROMA

Due to the precision of the measurement and due to the background, the *measured* values of the impact parameter will however be smaller. The principle of the measurement of the impact parameter in the R-Φ-plane is sketched in Fig. 5.8. Since the flight direction of the heavy meson cannot be measured directly, it is approximated by the thrust axis of the event hemisphere (s. below). The production vertex is assumed to be identical to the nominal beam position. The determination of the impact parameter and the resulting uncertainties are described in the next sections.

5.2.1 Determination of the impact parameter

For the determination of the impact parameter δ three input quantities are used:

1. the nominal beam position
2. the parameters of the muon track
3. the thrust axis calculated in the muon hemisphere of the event.

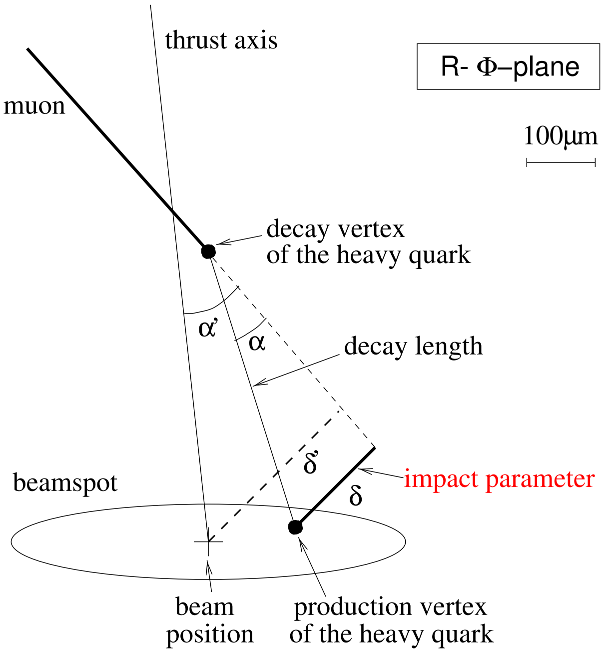

Figure 5.8: *Impact parameter method. The heavy meson is produced at the primary vertex within the beamspot. It decays semi-leptonically into a muon with angle* α *and impact parameter* δ*. In the measurement, the flight direction of the heavy meson is approximated by the thrust axis, and the primary vertex by the nominal beam position resulting in the quantities* α' *and* δ' [1].

The nominal beam position is calculated using the run-vertex parameters which are determined by CSTREC for all runs in 1997 (cf. Chap. 4.7). The z-value of the vertex is taken from the CJC primary vertex fit for every event. The x- and y-position of the vertex for a particular event depends on the z-position and is given by:

$$x = x_{RV} + z_{V_{CJC}} \cdot sx_{RV} \tag{5.6}$$

$$y = y_{RV} + z_{V_{CJC}} \cdot sy_{RV} \tag{5.7}$$

where the index RV denotes the values for beam position and slope versus z taken from the run-vertex. The uncertainty on x and y is calculated using error propagation and taking into account the size of the beamspot.

The absolute value of the impact parameter is then obtained by calculating the closest approach of the muon track with respect to the nominal beam position (using the track parameters dca and Φ):

$$dca' = dca - x \cdot \sin\Phi + y \cdot \cos\Phi \tag{5.8}$$

This quantity still follows the sign convention for the *dca* (cf. Chap. 2.3). The sign of the impact parameter is determined by calculating the intersection of the muon track with the *thrust axis*. Due to the finite precision of the involved quantities, namely of run-vertex and track parameters and in particular of the thrust axis, it can happen that the intersection is in the backward direction. In this case, the impact-parameter gets a negative sign (Fig. 5.9). From Fig. 5.8 it can be seen that for small

---

[1] For convenience, only the variable names α and δ will be used in the following. Where appropriate, it is explicitly stated whether they refer to reconstructed or to ideal quantities.

$\delta' > 0$ $\delta' < 0$

Figure 5.9: *Sign convention for the impact parameter*

angles α' between the muon track and the thrust axis the probability of reconstructing a negative impact parameter increases. A cut on this angle helps to reduce this fraction.

Thrust axis The definition of the thrust axis requires the sum of all longitudinal momentum components with respect to this axis to be maximal. The scalar quantity *thrust* is then defined as:

$$T = \frac{\sum_i |\vec{n}_T \cdot \vec{p}_i|}{\sum_i |\vec{p}_i|} \tag{5.9}$$

where $\vec{n}_T$ is the unit vector of the thrust axis and the sums run over all particles in an event. T is 0.5 for an isotropic momentum distribution and rises to 1.0 for collinear events. In this study, a slightly modified definition has been adapted. The calculation has been restricted to the R-Φ-plane and to the *hemisphere* defined by the muon momentum vector, that is the half-plane defined by the condition $\Phi - 90° < \Phi(\mu) < \Phi + 90°$. The introduction of hemispheres utilizes the fact that for events where a heavy quark pair is produced the transverse momenta seen in the detector are balanced. Taking the muon from the decay of one of the heavy quarks as a reference axis for the hemispheres is justified since the muon describes the original direction of the quark within a margin of $\Delta\Phi \approx 10°$ for c-quark decays and $\approx 20°$ for b-quarks as can be seen from M.C. data (Fig. 5.10, dotted histograms).

The hemisphere then also contains the particles produced in the hadronization process of the decaying heavy meson. The calculation of the thrust vector takes into account tracks and calorimeter cell information belonging to the hemisphere *except* the muon itself. In order to avoid double counting of energy depositions, only those cells are taken into account that are significantly separated from a track extrapolated to the calorimeter region. Fig. 5.10 also shows the opening angles $\Delta\Phi$ between the generated flight direction of the heavy quark and the reconstructed thrust axis. For c-quarks, the quark direction is approximated to an accuracy of $\approx 15°$, while for b-quarks, the accuracy is comparable to the one obtained from the muon direction ($\approx 20°$).

The impact of approximating the flight direction of the heavy quark by the thrust axis is shown in Fig. 5.11 for the $\cos\alpha$- and the $p_t^{R\Phi}$-distributions. The histograms have to be compared to Fig. 5.6, where the original generator information for the flight direction of the heavy quark has been used.

Unlike on the generator level, a clear separation of c- and b-quark decay muons is no longer possible since the distributions are smeared. However, the mean value of $p_t^{R\Phi}$ is still lower for muons from charm decays, and the distribution falls more steeply towards higher values of $p_t^{R\Phi}$ than the one for b-quark decay muons. The mean decay angle α is still smaller for the c-quark decay muons.

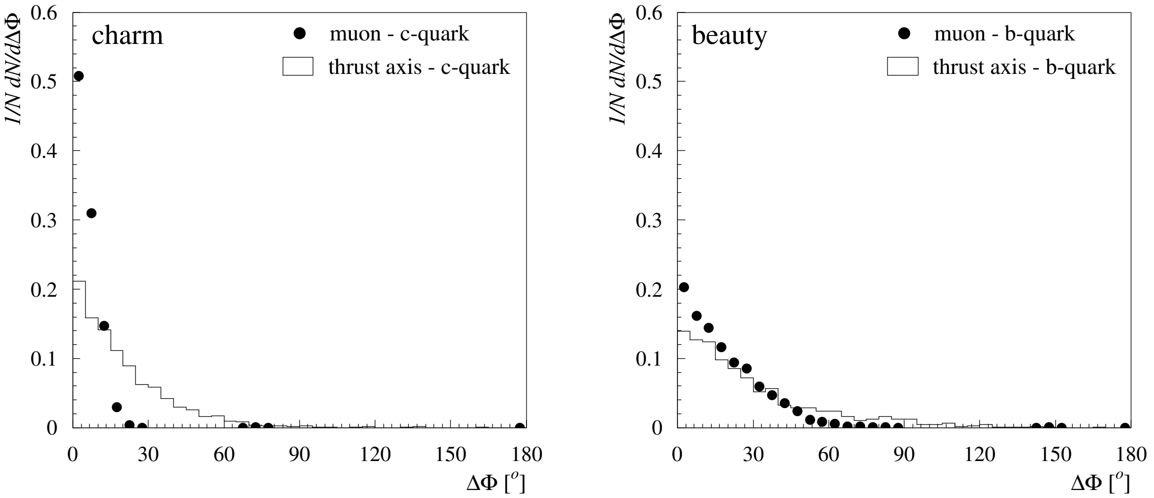

Figure 5.10: *Opening angle (in the R-Φ-plane) between generated heavy quark direction and reconstructed muon (dots) and reconstructed thrust axis (histograms) for $c\bar{c}$- (left) and $b\bar{b}$-events (right).*

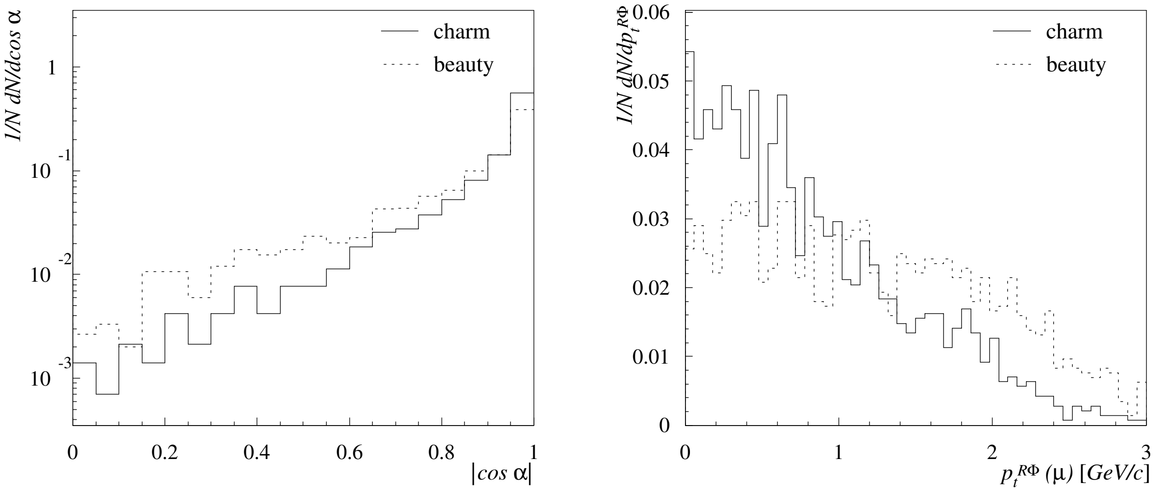

Figure 5.11: *Distributions for the generated muon parameters with respect to the reconstructed thrust axis. Left: decay angle α, right: relative transverse momentum $p_t^{R\Phi}$*

5.2.2 Uncertainties on the impact parameter

The uncertainties of the quantities employed for the calculation of the impact parameter contribute to its error in different ways:

- the error of the nominal beam position is $\approx 180\,\mu$m in x and $\approx 50\,\mu$m in y and is independent of the measured muon track,
- the mean error of the track parameter *dca* is of the order of $70\,\mu$m.

These two quantities lead to an error of the absolute value of the impact parameter δ that is dependent on the azimuthal angle Φ of the muon, as can be seen in Fig. 5.12. For $\Phi = \pm 90°$, the error is largest and dominated by the width of the beamspot in x while at $\Phi = 0°$ and $\Phi = \pm 180°$ on the other hand, the error is smallest and rather equally composed from the y-size of the beamspot and the muon track resolution.

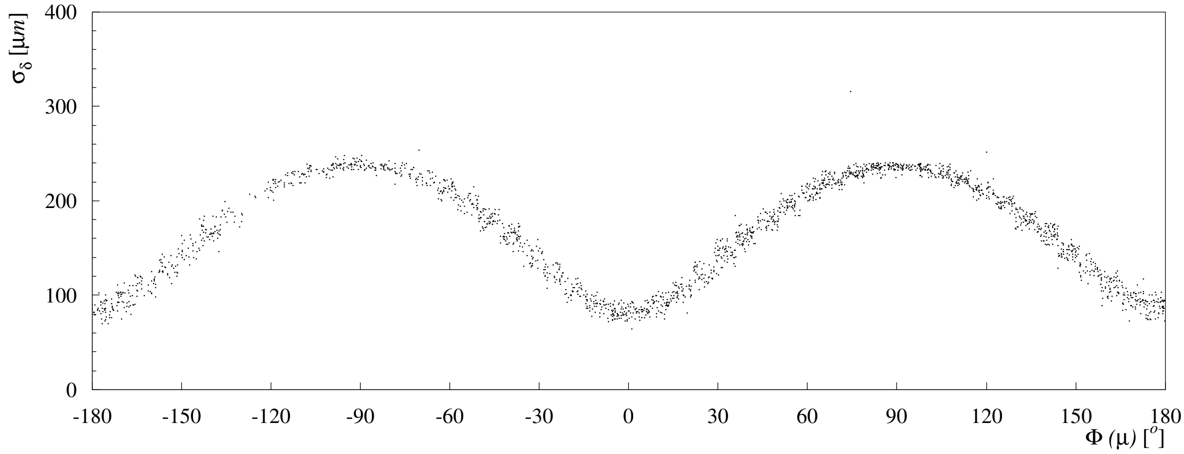

Figure 5.12: *Error on the impact parameter vs.* Φ*. The dependence on the dimensions of the beamspot is clearly visible: the error is largest for* $\Phi = \pm 90°$ *where the beamspot size in x-direction of* $\sigma_x \approx 180\,\mu m$ *is relevant. The error is determined for selected muon tracks (s. next section) by means of error propagation for* dca' *(Eq.* (5.8)*)*

Major improvements on the absolute value of the impact parameter can therefore be expected from a primary vertex fit based on tracks measured in the CST that resolves the beamspot. This still has to be developed. First attempts have shown that —provided there is a sufficient number of CST tracks— an iterative approach will be needed, where tracks are considered individually for matching to a common origin. It will probably also be necessary to allow for tracks that have not been measured in the CST to enter the fit additionally in order to improve statistics. For the present study however, the run-vertex has been used throughout.

The uncertainty on the *sign* of the impact parameter depends on

1. the quality of the thrust axis, that is its accuracy in approximating the original heavy quark flight direction,
2. the distance in x and y of the true event vertex from the run-vertex,

3. the precision of the reconstructed azimuthal angle Φ of the muon.

The effect on the impact parameter when taking these uncertainties into account is shown in Fig. 5.13 for the two M.C. samples. Starting from the generator level (top left), the generated azimuthal angle Φ of the muon is replaced by the reconstructed quantity first (top right). Next, the δ-distributions with the run-vertex replacing the generated production vertex of the heavy quark are shown (bottom left). The last histogram (bottom right) shows the reconstructed impact parameter, where the thrust axis has replaced the generated flight direction of the heavy quark. For the *b*-quark M.C.-distributions, the fractions of entries at positive and negative values of δ respectively are given in Tab. 5.3.

	$\delta < 0$	$\delta > 0$
a) generator	0%	100%
b) with reconstructed muon	$22.5 \pm 1.2\%$	$77.5 \pm 2.3\%$
c) with run-vertex	$33.6 \pm 1.5\%$	$66.4 \pm 2.1\%$
d) fully reconstructed	$44.5 \pm 1.7\%$	$55.5 \pm 1.9\%$

Table 5.3: *Fractions of entries at positive and negative values of δ for the b-quark Monte Carlo.*

It can be seen that the uncertainties due to the muon reconstruction lead to negative entries. The absolute values of δ for those entries are however compatible with the track resolution.

If the run-vertex is employed, the fraction of entries at negative values of δ is increased considerably. Moreover, the absolute values of the negative entries are no longer of the order of the track resolution. It must be concluded that these entries may carry life time information, i.e. are due to muons from heavy quark decays, but are sorted wrongly. This effect is strengthened by the additional uncertainties introduced by the use of the thrust axis instead of the flight direction of the heavy quark.

The sign of δ is determined as the intersection of the thrust axis and the muon track being in the forward or backward direction (s. previous section). The thrust axis approximates the heavy quark direction to an accuracy of $\approx 20^\circ$ and is thus the major source of uncertainty as compared to the reconstructed muon angle[2]. Therefore, especially at small decay angles α of the muon, errors of the angles of thrust axis and muon lead to an increased probability of obtaining negative values of δ.

At this point it can be summarized that the reconstructed impact parameter distributions show a considerable fraction of entries at negative values. Due to the uncertainties of the run-vertex and the thrust axis that lead to the assignment of the wrong sign, these can still carry life time information as is seen in M.C. distributions. However, even without applying cuts for the suppression of entries with negative values of δ, positive values are already favoured.

The expected shape of the impact parameter distribution of a muon sample that is enriched in heavy quark content —as will be introduced in the next section— is therefore asymmetric with respect to $\delta = 0$: at large positive values of δ, an excess of events should be present.

---

[2] For high-energetic cosmic tracks measured in the CST, the error on the azimuthal angle Φ was found to be 0.7 mrad, cf. Chap. 4.6.1

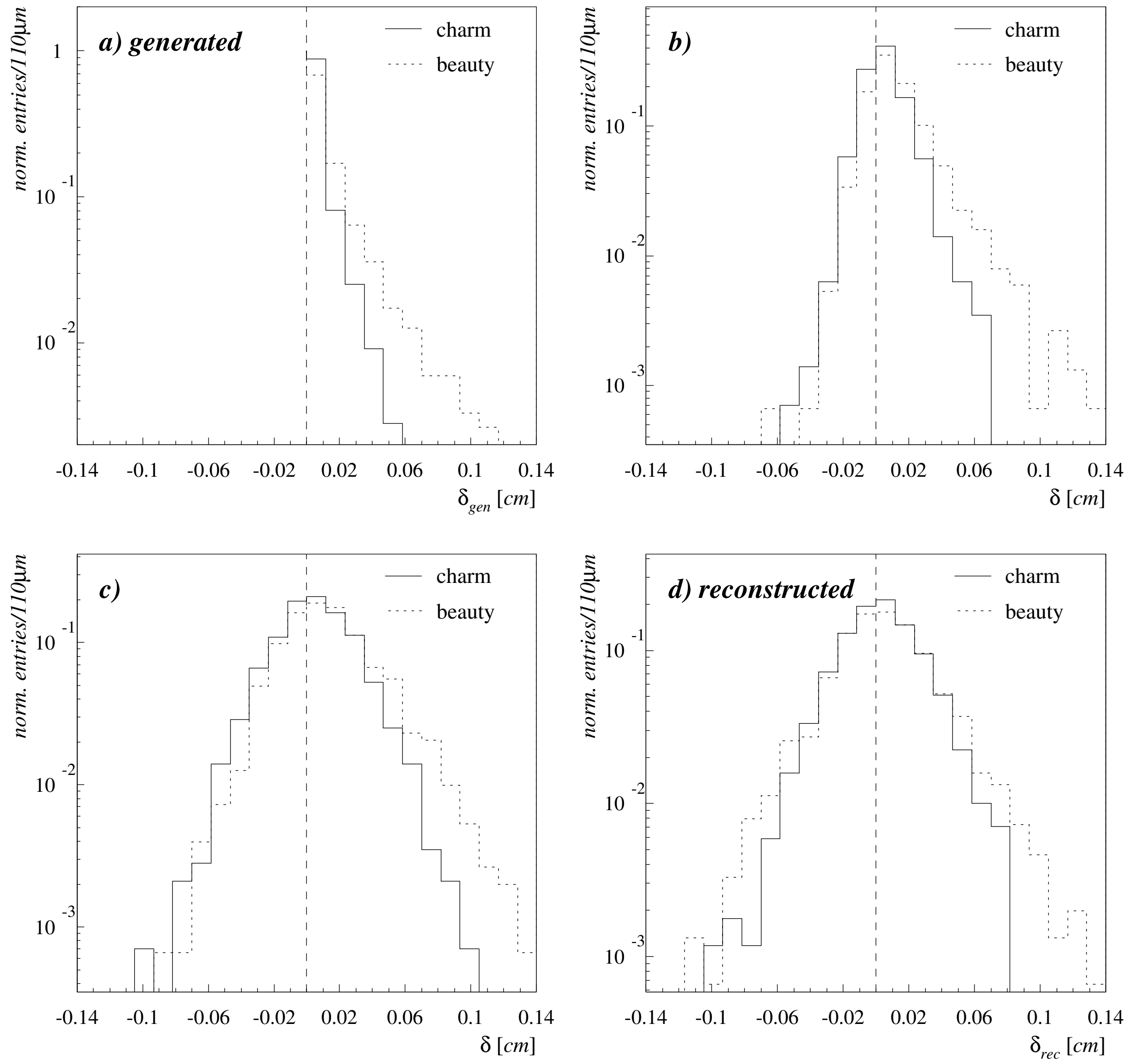

Figure 5.13: *Effects of reconstruction uncertainties on the impact parameter distributions.*
a) generator level (same as Fig. 5.7);
b) the reconstructed Φ*-angle of the muon is taken into account;*
c) in addition, the generated production vertex of the heavy quark is replaced by the run-vertex;
d) in addition, the thrust axis replaces the generated flight direction of the heavy quark: this is the reconstructed quantity.

5.3 Data selection

The basis for this explorative study is a sample of muons that have been measured in the iron barrel muon detector in the 1997 data taking period. The selection algorithm makes use of track information as well as of measurements of the muon detector. The search was restricted to the central part of the H1 detector: only the central track detectors and the iron barrel have been used. Additional conditions for an event to be accepted were the muon being measured in the CST, the existence of a run-vertex determined with CST tracks and the existence of a thrust axis in the muon hemisphere.

The analyzed data correspond to an integrated luminosity of 14.79 pb^{-1} which accounts for roughly 60% of the data taken with the CST in 1997.

The selection was applied to the simulated data for both $c\bar{c}$- and $b\bar{b}$-samples as well.

5.3.1 Selection of muon candidates

The first part of the selection looks for muon candidates by employing a standard software package of H1 [73]. Use is made of tracks measured in the central detector and of tracks reconstructed in the iron barrel detector which have been linked to the former. Additional identification in the LAr calorimeter is possible but not mandatory. Selection criteria are applied to the central tracks and the muon detector signatures separately first, and then on the quality of their matching.

General track selection The track selection is based on parameters measured by the CJC and the z-chambers. Information from the CST is not yet included. The following conditions must hold for a track to be considered further:

- minimal transverse momentum: $p_t > 150\,\text{MeV}$
- range in polar angle: $20° < \Theta < 160°$
- maximal absolute value of the dca (w.r.t. the primary vertex): $|dca| < 2\,\text{cm}$
- maximal radial distance of closest CJC hit to the beamline: $r_{start} < 50\,\text{cm}$
- minimal radial track length:
  - for $\Theta < 150°$: $r_{track} > 10\,\text{cm}$
  - for $\Theta > 150°$: $r_{track} > 5\,\text{cm}$

Muon selection The criteria of the muon selection make use of parameters from the muon detector reconstruction which returns so-called “iron tracks” and from the result of the linking of tracks measured in the muon detector to tracks measured in the CJC.[3]

- maximal radial distance of the extrapolated iron track to the primary vertex: $\rho < 100\,\text{cm}$
- maximal deviation of the z-coordinate of the extrapolated iron track at the beamline to the nominal interaction point ($z = 0$): $|z_{iron}| < 100\,\text{cm}$

---

[3] The linking step imposes an additional momentum cut of $p > 1$ GeV on a track.

- minimum number of wire layers hit: $N_{layer} \geq 2$
- first layer hit by the muon must be one of the first five layers: $I_{layer}(1.\text{ hit}) \leq 5$
- last layer hit by the muon must not be layer #1: $I_{layer}(\text{last hit}) \geq 2$.
- the track measured in the iron detector has to be been matched to the central track with a minimal probability: $\mathcal{P}(\chi^2_{\text{FE-CJC}}) \geq 0.001$

Apart from these standard requirements for a central muon, two additional criteria for its track parameters have been introduced at this stage:

- strict cut on transverse momentum: $p_t > 2\,\text{GeV}$
  This reduces the number of background events where a hadron leaking from the calorimeter to the muon detector fakes a muon. It also reduces the fraction of genuine muons that do not originate from the vertex region, e.g. decay muons from pions or kaons.
- minimal radial track length: $r_{track} > 22\,\text{cm}$
  This means implicitly that the track has been measured in both CJC1 and CJC2.

Selection after the CST reconstruction For the above preselected events containing at least one muon candidate the CST reconstruction is performed. The muon track must be reconstructed in the CST and it has to have:

- linked CST hits in both inner and outer layer
- a minimum fit probability of the CJC-CST track fit in R-Φ (cf. Chap. 4.6.1): $\mathcal{P}_{R-\Phi\text{-fit}} > 0.1$

For any further analysis steps, the improved muon track parameters delivered by the CJC–CST fit can now be utilized.

Selection on global event quantities In order to apply the impact parameter method, the run-vertex and the thrust axis that approximates the flight direction of the heavy quark are needed in addition to the muon track parameters themselves. For an event the following conditions must be fulfilled for an event to be accepted:

- a run-vertex determined from CST tracks has to be available[4].
- at least four tracks in the muon hemisphere are required for a calculation of the thrust axis. This is done as described in Chap. 5.2.1. Calorimeter cell information is utilized as well.

After all the above selection steps, a sample of 7332 events remains. 1703 events are left in the $c\bar{c}$ Monte Carlo sample and 1514 in the $b\bar{b}$-events. Some distributions of kinematic quantities for the three data samples are shown in Fig. 5.14.

---

[4] This might not be the case for very short runs where the statistics is not sufficient for a calculation of the run-vertex parameters, cf. Chap. 4.7.

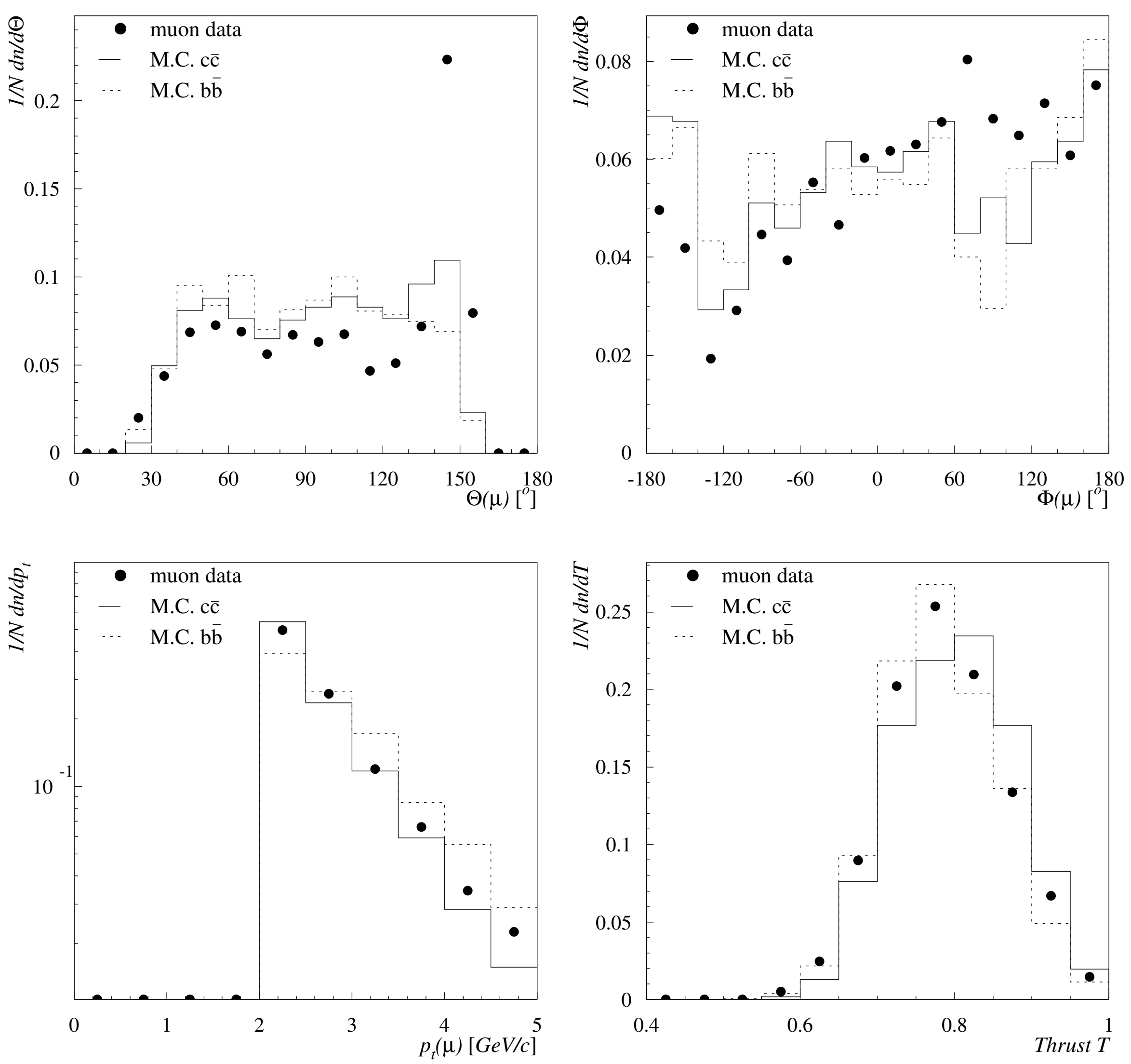

Figure 5.14: *Parameter distributions for the selected muon data and the two Monte Carlo samples. From top left: polar angle* Θ*, azimuthal angle* Φ*, and* p_t *of the selected muon. Bottom right: thrust value computed in the muon hemisphere.*

5.3.2 Background sample

Measuring the impact parameter of a muon from a heavy quark decay is dominated by background processes: hadrons originating from light quarks that fake a muon signature in the detector as well as muons from decays of kaons or pions in the detector. The distribution of δ for those particles however is distributed symmetrically around $\delta = 0$. In order to verify this behaviour, a *background event sample* has been selected additionally. This sample is independent of the muon selection and contains only a negligible fraction of semi-muonic heavy quark decays. It is chosen from events were the scattered electron has been measured in one of the electron-taggers at $z = 33$ or 44 m, thus belonging to the photoproduction event class. In addition to an energy deposition in one of the e–taggers, the existence of at least one independently measured track in the central tracking detectors with a transverse momentum of $p_t > 1.8\,\text{GeV}$ is required[5].

In the following, this track is then treated like the muon candidate in the signal sample. This means that it has to satisfy the criteria of the general track selection, has to have a minimal radial length of 22 cm, a minimal transverse momentum of 2 GeV, and has to be measured in the CST. For the selected events, the run-vertex has to exist and a thrust axis with respect to the hemisphere that is defined by the track has to be calculable. The identification in the muon detector is however not required.

5.3.3 Cuts for background reduction and b-quark enrichment

The selected events of the muon data sample still contain a considerable amount of background (cf. previous section). In order to reduce the number of hadrons that fake a muon signature, the range of the polar angle Θ is further restricted to $35° < \Theta < 135°$, thus excluding the backward region of the iron detector which is protected unsufficiently by hadronic calorimeters. Additionally, the cut on the minimal number of hit layers in the muon detector is raised to $N_{layer} \geq 5$.

As explained in Chap. 5.2.1, the probability of reconstructing a negative impact parameter rises for small values of the muon decay angle α. Therefore, a cut on the decay angle of $|\cos\alpha| < 0.95$ has been applied. This cut also increases the fraction of b-decay muons in the data sample since they are emitted at larger angles with respect to the decaying meson (cf. Fig. 5.6, left). For the two Monte Carlo datasets the resulting distributions for the impact parameter after this cut are shown in Fig. 5.15 (left histogram) and have to be compared to Fig. 5.13 d). An asymmetry with respect to $\delta = 0$ is now clearly visible for the $b\bar{b}$- M.C. data. A cut on the error of the impact parameter itself of $\sigma_\delta < 230\,\mu\text{m}$ reduces the fraction of impact parameters with a negative sign further (Fig. 5.15, right). As can be seen in Fig. 5.12, this is an implicit cut on the azimuthal angle of the muon track that excludes the Φ-range where the uncertainty on the beam spot position is largest.

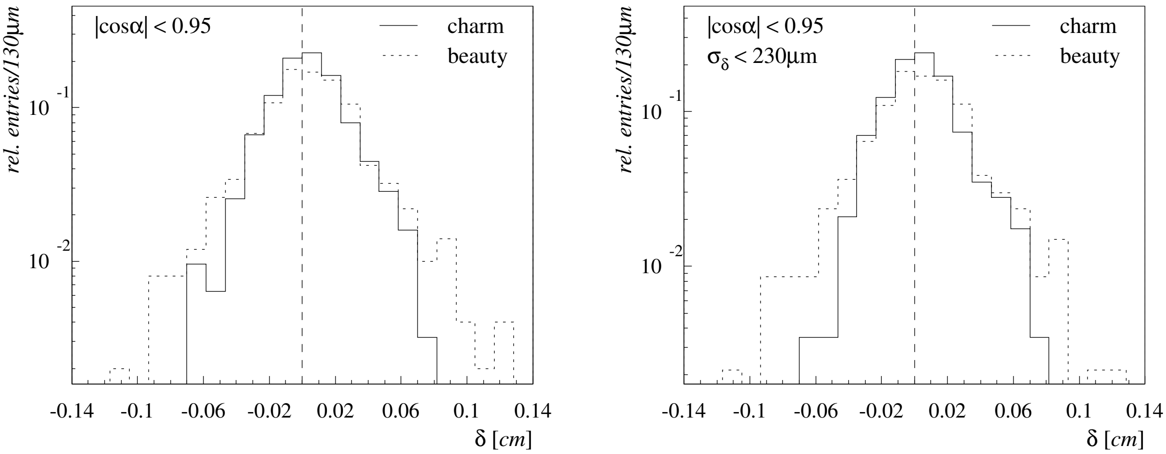

Figure 5.15: *Effect of cuts on the impact parameter distributions*

A further variable suitable for the separation of c- and b-quark decay muons is the relative transverse momentum $p_t^{R\Phi}$ of the muon with respect to the decaying heavy meson (cf. Fig. 5.6, right). For the

---

[5] This corresponds to the H1 event class 21 (`PTETAG`).

reconstructed data, with the thrust axis approximating the quark direction, a clear separation of muons from charm and beauty is not possible anymore (cf. Fig. 5.11, right). However, a cut on $p_t^{R\Phi} > 1$ GeV suppresses events from c-quark decays further.

The number of remaining events after applying the various cuts is shown in Tab. 5.4 for both muon and background sample. After all cuts, the Monte Carlo statistics is rather low which is due to the fact

integrated luminosity $\mathcal{L}$ [pb^{-1}]	muon data 14.79	background 1.28	M.C. $c\bar{c}$ 10.78	M.C. $b\bar{b}$ 47.62
Events after muon selection and CST reconstruction	7332	13666	1703	1514
$35° < \Theta(\mu) < 135°$	5346	9998	1394	1299
$N_{layer} \geq 5$	3238	—	1000	993
$\sigma_\delta < 0.023\,\text{cm}$	2702	8328	925	924
$\lvert\cos\alpha\rvert < 0.95$	1443	6521	286	467
$p_t^{R\Phi} > 1$ GeV	1139	5956	267	451

Table 5.4: *Remaining number of events after selection cuts*

that the new CST simulation program was not officially released yet and therefore no use of Monte Carlo mass production could be made.

5.4 Results

The distributions of the impact parameter δ for both muon and background data samples are plotted in Fig. 5.16. The spectrum for the muon sample is clearly skewed to positive values of δ whereas the background distribution is symmetric. At negative values of δ the two distributions agree very well. Those stem from Gaussian-distributed background (e.g. kaons or pions), from tracks with a small value of α, the opening angle between muon direction and thrust axis, and from reconstruction uncertainties due to the use of the run-vertex and the thrust axis. The background distribution has been fitted with the sum of two Gaussians in order to account for the entries at large absolute values of δ. The width of the Gaussian describing the entries in the peak at small values of δ is $\sigma \approx 120\,\mu$m and is thus compatible with the mean error on δ which is dominated by the resolution of the beam spot.

In order to study the excess of events at positive values of δ, the above distribution is subdivided into three regions:

- the left side of the histogram defined by $\delta < -0.02\,\text{cm}$. Entries in this region are due to the assignment of the wrong sign to the value of δ.
- the central region of the distribution defined by $-0.02\,\text{cm} \leq \delta \leq 0.02\,\text{cm}$. Here, a large fraction of background is present. The entries carry little or no life time information since the value of δ is of the order of its error.
- the right side of the histogram with $\delta > 0.02\,\text{cm}$. This is the "region of interest" where the entries are expected to stem from muons originating from heavy quark decays.

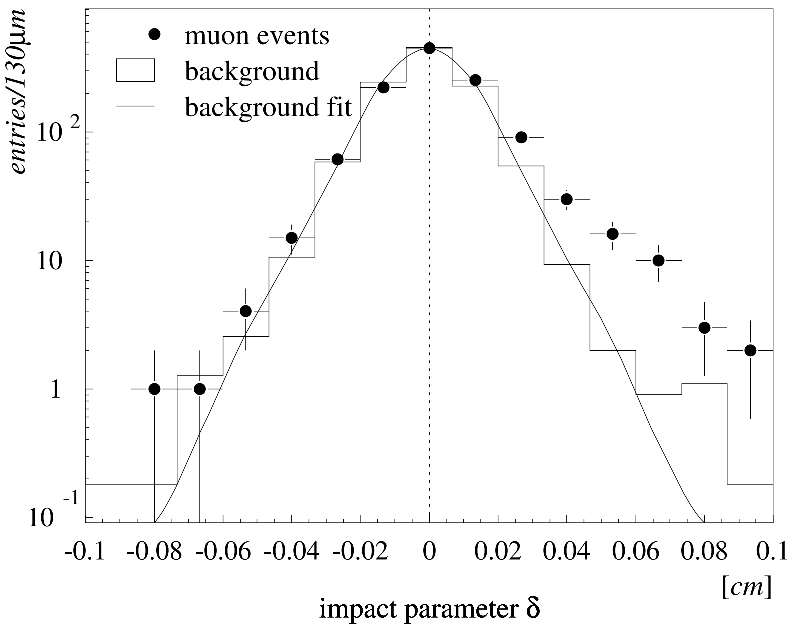

Figure 5.16: *Impact parameter distributions for muon events and background. The background histogram has been normalized to the number of entries in the muon data histogram with* $-0.02cm \leq \delta \leq 0.02\,cm$*. The bin width of 130μm corresponds to the mean error on the value of* δ *(cf. Fig. 5.12). The function fitted to the background distribution is the sum of two Gaussians.*

The distributions of the two M.C. data samples each have been normalized to the number of entries in the central region. They are plotted in Fig. 5.17, together with the muon data and the fit function to the background sample. Both M.C. samples show a clear deviation from the shape of the symmetric background, in particular an excess of entries for $\delta > 0.02\,$cm. The fractions of the entries in the three regions are given in Tab. 5.5. For the background distribution, the symmetry is expressed in equal fractions for the left and right tail respectively. For both of the two background-free M.C. data samples, the fractions of events in the region of positive δ-values are increased. The higher b-quark life times are reflected in a larger value for the $b\bar{b}$- than for the $c\bar{c}$-sample. However, the same is true for the region of negative δ-values. Since the sign of the impact parameter is determined independently of its absolute value, a possible explanation is that the entries in the left tail do carry life time information, but get a negative δ-sign due to the reconstruction uncertainties.

	muon data	background	M.C. $c\bar{c}$	M.C. $b\bar{b}$
$\delta < -0.02\,$cm	7.1±0.8%	6.9±0.3%	12.4±2.1%	18.1±2.1%
$-0.02\,$cm $< \delta < 0.02\,$cm	79.7±2.6%	86.7±1.2%	68.6±5.0%	54.9±3.5%
$\delta > 0.02\,$cm	13.2±1.1%	6.4±0.3%	19.0±2.6%	27.0±2.4%

Table 5.5: *Fractions of entries in the three regions of the impact parameter distributions*

The muon data distribution finally shows a large surplus of entries in the right as compared to the left region. This is caused by the fact that the signal is composed of muons from heavy quark decays and

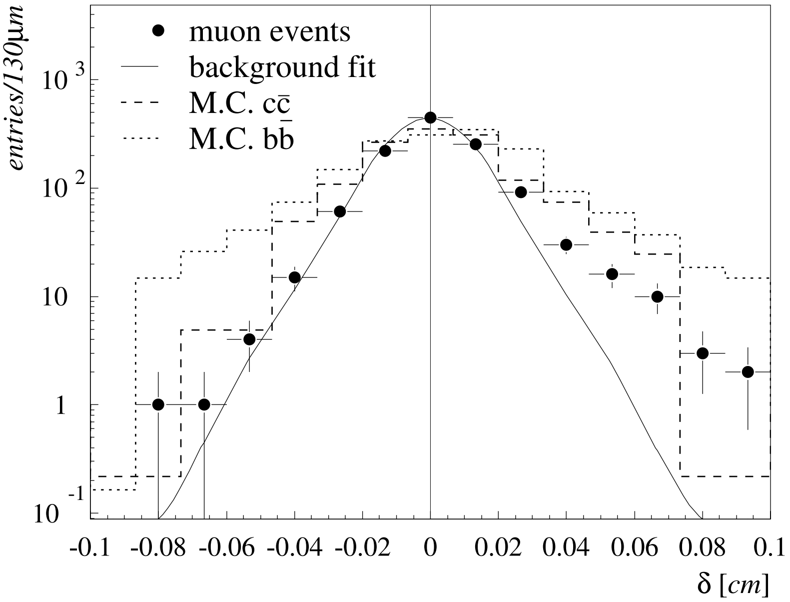

Figure 5.17: *Impact parameter distributions for muon data and the $c\bar{c}$- and $b\bar{b}$-Monte Carlo samples. The M.C. are each normalized to the number of events in the muon data with* $-0.02\,cm \leq \delta \leq 0.02\,cm$*. The function fitted to the background data sample (cf. Fig. 5.16) is shown in addition.*

of background.

Fig. 5.18 shows the distributions for the decay angle α and the relative transverse momentum $p_t^{R\Phi}$ of the muon. The expected behaviour for the two M.C. data samples is visible: muons from c-quark

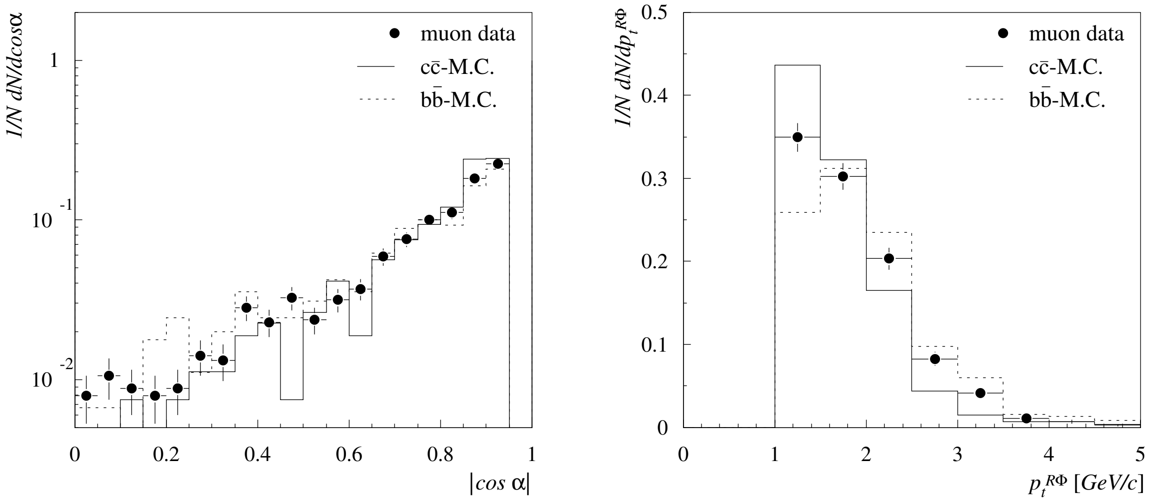

Figure 5.18: *Distributions for decay angle* α *(left) and relative transverse momentum* $p_t^{R\Phi}$*. All histograms are normalized to 1.*

decays are on average emitted at smaller angles α and have a lower relative transverse momentum $p_t^{R\Phi}$. The decline of the $p_t^{R\Phi}$ distribution for the muon data towards larger values is not as steep as for the c-quark decay muons but rather follows the b-distribution. At low values of $p_t^{R\Phi}$ however, the muon data have more entries compared to the b-quark M.C. sample.

Dependence of δ on $p_t^{R\Phi}$ In the next step, the distribution of the impact parameter is probed by raising the $p_t^{R\Phi}$-cut, so that the b-quark content is further enriched. The resulting effect on the impact parameter distribution of the muon data sample is shown in Tab. 5.6 where again the fractions of entries for the tails of the distributions are given: The fraction of entries at positive δ-values is enlarged with raising $p_t^{R\Phi}$ while the fraction at negative δ-values decreases.

$p_t^{R\Phi}$-cut [GeV/c]	> 1.0	> 1.5	> 2.0	> 2.5
$\delta < -0.02\,\mathrm{cm}$	7.1±0.8%	8.3±1.4%	6.9±2.0%	4.0±1.9%
$\delta > 0.02\,\mathrm{cm}$	13.2±1.1%	14.4±1.9%	16.0±3.0%	16.8±3.7%

Table 5.6: *Fractions of entries in the impact parameter distribution of the muon data sample for different $p_t^{R\Phi}$-cuts*

Applying the higher $p_t^{R\Phi}$-cuts to the background data sample does not change the shape of the impact parameter distribution: it remains symmetric with $\approx 6\%$ of the entries in the left and right tail respectively (cf. Tab. 5.5).

The lack of statistics inhibits significant statements on the M.C. distributions, especially on the $c\bar{c}$-sample (cf. Tab. 5.4). The correlations between the impact parameter δ and $p_t^{R\Phi}$ are shown in Fig. 5.19. The fact that the excess of entries at positive values of δ gets more prominent with rising $p_t^{R\Phi}$ is strong evidence that the asymmetry is indeed due to muons originating from decays of heavy quarks.

Dependence of δ on the azimuthal angle Φ of the muon The Φ-dependence of the impact parameter distribution provides a means to study possible systematic errors that are introduced by the reconstruction. As shown in Fig. 5.12, the error on δ depends on the extensions of the beamspot and therefore on Φ. The muon data sample was divided into a subsample with a small error of δ by requiring

$$|\Phi_\mu| > 140^\circ \quad \texttt{.OR.} \quad |\Phi_\mu| < 50^\circ$$

and a sample for the complementary range of Φ where the error on δ is large. The two regions are indicated in Fig. 5.20. The corresponding impact parameter distributions are shown in Fig. 5.21. Both distributions still show a clear asymmetry. The fractions of entries for left and right tails are given in Tab. 5.7. The result is that the fraction of entries at negative δ-values relative to the one at

	small error on δ $\lvert\Phi(\mu)\rvert > 140^\circ$ .OR. $\lvert\Phi(\mu)\rvert < 50^\circ$	large error on δ $50^\circ < \lvert\Phi(\mu)\rvert < 140^\circ$
$\delta < -0.02\,\mathrm{cm}$	4±0.8%	11±1.6%
$\delta > 0.02\,\mathrm{cm}$	10.8±1.2%	17.4±2.0%

Table 5.7: *Fractions of entries in the impact parameter distribution of the muon data sample for two ranges of Φ corresponding to small and to large errors of δ respectively.*

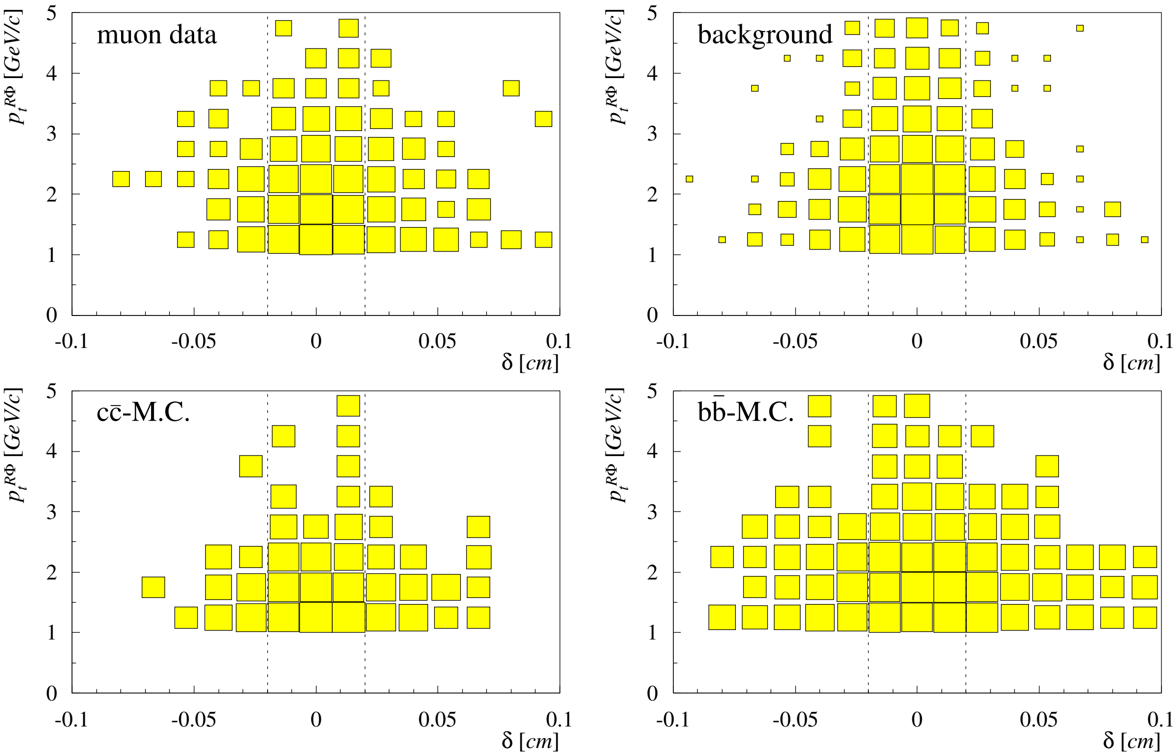

Figure 5.19: *Correlation between the impact parameter* δ *and* $p_t^{R\Phi}$. *The dotted lines at* $\delta = \pm 0.02\,cm$ *indicate the partitions for the symmetric center and the tails of the* δ*-distribution.*

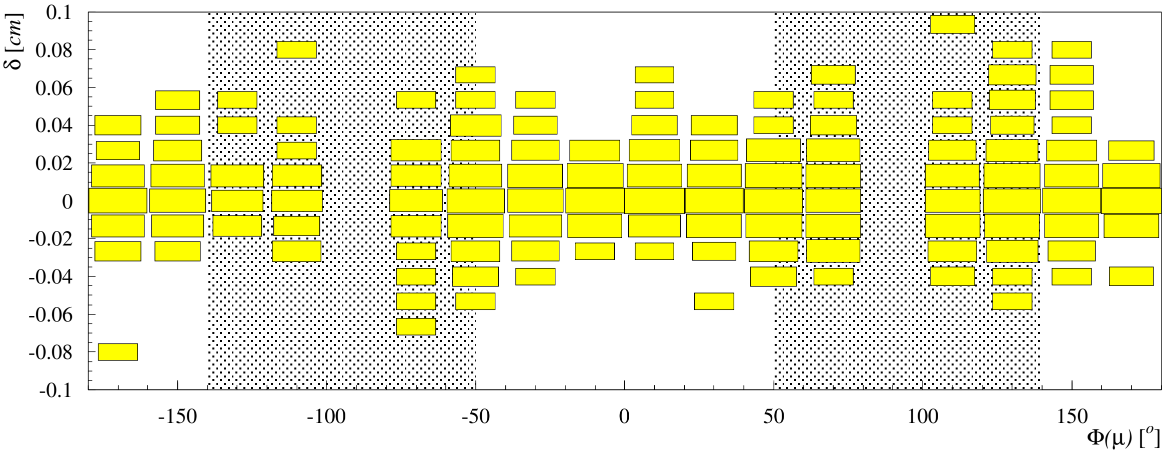

Figure 5.20: *Correlation of* δ *and* $\Phi(\mu)$. *The shaded regions indicate the* Φ*-range where the error on* δ *is large due to the larger beam spot extension in x-direction. The "holes" at* $\Phi = \pm 90°$ *are due to the cut of* $\sigma_\delta < 230\mu m$, *cf. Chap. 5.3.2.*

positive values decreases for small errors of δ. This means that as expected, the improved accuracy of the reconstruction lowers the probability of assigning a negative impact parameter. The fact that the excess of entries at positive values of δ is significant for both subsamples shows that the asymmetry is not due to systematic errors of the reconstruction.

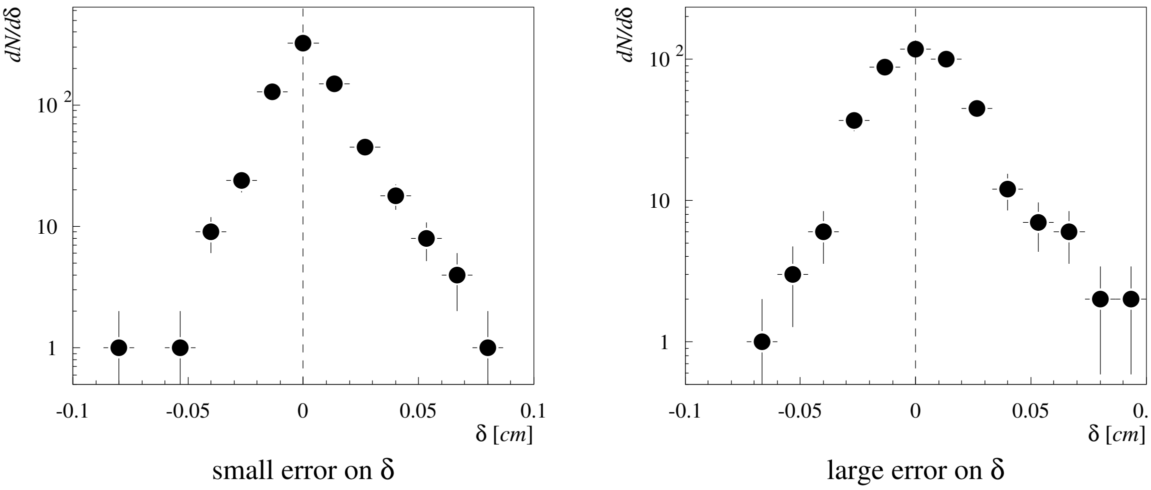

Figure 5.21: *Impact parameter distributions for the two subsamples of the muon data. Left: region with small* δ*-errors (* $|\Phi(\mu)| > 140^\circ$ `.OR.` $|\Phi(\mu)| < 50^\circ$*), right: region with large* δ*-errors (* $50^\circ < |\Phi(\mu)| < 140^\circ$*).*

5.5 Conclusions

It has been shown that by employing the tracks measured in the CST with improved resolution, the impact parameter is a suitable quantity for the detection of muons from heavy quark decays.

The impact parameter is calculated in the R-Φ-plane by using the track parameters of the muon that are improved by CST measurements, the run-vertex parameters to approximate the production vertex of the heavy quark, and the thrust axis to approximate its flight direction. The absolute value of the impact parameter is then given by the distance of closest approach of the muon track to the run-vertex, and its sign is determined from the intersection of muon track and thrust axis.

The final distribution shows an excess of entries at positive values of δ which can be attributed to particles whose origin is separated from the primary vertex. This was further investigated by raising the cut on the relative transverse momentum $p_t^{R\Phi}$ which enlarges the number of muons originating from b-quark decays, i.e. suppresses background and also muons from c-quark decays. The result is a more pronounced asymmetry of the impact parameter distribution.

The Monte Carlo data samples studied for comparison support the qualification of the impact parameter as a suitable observable for a tagging of heavy quark decays.

A large source of uncertainty of the impact parameter is the employment of the run-vertex as an approximation of the production vertex of the heavy quark which leads to entries at negative values of δ. This is demonstrated by comparisons of reconstructed and generated quantities in Monte Carlo and is proven in data by restricting the error of the run vertex position which is equivalent to limiting the Φ-range of the reconstructed muon. As a result, the *origin* of the thrust axis is better determined so that the assignment of a negative sign to the impact parameter is less likely. The expected reduction of the fraction of entries at negative values of δ in the data is found.

The limitations of the present method —where the errors of the vertex position are given by the size of the beam spot— will be overcome in the future by fitting a primary event vertex with CST tracks.

However, for such a fit several tracks that originate from the primary vertex *and* are measured in the CST are needed in every event. Apart from improving the reconstruction of the primary vertex as the origin of the heavy quark, a higher precision of the determination of its *direction* is also desirable for the future. It has to be studied whether the accuracy of the thrust axis approximating the quark direction can be improved by e.g. employing alternative algorithms for its determination.

From a greater accuracy of the reconstructed quantities an improvement of the available statistics can be expected since some of the selection cuts (e.g. the cut on the muon decay angle α) can be lowered.

Summary and Outlook

This thesis presents the readout system and the event reconstruction of the Central Silicon Tracker (CST), the microvertex detector of the H1 experiment at HERA that has begun data taking in 1997. In addition, an explorative study on heavy quark decays using CST data is reported.

The CST consists of double-sided silicon strip detectors measuring charged particles in the plane perpendicular to the beam axis (R-Φ) as well as in R-z (where the z-axis is defined by the proton beam direction). This is achieved by arranging the strips on the p- and the n-side of the detectors at an angle of 90° with respect to each other. The detector is centered at the nominal interaction point and covers 100% of the azimuthal angle Φ and a polar angle range of $30^\circ < \Theta < 150^\circ$.

In addition to the large number of readout strips (81920 in total), the readout system of the detector has to cope with event rates of 10.4 MHz due to the HERA bunch crossing frequency. Moreover, detector signals from single events have to be stored intermediately to allow for the decision time of the central trigger of $2.4\,\mu$s. These requirements are met by the use of custom-designed readout chips with an integrated pipeline consisting of 32 analog buffers. During data sampling, the pipeline is operated at the HERA frequency. If an event is triggered by other subdetectors of H1, the signal charges from the respective pipeline buffer are amplified, multiplexed, and transferred to dedicated processor modules where they are digitized. The memory of these modules provides a 16-fold multi-event buffering, so that the subsequent online processing of the data can be performed asynchronously to the trigger signals.

The purpose of the online processing is the reduction of the amount of raw data. Only the data from readout strips that have been hit are transferred to the main data acquisition system for eventual permanent storage. The implemented hit finding algorithms rely on correct readout constants, namely pedestals and values for the noise of each readout strip. The task of determining and updating these constants is also performed online by the processor modules. The design goal of operating the online processing system at triggered event rates of ≈ 100 Hz without introducing dead time was achieved in the first year of operation. On average, the event size is reduced by a factor of 60. At the same time, the online hit finding algorithms are efficient in the sense that no hit information is lost.

On the basis of the reduced data, the event reconstruction is performed. Its goal is to use the CST hit data to improve the accuracy of the track measurements in the central region of the H1 detector. A necessary requirement in this respect is the correct alignment of the CST with respect to the surrounding jet chamber CJC. A set of alignment constants has been successfully determined from the data of 1997, and the remaining uncertainties are smaller than the intrinsic resolution of the CST.

In the first reconstruction step, clusters are built from the information of the hit strips. The cluster position is calculated by means of a center-of-gravity algorithm. The subsequent transformation to the H1-coordinate system takes the alignment corrections into account. Next, the found clusters are assigned to tracks measured by the CJC. This reconstruction step is done separately for the R-Φ- and the R-z-projections. The efficiency for the p-side linking of a CJC track to a CST cluster is 98%. On the n-side which has a lower signal-to-noise ratio, an efficiency of 86% was measured.

With the assigned spacepoints the track parameters as measured by the CJC are improved. Again separately for R-Φ- and R-z, a constrained fit is performed. The resulting track resolutions were studied using a sample of high-energetic cosmic ray tracks. For the track curvature κ, its closest approach dca to the nominal interaction point, the z-coordinate z_0 at the dca, and the azimuthal and polar angles Φ and Θ the following resolutions were measured:

$$\begin{aligned} \sigma(\kappa) &= 1.68 \times 10^{-5}\ \mathrm{cm}^{-1} & \qquad \sigma(\Theta) &= 0.9\,\mathrm{mrad} \\ \sigma(\Phi) &= 0.7\,\mathrm{mrad} & \qquad \sigma(z_0) &= 83\,\mu\mathrm{m} \\ \sigma(dca) &= 44.7\,\mu\mathrm{m} \end{aligned}$$

With these improved tracks the potential of CST measurements for heavy quark tagging was demonstrated by the study of the semi-muonic decay of particles containing heavy quarks. A sample of events with muons of high transverse momentum ($p_t > 2\,\mathrm{GeV}$) has been selected from the data taken with the CST in 1997, and the impact parameter method was applied in order to prove that the origin of the muon tracks is separated from the primary event vertex. A significant asymmetry in the impact parameter distribution is seen which is not present in a background data sample that was selected for comparison.

Different sources of systematic uncertainties in the measurement of the impact parameter have been studied, and a dependence on the accuracy of the primary vertex position and on the quality of the thrust axis approximating the flight direction of the decaying heavy quark have been found.

If the b-quark content of the muon sample is further enriched by applying harder cuts , the on average longer lifetime is reflected by a more significant asymmetry in the impact parameter distribution. This finding is supported by Monte Carlo data samples containing muons from c- and b-quark decay respectively that have been studied in addition. Both also show the asymmetry of the impact parameter distribution which is even more pronounced for the b-quark sample.

It can be concluded —as in previous experiments at other colliders— that the impact parameter that is determined for tracks measured in the CST is a useful observable for tagging heavy quark decays.

Since the readout system of the CST proved to work reliably in 1997, it was not changed for the 1998 data taking. A number of developments are going on with respect to the event reconstruction however: The primary goal is the implementation of a primary vertex fit on the basis of tracks measured in the CST. This will overcome the limitations in the precision of the vertex position that are presently given by the radial extensions of the particle beams. A secondary vertex finder has already been developed. These vertex positions can also be used to improve the linking of CJC tracks and CST hits in the R-z-projection since they impose an additional constraint on the track parameters. In the R-Φ-projection, the linking can be improved further by a special treatment of clusters which are erroneously reconstructed as two separate (“split”) clusters due to dead readout strips. With the new CST detector simulation that has to be cross-checked and tuned further, a valuable tool for improving the reconstruction is now available.

An implementation of the CST reconstruction program on the processor farm for online filtering is foreseen in the near future. Due to the high precision of the tracks measured in the CST, the capability of recognizing events with heavy quarks online is increased considerably. Moreover, a better determination of the z-vertex, as is possible with the CST, is of general importance for nearly all physics channels considered in the filtering process.

Presently, CST data are beginning to be exploited in more and more physics analyses, in particular those in the field of charmed particles. In 1998 the CST reconstruction is part of the standard H1 event reconstruction, and CST data will thus be available more easily in 1998. It can therefore be expected that their great potential —in particular in the field of heavy quark physics— will contribute to many new results.

Appendix A

Specifications for the readout system

This appendix is intended to give a more detailed documentation on some aspects of the readout system, namely an overview over all components, a memory map for the RIO2 processor modules, and descriptions of the readout parameters and of the data formats.

A.1 Overview of the components of the readout system

Basic building blocks are the VME crates that are connected by means of the fibre-optic VMEtaxi ring. The master crate (number 0) is connected to the main fibre-optic data acquisition ring of H1 as well. Crates number 1 and 2 contain the OnSiRoC control modules for CST and BST respectively. Crate number 3 houses the RIO2 processor modules, while crate number 7 keeps modules handling the incoming trigger signals as well as the response of the silicon branch. The master monitoring crate that contains the modules of the Silicon Farm is connected to the master readout crate using VSB. For each of the two crates, a proprietary Macintosh computer allows user intervention. Not shown in the figure are the Macintoshes connected to the CST and BST OnSiRoC crates.

The software package for the VMEtaxi modules of the H1 experiment [74] has been considerably extended for being employed in the silicon readout branch [45, 75]. It allows interaction with the modules via serial lines from terminals in the control room. In this way, an initialization or a memory display not only of the VMEtaxi boards themselves, but also of the OnSiRoC or RIO2 modules in the addressed crate is possible.

H1 Silicon Tracker Data Acquisition

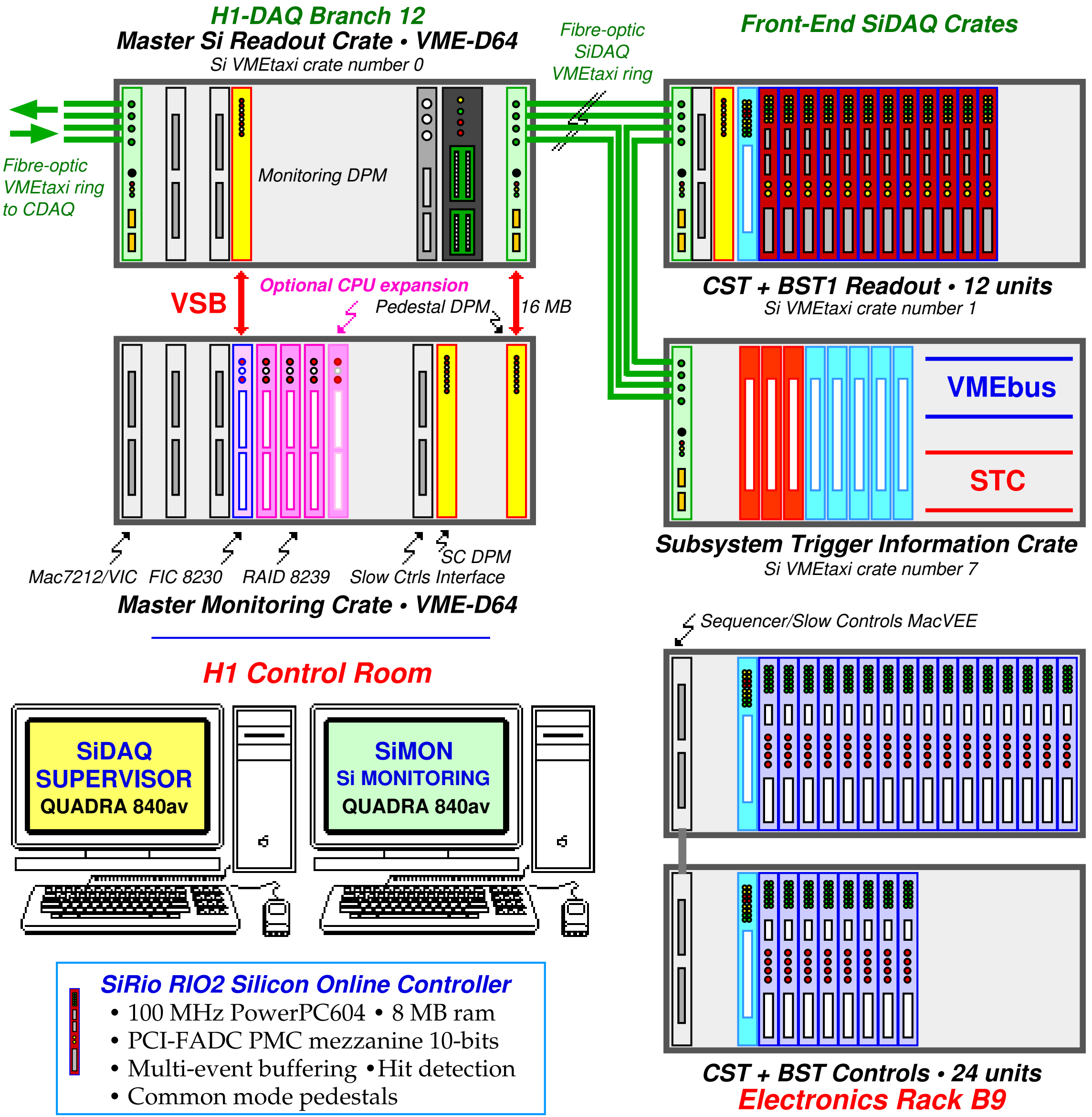

SiRio RIO2 Silicon Online Controller

- 100 MHz PowerPC604 • 8 MB ram
- PCI-FADC PMC mezzanine 10-bits
- Multi-event buffering •Hit detection
- Common mode pedestals

VMExi2, VMEtaxi Mark-2

- Fibre-optic VMEbus crate interconnect
- 50 MHz 68030, program & data sram
- 2x175/250 MHz taxi transceiver pairs
- 33/55 MBytes/sec xram transfer rates

CPU processor card RAID 8239

- 40 MHz R3000, FPU, 128 K data cache
- 16 MBytes on-board dram
- Real-time data spy-monitoring, quality control & calibration

DPM 8242, Dual-Ported Memory

- VME/VSB static ram board
- 4 MBytes Battery back-up
- Use for storage of pedestals, etc

MacVEE/Mac7212

- Mac-VMEbus
- Si event display
- Control & monitor

OnSiVoC

- Voltage Controller
- Sequencer

H1SiDAQ • Upgrade Layout • August 1996 • WJH

A.2 Memory map for the readout module RIO2

Below, the memory map for the RIO2 readout boards is shown (taken from [45]). Apart from accessing the Raw-, Hit-, Pedestal-, and Sigma buffers, the hit finding routines need no further interaction with the memory since all information is passed via input and returning arguments.

Global Area Memory Map Offsets (Total = 8 MBytes)

All offsets must be added to Base.

```
$0000’0000 - $0000’1000 ; VMEtaxi SiDAQ parameters       Taxi/W PPC/Read 4KB max
$0000’0000 - $0000’0080 : Mailbox area
$0000’0080 -            ; Status offset (STATOFF)   length $80   Taxi/W PPC/R
$0000’0100 -            ; SiDAQSPEC block (SPECOFF) length $80   Taxi/W PPC/R

$0000’1000 -            ; Event Indicator Area (EVENTOFF)        Taxi/PPC/W/R
                                  (see separate section for description)

$0010’0000 - $001F’FFFF ; Event Data Area 1 Mbyte                Taxi/R PPC/W

$0010’0000 - $0017’FFFF ; Raw Event Data 16 buffers each of 32 KBytes
$001N’0000 - $001N’7FFF ; Raw Event Data Buffer 2N   (N=0 thru 7)
$001N’8000 - $001N’FFFF ; Raw Event Data Buffer 2N+1 (N=0 thru 7)
eg.
$0010’0000 - $0010’7FFF ; Raw Event Data Buffer 0
$0011’8000 - $0011’FFFF ; Raw Event Data Buffer 3
$0013’0000 - $0013’7FFF ; Raw Event Data Buffer 6
$0017’8000 - $0017’FFFF ; Raw Event Data Buffer 15

For each Raw Data Buffer the following offsets are written to by the Xilinx:
$7FF8 - $7FFB : Pipeline counter once ADC data are written
$7FFC - $7FFF : Xilinx Event Number flag once ADC data are written
The Event Number flag must be the last written word by the Xilinx.
It is then cleared by the ppcdaq_readout task for internal bookkeeping.
In principle the Xilinx needs only write access to the Global area over the PCI.
Note also the use of the location $001N’7FF4 as a last data word flag.
Should this last effective data word location be indicated none-zero, contrary to the
event number flag, the PIC is set to $FF with a software incremented event number.

$0018’0000 - $001F’FFFF ; Hit Event Data in blocks of maximum size 32 KBytes
eg.
$0018’0000 - $0018’7FFF ; Hit Event Data Buffer 0
$0019’8000 - $0019’FFFF ; Hit Event Data Buffer 3
$001B’0000 - $001B’7FFF ; Raw Event Data Buffer 6
$001F’8000 - $001F’FFFF ; Hit Event Data Buffer 15

$0020’0000 - $002F’FFFF ; Pedestals (8192*2*32 peds*16-bits)  xi/PPC/R/W 1MB max

$0030’0000 - $003F’FFFF ; Simulation Event Data Area SIMODE bit 8 set (see below)

$0040’0000 - $005F’FFFF ; Available for constants storage     xi/PPC/R/W 2MB

$0060’0000 - $006F’FFFF ; Reserved                            xi/PPC/R/W 1MB

$0070’0000 - $007F’FFFF ; Temporary PPC program space         xi/W PPC/R 1MB max
$0070’0000 - $0070’7FFF ; Main task booted from fprom ($E’0000) on reset
$0070’8000 - $0070’FFFF ; Hit detection algorithm booted from memory on reset
                          Memory is battery-backup at $C0’8000
                                Raw Object from MPW-PPC-C. Real start at offset $8C.
```

A.3 Global readout parameters

The `SiDAQSpec` parameter block is known to every processor in the Silicon data acquisition branch. It contains the run parameters as set on the System Supervisor silicon branch panel:

`SiDAQSpec` Acronym	label on Supervisor	valid for mode	meaning and effects
`SiMask`	Crates in readout	all	Bits set for corresponding crates to read out
`SiMode`	Readout mode	all	defines readout mode
`SiHDThresh`	CST Hit Threshold	Hit&Cluster Extra	CST: Sigma threshold for a hit strip
`SiCDThresh`	CST Cluster Threshold	Hit&Cluster Extra	CST: Cluster threshold
`SiRESERVED[0]`	CST select FADC.RIO	Monitor	CST: select FADC
		Hit&Cluster Extra	CST: select RIO&FADC for additional Raw data output
`SiRESERVED[1]`	BST select FADC.RIO	Monitor	BST: select FADC
		Hit&Cluster Extra	BST: select RIO&FADC for additional Raw data output
`SiRESERVED[2]`	free		
`SiRESERVED[3]`	free		
`SiLLPuls`	CST length to left	Extra	CST: no. of left cluster neighbours to be written out
`SiLRPuls`	CST length to right	Extra	CST: no. of right cluster neighbours
`SiSWThresh`	free		
`SiPPCMask1`	PPC mask (crate 3)	all	Bit mask for RIO2s in crate 3
`SiPPCMask2`	PPC mask (crate 4)	all	Bit mask for RIO2s in crate 4

A.4 Front-end bank formats

SiDAQ Header Bank

- Name = 'SDAQ'
- XiDAQ Branch Number = 12
- Index = 0
- Length = 1
- Event Number

The SDAQ header bank indicates that Silicon data are present in the event.

SiDAQ Run-Start Record

- Name = 'SIRS'
- XiDAQ Branch Number = 12
- Index = 0
- Length = 12
- `SiDAQSPEC` 8 word block
- OnSiRoC/RIO2 bit pattern (4 words)

The run-start record is only written at the beginning of a data acquisition run. It contains the run-parameters for the Silicon branch as defined in the `SiDAQSpec` block described in App. A.3. Additionally a bit pattern of the modules present in the OnSiRoC and RIO2 crates is contained.

SiDAQ Front-End Data

- Name = 'SIFE'
- Branch, Crate, LastPPC, PIC
- Index = 0
- Length
- 1st word = Event Number
- Front-End Data Block

The SIFE bank contains blocks of data written by the RIO2 readout modules. One bank per readout crate is written while LastPPC indicates the module with the highest number found in this crate. The pipeline counter (PIC) in the bank header is taken from this board.

A.5 CST data word formats

The following holds for any readout mode except RAW. All descriptions refer to 32-bit words. As explained in Chap. 3.1.4, the SIFE bank is substructured by means of *Control Words* that mark the beginning of a data block for one RIO2 board or for data from one FADC processed by this module.

Data from the CST always start with the

```
CST Main PPC Control Word

        BBMMMSpp'ppmmmmmm'mmllllll'llllllll

B:      2-bit branch = 00 (CST), 01 (BST1), 10 (VLQ)
M:      3-bit SiMode word: 0 = DATA, 1 = COPYRAW, 3 = MONI, 4 = EXTRA
S:      if set, Specials are present in the data
p:      4-bit RIO number
m:      8-bit FADC wanted mask
l:      14-bit length of RIO data (in long words). Max 32 kB = 8k words.
-------------------------
```

After this header word follow nine more words having the following format and meaning for the CST:

```
CST PPC data header

1       HitFinding Time (16 MHz counter)
2       Updating Time (16 MHz counter)
3       Event Number (24bit) | PIC
4       Raw Address
5       Bit Mask for pending PPC raw buffers
6       Version number
7       reserved
8       reserved
9       reserved                      :
```

This header block is always present.

The data block is then again substructured with respect to data from the different FADCs. At the top of each “FADC data block” there is again a header word which contains the length of the block and the FADC number. These FADC data blocks can contain different information: hits, raw data, pedestals, sigmas or the common modes (for 10 connected APCs). The CST FADC Block Control Word has the following format:

```
CST Block Control Word

        00000000'WtttfffV'llllllll'llllllll

t:      3-bit data type: 000-Hits, 001-Raw, 010-CM, 011-Ped, 100-Sigma
f:      3-bit FADC number (0-7)
V:      Voltages on/off (detected by checking Specials)
l:      16-bit length of FADC data block (in long words)
----------------------------------------
```

The format of the following data words depends on the data type. The default is to have hit data with “specials” appended:

```
CST Hit Word

        ssssssss'sssDDDDD'DDDDDppp'pppppppp

s:      11-bit scaled variance, scaled by 1/4
D:      10-bit pulse height ( RAW - PED - CM)
p:      11-bit strip number
----------------------------------------
CST Special Word

        10000fff'DDDDDDDD'DDDDDppp'pppppppp

f:      3-bit FADC number
D:      13-bit RAW data
p:      11-bit "strip"-number (1280-1287)
----------------------------------------
```

The Special words are present only every other event. This is indicated by bit 26 of the CST Data Header Word. If the block contains raw data, the data word is

```
CST Raw Word

        000eeeee'eeeeeeee'000ooooo'oooooooo

e:      13-bit raw FADC data from even strip numbers
o:      13-bit raw FADC data from odd strip numbers
----------------------------------------
```

For pedestal, sigma, or common mode data blocks, each data word contains the value for one channel.

Storage format of CST pedestals & sigmas Pedestals are kept at memory address `$0040'0000`. 32-bit words are being used, and blocks of (1280 strips × 8 FADCs) words are stored for 32 pipeline buffers consecutively:

$$\begin{array}{rl}
\texttt{\$0040'0000}: & \text{PIC 0, FADC 0} \\
\vdots & \qquad\vdots \\
\texttt{\$0040'1400}: & \text{PIC 0, FADC 1} \\
\vdots & \qquad\vdots \\
\vdots & \qquad\vdots \\
\texttt{\$0040'A000}: & \text{PIC 1, FADC 0} \\
\vdots & \qquad\vdots
\end{array}$$

In contrast to the raw data order (cf. Chap. 3.1.4), the pedestal words within a pipeline buffer block are stored sequentially for every FADC , i.e. each FADC has its own coherent memory block. The total size of the pedestal block is 4 bytes × 10240 strips × 32 Pipeline Buffers = 1280 kBytes.

Sigmas are kept at memory address `$0020'0000`. Rather than keeping just the rms noise sigma, a quadruple is stored for each strip:

(Variance, Pulse Height Sum, Pulse Height Sum Squared, Counts).

Each of the words is 32-bit, so that the total size of the “sigma block” is 4 bytes × 4 words × 10240 strips $=$ 160 kBytes.

List of Figures

List of Tables

Bibliography

[1] J.D. Bjorken. *Phys. Rev.*, 179:1547, 1969.

[2] C.G. Callan and D.J. Gross. High-energy electroproduction and the constitution of the electric current. *Phys. Rev. Lett.*, 22:23, 1969.

[3] C.F. Weizsäcker. Ausstrahlung bei Stößen sehr schneller Elektronen. *Z. Phys.*, 88:612, 1934. E.J. Williams. Nature of the high energy particles of penetrating radiation and status of ionization and radiation formulae. *Phys. Rev.*, 45:729,1934.

[4] G.A. Schuler, T. Sjöstrand. Towards a complete description of high-energy photoproduction. *Nucl.Phys.*, B407:539–605, 1993.

[5] H. Fritzsch, K.H. Streng. Photoproduction of heavy quark flavors. *Phys.Lett.*, B72:385, 1978.

[6] R.K. Ellis, P. Nason. QCD radiative corrections to the photoproduction of heavy quarks. *Nucl.Phys.*, B312:551, 1989.

[7] S. Frixione, M.L. Mangano, P. Nason, G. Ridolfi. Total cross sections for heavy flavour production at HERA. *Phys. Lett.*, B348:633–645, 1995.

[8] M. Kander. Bestimmung des ep-Wirkungsquerschnittes von Beauty-Quarks durch ihren semileptonischen Zerfall in Myonen mit dem H1-Detektor bei HERA. Ph.D. thesis, Fachbereich Physik, Universität Hamburg, 1998.

[9] S. Frixione, M.L. Mangano, P. Nason, G. Ridolfi. Heavy quark production. Preprint CERN-TH/97-16, 1997.

[10] Particle Data Group (R.M. Barnett et al.). Review of particle physics. *Phys. Rev.* D, 54:1–720, 1996.

[11] J. Antos et al. The SVX-II silicon vertex detector upgrade at CDF. *Nucl. Instr. and Meth.*, A360:118–124, 1995.

[12] W.E. Cooper. The D0 silicon tracker. *Nucl. Instr. and Meth.*, A368:205–210, 1995.

[13] K. Abe et al. Design and performance of the SLD vertex detector, a 307 Mpixel tracking system. *Nucl. Instr. and Meth.*, A400:287–343, 1997.

[14] B. Mours et al. The design, construction and performance of the ALEPH silicon vertex detector. *Nucl. Instr. and Meth.*, A379:101–115, 1996.

[15] V. Chabaud et al. The DELPHI silicon strip microvertex detector with double sided readout. *Nucl. Instr. and Meth.*, A368:314–332, 1996.

[16] L3 SMD collaboration (M. Acciarri et al.). The L3 silicon microvertex detector. *Nucl. Instr. and Meth.*, A360:103–109, 1995.

[17] S. Anderson et al. The extended OPAL silicon strip microvertex detector. *Nucl. Instr. and Meth.*, A403:326–350, 1998.

[18] N. Cabibbo. Unitary symmetry and leptonic decays. *Phys. Rev. Lett.*, 10:531, 1963.
M. Kobayashi and T. Maskawa. *CP* violation in the renormalizable theory of weak interaction. *Prog. Theo. Phys.* 49:652,1973.

[19] ARGUS collaboration (H. Albrecht et al.). A measurement of the inclusive semileptonic decay fraction of charmed hadrons. *Phys. Lett.*, B278:202, 1992.

[20] OPAL collaboration (P.D. Acton et al.). Measurement of $\Gamma(\mathrm{Z}^0 \to b\bar{b})/\Gamma(\mathrm{Z}^0 \to \text{hadrons})$ using leptons. *Z. Phys.*, C58:523, 1993.

[21] ARGUS collaboration (H. Albrecht et al.). A model independent determination of the inclusive semileptonic decay fraction of *B* mesons. *Phys. Lett.*, B318:397, 1993.

[22] H. Niggli. Direct gluon density determination in tagged charm-photoproduction at HERA. Ph.D. thesis, Swiss Federal Inst. of Technology Zürich, Mar. 1998.

[23] U. Langenegger. A measurement of the beauty and charm production cross sections at the *ep* collider HERA. Ph.D. thesis, Swiss Federal Inst. of Technology Zürich, Apr 1998.

[24] HERMES collaboration (K. Ackerstaff et al.). First results from the HERMES experiment. *Phys.Lett.*, B404:383–389, 1997.

[25] HERA-*B* collaboration (H. Albrecht et al.). HERA-*B*: An experiment to study *CP*-violations in the *B*-system using an internal target at the HERA proton ring. Technical proposal, *DESY-PRC* 94/02, 1994.

[26] H1 collaboration (I. Abt et al.). The H1-detector at HERA. *Nucl. Instr. and Meth.*, A386:310, 1997.

[27] H1 collaboration (I. Abt et al.). Technical proposal to upgrade the backward scattering region of the H1-detector. *DESY PRC* 93/02, 1993.

[28] B. Schwab. Das Rückwärtskammersystem des H1-Experiments. Ph.D. thesis, Universität Heidelberg, 1996.

[29] H1-SPACAL group (T. Nicholls et al.). Performance of an electromagnetic lead/scintillating-fibre calorimeter for the H1-detector. *Nucl. Instr. and Meth.*, A374:149, 1996.

[30] V. Karimäki. Fast code to fit circular arcs. Univ. of Helsinki Report HU-SEFT-1991-10, 1991.

[31] M.W. Schulz. Untersuchung von Methoden zur Kalibration der H1-Jetkammer. Ph.D. thesis, Fachbereich Physik, Univ. Hamburg, 1993.

[32] M. Wagener. Scale dependence of the charm production cross section and performance of the Central Silicon Tracker at the H1 experiment. Ph.D. thesis, Swiss Federal Inst. of Technology Zürich, July 1997.

[33] D. Pitzl et al. Evaluation of double-sided, AC-coupled, double metal silicon strip detectors for H1 at HERA. *Nucl. Instr. and Meth.*, A348:454–460, 1994.

[34] J. Gassner. Messung der Ortsauflösung des H1-Siliziumvertexdetektors. Diploma Thesis IPP ETH Zürich. ETHZ-IPP Internal Report 96-4, Dec. 1996.

[35] W.J. Haynes, P. Burch, R. Halsall, W. Melotti, G. Noyes, M. Kausch, P. Kostka, D. Pitzl. The H1 silicon tracker data acquisition system. *Nucl. Instr. and Meth.*, A403:313–325, 1998.

[36] E. Pietarinen. VMEbus cross interface processor module with high speed fibre optic links: VMExi. Univ. of Helsinki Report HU-SEFT-1991-14, Helsinki, June 1991.

[37] R. Horisberger and D. Pitzl. A novel readout chip for silicon strip detectors with analog pipeline and digitally controlled analog signal processing. *Nucl. Instr. and Meth.*, A326:92–99, 1993.

[38] J. Bürger et al. The readout system of the H1 silicon detectors. *Nucl. Instr. and Meth.*, A367:422–427, 1995.

[39] S.A. Prell. Entwicklung des Steuer- und Auslesemoduls für die Siliziumstreifendetektoren des H1-Detektors. PhD thesis, Univ. Hamburg, 1996.

[40] H1 collaboration. Technical proposal to build silicon tracking detectors for H1. *DESY PRC*, 92/01, July 1992.

[41] W. Erdmann, R. Eichler, H. Niggli, D. Pitzl (Zürich, ETH), M. Wagener, K. Gabathuler, R. Horisberger (PSI, Villigen). Optical analog readout and control of the central silicon vertex detector of H1 at HERA. *Nucl. Instr. and Meth.*, A372:188–194, 1996.

[42] S. Prell. OSCA - OnSiRoC Sequencer Compiler Application, 1995. H1 internal note.

[43] Creative Electronics Systems SA, Geneva, CH. RIO2 8060 PowerPC based RISC I/O VMEbus board, 1996.

[44] G. Noyes, P. Burch. RAL-PC3050 RIO2 FADC PMC. RAL Technology, Jan. 1997.

[45] W.J. Haynes. SiPPCvmexi_SSP - H1 Silicon Tracker PowerPC Readout - VMEtaxi Mark-2 System Software Package. RAL, Jan 1997. Version 2.0.

[46] Motorola Inc. Motorola C/C++ SDK PowerPC Edition for MacOS DR 2.0/MPW - User's Guide, December 1996.

[47] Motorola Inc. PowerPC 604 RISC microprocessor user's manual.

[48] M. Zimmer. Graphics-oriented operator interfaces at H1. In *Proc. Int. Conf. Computing in High Energy Physics '91*, Tsukuba, Japan, March 1991.

[49] J. Coughlan, D. Düllmann, M. Savitski, M. Zimmer. Object oriented programming for online systems at H1. In *Proc. Int. Conf. Computing in High Energy Physics '92*, pages 519–522, 1992.

[50] T. Shanley. PowerPC System Architecture. Addison-Wesley, Reading, Mass., Feb. 1995.

[51] Motorola Inc. PowerPC microprocessor family: the programming environments, May 1996. Rev 0.1.

[52] M. Kausch. SiPPCUser - H1 Silicon Tracker Hit Finding Routines. H1 internal note, Jan 1997. Version 2.0.

[53] B.G. Taylor. The MacVEE User Manual. CERN, Geneva, 1989.

[54] Creative Electronics Systems SA, Geneva, CH. MAC 7212, Mac II NuBus to VMV/VME Interface, 1990.

[55] Creative Electronics Systems SA, Geneva, CH. FIC8230, 1989.

[56] Creative Electronics Systems SA, Geneva, CH. RAID 8239, R3000 VMEbus controller, 1990.

[57] Creative Electronics Systems SA, Geneva, CH. VME/VSB Dual Ported Memory DPM 8242, 1989.

[58] A.B. Fahr. KOOL WWW manual, 1997.

[59] LHIS. A fast histogram booking, filling and manipulation package based on LOOK.

[60] M. Kausch. How to use the Silicon Farm - H1 Silicon Tracker Data Monitoring. H1 internal note, Jan 1997. Version 1.0.

[61] V. Blobel. The BOS system. Dynamic memory management, Dec. 1987. Internal note. Second updated printing.

[62] V. Blobel. Methoden der Datenanalyse in der Hochenergiephysik. Internal Note DESY F14-81/01, July 1981.

[63] V. Blobel. Constrained least squares and error propagation. Internal note. Hamburg, July 1997.

[64] V. Blobel. Online monitoring and determination of run-dependent calibration constants within reconstruction modules. *H1 software note* No. 41, Aug. 1993. updated Jan. 1996.

[65] G. Ingelman, J. Rathsman, G.A. Schuler. AROMA 2.1 — A Monte Carlo Generator for Heavy Flavour Events in *ep* Collisions. DESY internal note. Draft, unpublished, June 1995.

[66] T. Sjöstrand. PYTHIA 5.7 and JETSET 7.4: Physics and manual. CERN-TH-7112-93, 1994.

[67] R. Brun et al. GEANT3. CERN-DD/EE/84-1, 1987.

[68] OPAL collaboration (G. Alexander et al.). A study of charm hadron production in $Z^0 \to c\bar{c}$ and $Z^0 \to b\bar{b}$ decays at LEP. *Z. Phys.*, C72:1–16, 1996.

[69] ALEPH, DELPHI, L3, and OPAL collaborations. Combining heavy flavor electroweak measurements at LEP. *Nucl. Instr. and Meth.*, A378:101–115, 1996.

[70] ALEPH collaboration (D. Decamp et al.). Measurement of the B hadron lifetime. *Phys. Lett.*, B257:492–504, 1991.

[71] DELPHI collaboration (P. Abreu et al.). Measurement of the average lifetime of B hadrons. *Z.Phys.*, C53:567–580, 1992.

[72] J. Hagemann. Bestimmung der mittleren Lebensdauer von *B*-Hadronen mit der Impaktparameter-Methode am Experiment JADE. Ph.D. thesis, Fachbereich Physik, Universität Hamburg, 1989.

[73] L. West. How to use the Heavy Flavour Working Group Track, Muon and Electron Selection Code. H1 internal note, July 1996.

[74] W.J. Haynes. VMExi2_SSP - VMEtaxi Mark-2 System Software Package, July 1993. Version 4.2.

[75] W.J. Haynes. SiVMEXI - H1 Silicon Trackers: VMEtaxi Data Acquisition. RAL, 1996. Version 1.1.

Danksagung

Ich danke Frau Prof. Naroska für ihr Interesse und ihre konstruktive Kritik an dieser Arbeit, die mich insbesondere in den letzten Wochen entscheidend vorangebracht hat. Herrn Prof. Klanner danke ich für die Erstellung des zweiten Gutachtens.

Ein besonderer Dank geht an Jochen Bürger für die Anbahnung dieser Arbeit, für Rat und Tat während mehr als drei Jahren und für wichtige Kritik zum dritten Kapitel.

Herrn Prof. Blobel danke ich für unzählige Ratschläge und viele gute Ideen, für hochwertige Software sowie für die wertvollen Kommentare zum vierten Kapitel.

Einen herzlichen Dank an Daniel Pitzl für nie versiegenden Optimismus auch in aussichtslosen Lagen, für die vielen Dinge, die ich von ihm über Siliziumdetektoren gelernt habe, und für viele Einfälle und Verbesserungsvorschläge für die Online-Software.

Gareth Noyes gebührt ein besonderer Dank für seine geduldigen Erklärungen, ohne die ich das Datenaufnahmesystem bis heute nicht verstanden hätte. Bill Haynes danke ich für das Vertrauen in einen Doktoranden, der im Programmieren von Online-Software dilettiert und für die prompten Antworten auch auf die dümmeren Fragen.

Ich danke Martin Kander für die Weitergabe von wertvollen Erfahrungen bei der Myonenanalyse.

Einen Dank an alle, die über die Jahre zum Gelingen des Projekts und somit dieser Arbeit beigetragen haben, besonders an Olaf Behnke, Monika Biddulph, Alan Campbell, Prof. Ralph Eichler, Peter Kostka, Hubert Niggli und Yorgos Tsipolitis.

Für das Lesen und Kommentieren von Teilen bzw. der ganzen Arbeit danke ich Eckhard Elsen, Jörg Gayler und Frank Lehner. Und schließlich ein Dankeschön an meine Zimmergenossen Jörn Steinhart und Stephan Hurling für stete Anteilnahme und für ein angenehmes Arbeitsklima.